Non-degenerate two-photon absorption in bulk ZnSe, GaAs and Si

Dissertation

submitted in partial fulfillment
of the requirements for the degree of
Dr. rer. nat.
to the Faculty of Physics
TU Dortmund University, Germany

by

Laura Krauß-Kodytek

Dortmund, April 2022

technische universität
dortmund

1st Reviewer: Prof. Dr. Markus Betz (TU Dortmund University)
2nd Reviewer: Prof. Dr. Carsten Westphal (TU Dortmund University)

Abstract

The two-photon absorption is a nonlinear optical process with various properties which makes it an excellent basis for a wide range of different applications. In this thesis the non-degenerate two-photon absorption coefficient $\beta(\omega_1, \omega_2)$ as a function of the frequency ratio ω_1/ω_2 of the two driving fields is experimentally investigated whereby the sum energy $\hbar\omega_1 + \hbar\omega_2$ is kept constant. The studied materials are the prototypical semiconductors ZnSe, GaAs and Si. Regardless of the direct or indirect character of the bandgap, the two-photon absorption strength increases with increasing ratio $\omega_1/\omega_2 \geq 1$. The experimental data of ZnSe and GaAs agrees well with corresponding theoretical predictions for direct semiconductors. Si shows overall smaller absorption strengths. These results also agree with theoretical predictions for indirect semiconductors. In addition, different crystallographic orientations of the samples and polarization configurations of the two driving fields are analyzed. These results make an important contribution to the so far rarely investigated orientation and polarization anisotropy of the non-degenerate two-photon absorption.

Kurzfassung

Die Zwei-Photonen-Absorption ist ein nichtlinearer optischer Prozess mit diversen Eigenschaften, welche sie zu einer ausgezeichneten Grundlage für ein breites Spektrum verschiedener Anwendungen macht. In dieser Arbeit wird der nicht-entartete Zwei-Photonen-Absorptionskoeffizient $\beta(\omega_1, \omega_2)$ als Funktion des Frequenzverhältnisses ω_1/ω_2 bei einer konstanten Übergangsenergie $\hbar\omega_1 + \hbar\omega_2$ experimentell untersucht. Die verwendeten Materialien sind die Halbleiter ZnSe, GaAs und Si. Unabhängig von dem direkten oder indirekten Charakter der Bandlücke steigt die Zwei-Photonen-Absorptionsstärke mit zunehmendem Verhältnis $\omega_1/\omega_2 \geq 1$. Die experimentellen Daten von ZnSe und GaAs stimmen sehr gut mit den entsprechenden theoretischen Vorhersagen für direkte Halbleiter überein. Bei Si zeigen sich im Vergleich insgesamt geringere Absorptionsstärken. Auch hier stimmen die Ergebnisse mit den theoretischen Vorhersagen für indirekte Halbleiter überein. Darüber hinaus werden verschiedene kristallographische Orientierungen der Proben und unterschiedliche Polarisationseinstellungen der beiden anregenden optischen Felder analysiert. Diese Ergebnisse leisten einen wichtigen Beitrag zu der bisher wenig untersuchten Orientierungs- und Polarisationsanisotropie der nicht-entarteten Zwei-Photonen-Absorption.

to Leonard

Contents

Introduction

Physics would be dull and life most unfulfilling if all physical phenomena around us were linear. Fortunately, we are living in a nonlinear world. While linearization beautifies physics, nonlinearity provides excitement in physics.

Y. R. Shen - The Principles of Nonlinear Optics [1]

These exciting nonlinear phenomena, which Y. R. Shen describes so vividly, occur in a variety of effects when high intensity laser light interacts with matter. One of those effects is the two-photon absorption. In contrast to the linear one-photon absorption, here two photons simultaneously trigger an optical transition from the ground to an excited state whereby the energy of each photon alone is not sufficient to compensate for the energy difference in between those states. These two photons can either have the same or different frequencies, which then will be referred to as degenerate or non-degenerate two-photon absorption (see Figure 1). Considering a semiconductor this could be a transition from the valence band to the conduction band, although the energy of each involved photon is smaller than the bandgap energy and only their sum energy exceeds the bandgap energy.

The first theoretical description of the two-photon absorption was already proposed in 1931 by Maria Göppert-Mayer using second-order perturbation theory [2]. However, since the probability for a two-photon absorption is too small to be triggered with any conventional light source, the first experimental observation lasted until the demonstration of the first running laser device by T. H. Maiman in 1960 – a 694.3 nm pulsed ruby-crystal laser [3, 4]. Shortly after, in the early 1960s, W. Kaiser and C. G. B. Garrett [5] reported a two-photon induced frequency upconversion fluorescence in a CaF_2:Eu^{2+} crystal excited by the intense radiation from the recently developed ruby-crystal laser. In fact, the population of the energy levels of the Eu^{2+} impurities and the ensuing blue fluorescence could only be induced by two red ruby-crystal laser photons. In 1964 R. Braunstein and N. Ockman were the first ones observing two-photon absorption in a semiconductor [6]. They triggered a two-photon excitation of an electron from the valence to the conduction band in a CdS crystal also

using a ruby-crystal laser and investigated different aspects of the radiative recombination emission. Until the 1980s the two-photon absorption was mainly used as a spectroscopic tool as it enabled the access to eigenstates of matter that were not accessible with linear, one-photon optical spectroscopy. But later on, various applications quickly developed that took advantage of the benefits of the two-photon absorption. Today, there is a wide variety of applications.

A well established example are two-photon absorption based autocorrelators for the temporal characterization of ultra-short laser pulses [7]. They exhibit many advantages in contrast to the standard autocorrelation technique using a nonlinear crystal. A two-photon absorption autocorrelator unites the autocorrelation signal generation and detection in a single semiconductor device, since the optically correlated signal is directly transformed into an electrical signal via the two-photon absorption. Expensive nonlinear crystals can therefore be replaced by commercially available and robust photodiodes for the analysis of pulses with wavelengths continuously ranging from the ultraviolet to the infrared region [8]. Since a two-photon absorption ends in a transition of a charge carrier at an excited state, no photon momentum needs to be conserved, which further makes the autocorrelator easier to use, more sensitive and allows the characterization of extremely short pulses down to a few femtoseconds. [9]
Further two-photon absorption applications from the field of photonics are, for example, infrared detection [10], optical switching [11] and coherent control of photocurrents [12, 13], which all benefit from the various advantages of the two-photon absorption.

The development of new technologies is based on extensive theoretical and experimental fundamental research. Therefore, various aspects of the two-photon absorption have been intensively studied and have drawn a comprehensive picture of its properties and characteristics. Even so, there are many unanswered questions which still makes the two-photon absorption a desirable topic for today's scientists.

This thesis contributes to the fundamental understanding of the two-photon absorption and experimentally investigates the non-degenerate two-photon absorption coefficient $\beta(\omega_1, \omega_2)$ as a function of the frequency ratio ω_1/ω_2 of the two driving fields. The investigated materials are the prototypical bulk semiconductors ZnSe, GaAs and Si, which are well characterized and irreplaceable in up-to-date technologies. The therefore used experimental setup is designed in a pump-probe scheme. In combination with a tunable laser source, it is possible to systematically acquire the two-photon absorption strength from degener-

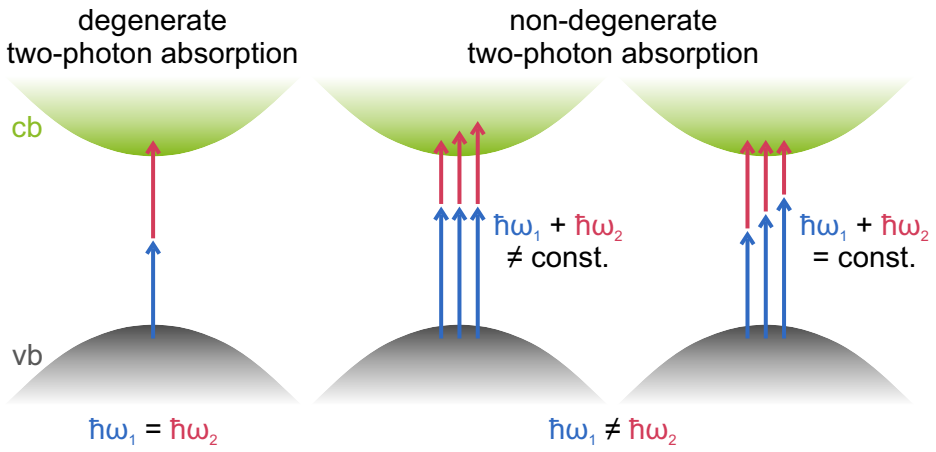

Figure 1: Schematic representation of a two-photon transition in a direct semiconductor from the valence band (vb) to the conduction band (cb). The transition can be triggered by a degenerate photon pair with the same frequencies or a non-degenerate photon pair with different frequencies. Comparing different non-degenerate two-photon absorption configurations, either one photon frequency can be kept constant and the other photon frequency is varied or the sum frequency is kept constant and both frequencies are varied.

ate configurations with $\omega_1/\omega_2 = 1$ up to non-degenerate configurations with $\omega_1/\omega_2 > 1$ while keeping the sum energy $\hbar\omega_1 + \hbar\omega_2$ of the two photons constant. The experimentally measured scaling behaviour $\beta(\omega_1/\omega_2)$ is analyzed and compared among the three samples to stress the differences for direct and indirect bandgap semiconductors. The accordance with corresponding theoretical predictions is evaluated.

Previous experimental studies were mainly related to degenerate configurations where the two-photon absorption strength is often studied in a z-scan experiment [14] with only one driving laser field. Less experimental studies focused on non-degenerate configurations. For direct gap semiconductors various experiments employed driving fields close to degeneracy [15], others configurations with frequency ratios $\omega/2\omega$ [16]. Also widely non-degenerate configurations were investigated, in which one driving field has a fixed and the other one a variable frequency [17, 18, 19]. All these studies showed an increasing two-photon absorption strength for non-degenerate in contrast to degenerate configurations. Nevertheless, a study measuring the two-photon absorption strength for increasing frequency ratios at a constant sum energy of the two photons is lacking so far. Non-degenerate studies for indirect semiconductors are even less performed. The few available studies mainly concentrate on non-degenerate 2PA at discrete wavelength configurations, especially in Si waveguides at the telecommunication wavelengths [20, 21, 22]. Only the joint study of Sanaz Faryadras and Cox et al. [23, 24] investigated the non-degenerate 2PA in bulk Si for different fre-

quency ratios but with varying sum energy. The studies for indirect semiconductors also show an enhancement of the 2PA strength with increasing difference in between the photon frequencies but with overall smaller absorption strengths.
Another focus of this thesis is the orientation and polarization anisotropy of the two-photon absorption coefficient $\beta(\omega_1, \omega_2)$. For the investigation of the orientation anisotropy each sample is measured in (100) and (110) crystallographic orientation and the results are compared. For the polarization anisotropy, measurement configurations are used where the two, both linearly polarized, driving fields are either parallel or perpendicular aligned to each other. The results of the orientation and polarization anisotropy measurements are further analyzed dependent on the frequency ratio ω_1/ω_2.
Only very few experimental studies have investigated the anisotropy of the two-photon absorption. Especially, studies for non-degenerate configurations at different frequency ratios are missing so far, although degenerate studies for direct gap semiconductors yield high anisotropy effects [25, 26, 27, 28, 29]. Research on indirect semiconductors is even scarcer. The few experimental results for Si partially give rise to similar characteristics of the degenerate two-photon absorption anisotropy [30, 31, 32, 33], but need to be continued for conclusive results. Experimental data for non-degenerate configurations is missing entirely.

In a nutshell, the two-photon absorption shows a variety of interesting characteristics, leading to diverse applications in fundamental scientific research but also industrial areas as for example medicine and engineering. This wide-ranging interest is a great opportunity for jointly developed new insights and holds a lot of promise for future research on two-photon absorption.

The references in this thesis do not claim to be complete. Often, only a selection of the most recent publications or a selection of publications, in which a technology, a theoretical approach or a specific experiment is mentioned first, is given. If the name of an author is given in the continuous text and the (lead) author is a woman, also the surname is added to enhance the visibility of women in science.

Chapter 1

Theoretical Background

This chapter introduces the theoretical concepts of nonlinear optical phenomena in general and describes the process of nonlinear two-photon absorption more precisely. In particular the two-photon absorption coefficient, describing the strength of a two-photon absorption, is introduced and its scaling behavior in semiconductors under the influence of certain parameters is further analyzed. Differences for direct and indirect semiconductors are outlined. In addition, the anisotropy of the two-photon absorption coefficient is examined.

1.1 Nonlinear optics

The field of nonlinear optics comprises a variety of phenomena which occur when high intensity laser light interacts with matter. Already a few decades after the advent of the laser, much more nonlinear effects have been experimentally investigated as conventional linear effects were explored in the past. The reason for the rapid growth of this new branch stemmed from the unique characteristics of the laser. In comparison to conventional light sources, laser light is monochromatic, directional and coherent and can reach high intensities. These properties form the basis for the observation of nonlinear optical phenomena whose potential is still not exhausted to date, giving rise to undiscovered effects and their applications. [34]

1.1.1 The electric nonlinear polarization

The Maxwell's equations build the theoretical foundation for describing phenomena in classical electrodynamics. The interaction of an electromagnetic light field $\mathbf{E}$[1] with a

[1] Letters printed in bold will subsequently denote vectorial quantities.

dielectric material is comprised in these equations by the electric displacement field

$$\mathbf{D} = \epsilon_0 \mathbf{E} + \mathbf{P}(\mathbf{E}) \tag{1.1}$$

with the vacuum permittivity ϵ_0. The electric polarization $\mathbf{P}$ is defined as the dipole moment per unit volume induced by the spatial displacement of the bound charges in the solid structure due to the incident electric field. If the amplitude of the electric field is small, the electric polarization will be linearly dependent on the electric field

$$\mathbf{P}_\mathrm{L} = \epsilon_0 \chi^{(1)} \mathbf{E} \tag{1.2}$$

with $\chi^{(1)}$ being the linear susceptibility. For small optical field strengths this linear approximation is valid since the electrons can be assumed to be bound in a parabolic potential. However, for high optical field strengths the anharmonic part of the potential must also be considered as the spatial displacement between the atomic nuclei and their electrons increases. Therefore, the definition of the electric polarization has to be generalized by expressing it as a power series in the driving electrical field

$$\begin{aligned} \mathbf{P} &= \mathbf{P}_\mathrm{L} + \mathbf{P}_\mathrm{NL} \\ &= \epsilon_0 \chi^{(1)} \mathbf{E} + \epsilon_0 \chi^{(2)} \mathbf{E}^2 + \epsilon_0 \chi^{(3)} \mathbf{E}^3 + \dots \\ &= \epsilon_0 \sum_{n=1}^{\infty} \chi^{(n)} \mathbf{E}^n \end{aligned} \tag{1.3}$$

where $\chi^{(n)}$ denotes the nth-order susceptibility. In order to obtain a sufficiently strong displacement of the bound charges and thus to access the higher-order terms of the electric polarization, high optical field amplitudes are required. An optical field with an intensity comparable to a conventional light source would have an electric field amplitude too small in comparison to the characteristic atomic Coulomb field to enable the access to the nonlinear regime. The intensity of the sun, for example, would result in a field amplitude[2] of $E_\mathrm{solar} \approx 1013\,\mathrm{V/m}$ whereas the atomic field amplitudes[3] are in the order of $10^{11}\,\mathrm{V/m}$ considering a hydrogen atom. Therefore, intense laser sources with amplitudes of about $10^7\,\mathrm{V/m}$ are needed to introduce nonlinearities.

[2] The laser intensity I in terms of the peak field strength E_0 is given by $I = \frac{1}{2}\epsilon_0 c E_0^2$ with c the speed of light in vacuum. Followingly, the total solar intensity, given by the solar constant of $1361\,\mathrm{W/m^2}$ [35], would lead to a maximum field strength $E_\mathrm{solar} \approx 1013\,\mathrm{V/m}$. The solar constant is obtained for a surface perpendicular to the sun rays in roughly the distance from sun to earth without atmospheric influence.

[3] The atomic field amplitude of the hydrogen atom can be calculated by $E_\mathrm{atomic} = \varepsilon_\mathrm{Ryd}/a_0 e$ whereby ε_Ryd is the Rydberg energy, a_0 the Bohr radius and e the elementary charge.

If the nonlinear electric polarization is included in the electric displacement field, the wave equation in nonlinear optical media, with consideration of the Maxwell's equations, can be obtained as

$$\nabla^2\mathbf{E} - \frac{n^2}{c^2}\frac{\partial^2}{\partial t^2}\mathbf{E} = \frac{1}{\epsilon_0 c^2}\frac{\partial^2}{\partial t^2}\mathbf{P}_{\mathrm{NL}} \tag{1.4}$$

whereby c is the speed of light in vacuum. The linear part of the polarization is included by the quadratic refractive index $n^2 = 1 + \chi^{(1)}$. The wave equation illustrates that in nonlinear optics the time-varying nonlinear polarization acts as a driving force for new components of the electromagnetic field, leading to a variety of nonlinear optical phenomena.

These nonlinear optical phenomena can have the most different forms. In the regime of the second-order polarization, effects such as second-harmonic generation, sum- and difference-frequency generation occur. They, for example, exhibit new frequencies next to the driving field frequency after the interaction of the nonlinear medium with the optical light source. The third-order polarization leads to two-photon absorption which will be described in detail in Chapter 1.2. Another third-order effect among others is self-focusing where the nonlinear material itself acts as a converging lens due to an optically induced change in the refractive index. Also higher-order polarizations enable a variety of effects, but the accessibility decreases as the required illumination strengths increase. [36, 37]

1.1.2 The nonlinear susceptibility tensor

In general, the material dependent nth-order susceptibility $\chi^{(n)}$ is a tensor of $(n+1)$th-rank with 3^{n+1} elements, describing the proportionality of the electric polarization and the applied electric field as introduced in Equation (1.3).
In case of a linear light-matter interaction, one optical field with frequency ω introduces an electric polarization which can only induce a secondary optical field of the initial frequency ω. The spatial components of that polarization can generally be described by

$$P_{\mathrm{i}}^{(1)}(\omega) = \epsilon_0 \sum_{\mathrm{j}} \chi_{\mathrm{ij}}^{(1)}(\omega;\,\omega) E_{\mathrm{j}}(\omega) \tag{1.5}$$

with i and j denoting the spatial coordinates x, y and z. The linear susceptibility tensor $\chi^{(1)}$ is a 3×3-matrix and comprises nine elements. In the matrix formalism the linear electric polarization can be expressed as

$$\begin{pmatrix} P_x^{(1)} \\ P_y^{(1)} \\ P_z^{(1)} \end{pmatrix} = \epsilon_0 \begin{pmatrix} \chi_{xx}^{(1)} & \chi_{xy}^{(1)} & \chi_{xz}^{(1)} \\ \chi_{yx}^{(1)} & \chi_{yy}^{(1)} & \chi_{yz}^{(1)} \\ \chi_{zx}^{(1)} & \chi_{zy}^{(1)} & \chi_{zz}^{(1)} \end{pmatrix} \cdot \begin{pmatrix} E_x \\ E_y \\ E_z \end{pmatrix} . \tag{1.6}$$

Going to nonlinear light-matter interactions, the number of susceptibility tensor elements rapidly increases since more optical fields can interact. In case of a second-order nonlinear process the applied optical field can comprise up to two frequency components ω_m and ω_n so that the ith component of the electric polarization can in general be written as

$$P_\mathrm{i}^{(2)}(\omega_\mathrm{m}+\omega_\mathrm{n}) = \epsilon_0 \sum_{\mathrm{jk}} \sum_{(\mathrm{mn})} \chi_{\mathrm{ijk}}^{(2)}(\omega_\mathrm{m}+\omega_\mathrm{n};\, \omega_\mathrm{m}, \omega_\mathrm{n}) E_\mathrm{j}(\omega_\mathrm{m}) E_\mathrm{k}(\omega_\mathrm{n}) \tag{1.7}$$

with the indices $\mathrm{i,j,k} \in \{x, y, z\}$ denoting the spatial coordinates. The summation over (mn) takes account of all possible permutations of the frequencies ω_m and ω_n. Since the field amplitudes $E_\mathrm{j}(\omega_\mathrm{m})$ and $E_\mathrm{k}(\omega_\mathrm{n})$ are associated with the time dependencies $\exp(-i\omega_\mathrm{m}t)$ and $\exp(-i\omega_\mathrm{n}t)$, respectively, their product yields $\exp(-i(\omega_\mathrm{m}+\omega_\mathrm{n})t)$ so that the nonlinear polarization oscillates at a frequency $\omega_\mathrm{m}+\omega_\mathrm{n}$ as denoted in the notation of Equation (1.7). The second-order susceptibility tensor $\chi^{(2)}$ comprises 27 elements and is given in matrix notation by

$$\begin{pmatrix} P_x^{(2)} \\ P_y^{(2)} \\ P_z^{(2)} \end{pmatrix} = \epsilon_0 \begin{pmatrix} \chi_{xxx}^{(2)} & \chi_{xxy}^{(2)} & \chi_{xxz}^{(2)} & \cdots & \chi_{xzz}^{(2)} \\ \chi_{yxx}^{(2)} & \chi_{yxy}^{(2)} & \chi_{yxz}^{(2)} & \cdots & \chi_{yzz}^{(2)} \\ \chi_{zxx}^{(2)} & \chi_{zxy}^{(2)} & \chi_{zxz}^{(2)} & \cdots & \chi_{zzz}^{(2)} \end{pmatrix} \cdot \begin{pmatrix} E_x \cdot E_x \\ E_x \cdot E_y \\ E_x \cdot E_z \\ \vdots \\ E_z \cdot E_z \end{pmatrix} . \tag{1.8}$$

The tensor element $\chi_{zxy}^{(2)}$, for example, gives the introduced electric polarization in z-direction if the driving optical fields are polarized in x- and y-direction. In a third-order nonlinear process the applied optical field can comprise up to three frequencies ω_m, ω_n and ω_o. The ith component of the third-order polarization can therefore be described by

$$P_\mathrm{i}^{(3)}(\omega_\mathrm{m}+\omega_\mathrm{n}+\omega_\mathrm{o}) = \epsilon_0 \sum_{\mathrm{jkl}} \sum_{(\mathrm{mno})} \chi_{\mathrm{ijkl}}^{(3)}(\omega_\mathrm{m}+\omega_\mathrm{n}+\omega_\mathrm{o};\, \omega_\mathrm{m}, \omega_\mathrm{n}, \omega_\mathrm{o}) E_\mathrm{j}(\omega_\mathrm{m}) E_\mathrm{k}(\omega_\mathrm{n}) E_\mathrm{l}(\omega_\mathrm{o}) \tag{1.9}$$

with the indices $\mathrm{i,j,k,l} \in \{x, y, z\}$ and the summation over (mno) again representing all possible frequency permutations. The third-order susceptibility tensor $\chi^{(3)}$ increases to 81 elements and is given in matrix notation by

$$\begin{pmatrix} P_x^{(3)} \\ P_y^{(3)} \\ P_z^{(3)} \end{pmatrix} = \epsilon_0 \begin{pmatrix} \chi_{xxxx}^{(3)} & \chi_{xxxy}^{(3)} & \chi_{xxxz}^{(3)} & \cdots & \chi_{xzzz}^{(3)} \\ \chi_{yxxx}^{(3)} & \chi_{yxxy}^{(3)} & \chi_{yxxz}^{(3)} & \cdots & \chi_{yzzz}^{(3)} \\ \chi_{zxxx}^{(3)} & \chi_{zxxy}^{(3)} & \chi_{zxxz}^{(3)} & \cdots & \chi_{zzzz}^{(3)} \end{pmatrix} \cdot \begin{pmatrix} E_x \cdot E_x \cdot E_x \\ E_x \cdot E_x \cdot E_y \\ E_x \cdot E_x \cdot E_z \\ \vdots \\ E_z \cdot E_z \cdot E_z \end{pmatrix} . \tag{1.10}$$

For higher-order processes the mathematical description is equally applicable but much more extensive because of the rising number of tensor elements and interacting fields as

already described here for only the first three polarization orders.

Fortunately, by taking into account various symmetry considerations, the number of tensor elements can be strongly reduced. One example is the intrinsic permutation symmetry, which states that the order of the fields $E_{\mathrm{j}}(\omega_{\mathrm{m}})E_{\mathrm{k}}(\omega_{\mathrm{n}})$ in Equation (1.7) is physically irrelevant and thus the according tensor elements

$$\chi^{(2)}_{\mathrm{ijk}}(\omega_{\mathrm{m}}+\omega_{\mathrm{n}};\,\omega_{\mathrm{m}},\omega_{\mathrm{n}}) = \chi^{(2)}_{\mathrm{ijk}}(\omega_{\mathrm{m}}+\omega_{\mathrm{n}};\,\omega_{\mathrm{n}},\omega_{\mathrm{m}}) \tag{1.11}$$

are equal. This consideration is similarly applicable for every nth-order susceptibility tensor and reduces the number of independent elements. Another example is the spatial symmetry of the nonlinear material which also has a strong influence on the number of tensor elements. In particular, for materials with high crystal symmetries many tensor elements are zero or have the same value. In media showing inversion symmetry all odd-rank susceptibilities $\chi^{(n)}$ (n: even) vanish (as all tensor elements $\chi^{(2)}_{\mathrm{ijk}}$ are zero) and the third-order susceptibility, as first nonzero term, dominates the nonlinear response. Further specific reductions can be made with regard to the seven different crystal systems[4]. The cubic system is one of them to which many semiconductors belong. Due to the symmetry properties of cubic materials the linear susceptibility tensor $\chi^{(1)}$ only exhibits diagonal elements of which all are equal. The tensor elements of higher-order susceptibilities of cubic crystals are also reduced. Considering a third-order nonlinear interaction, its susceptibility tensor $\chi^{(3)}$ is reduced from 81 to 21 nonzero elements. The cubic system can further be subdivided into five point groups. For the point groups 432, $\bar{4}$3m and m$\bar{3}$m only four of the 21 tensor tensor elements are independent and for the point groups 23 and m$\bar{3}$ only seven elements are independent. The corresponding spatial coordinates of the independent third-order susceptibility tensor elements are

$$\left.\begin{aligned} xxxx &= yyyy = zzzz \\ yyzz &= zzyy = zzxx = xxzz = xxyy = yyxx \\ yzyz &= zyzy = zxzx = xzxz = xyxy = yxyx \\ yzzy &= zyyz = zxxz = xzzx = xyyx = yxxy \end{aligned}\right\} \begin{array}{c}\text{point groups} \\ 432,\ \bar{4}\text{3m and m}\bar{3}\text{m}\end{array} \tag{1.12}$$

[4] An overview of the tensor elements of the first-, second- and third-order susceptibility for all crystal systems can be found in Reference [36].

and

$$\left.\begin{aligned} xxxx &= yyyy = zzzz \\ yyzz &= zzxx = xxyy \\ zzyy &= xxzz = yyxx \\ yzyz &= zxzx = xyxy \\ zyzy &= xzxz = yxyx \\ yzzy &= zxxz = xyyx \\ zyyz &= xzzx = yxxy \end{aligned}\right\} \begin{array}{l}\text{point groups} \\ 23 \text{ and } \mathrm{m}\bar{3}\end{array} \tag{1.13}$$

respectively. [34, 36]

1.2 Two-photon absorption

The two-photon absorption (2PA) is a third-order nonlinear effect. It can be described in a simplified way as a quantum transition to an energetically higher level by the simultaneous absorption of two photons via an intermediate state[5]. As both, the initial and final state, are real, the energy of the two photons is transferred to the material by the absorption. The two photons, triggering the absorption, can either have the same or different frequencies, which then will be referred to as degenerate (D) or non-degenerate (ND) 2PA.

1.2.1 The two-photon absorption coefficient

In a linear medium the absorption and refraction is described by the complex refractive index

$$\tilde{n} = n + i\kappa \,. \tag{1.14}$$

The real part of $\tilde{n}$ is identical with the normal refractive index n. The imaginary part of $\tilde{n}$ is directly related to the linear absorption via the extinction coefficient κ which is in turn included in the linear absorption coefficient

$$\alpha = \frac{2\kappa\omega}{c} = \frac{4\pi\kappa}{\lambda} \,, \tag{1.15}$$

with angular frequency ω and wavelength λ. The linear absorption coefficient α directly quantifies the strength of a linear (one-photon) absorption. Due to the absorption, the light intensity exponentially decreases with increasing penetration depth y as described by the Lambert-Beer's law

$$I(y) = I_0 \, \mathrm{e}^{-\alpha y} \tag{1.16}$$

[5] Higher-order polarizations also lead to three-photon, four-photon and even multi-photon absorptions where more than two photons simultaneously trigger an electronic transition via several intermediate states.

with the initial intensity I_0 at $y = 0$ and α entering the law as the decay constant. [38]

Analogously to the imaginary part of the complex refractive index leading to a linear one-photon absorption, the imaginary part of the complex third-order susceptibility leads to a nonlinear absorption with two-photons. The strength of this nonlinear two-photon absorption can also be described by an absorption coefficient β, comparable to the linear absorption coefficient α. To derive that two-photon absorption coefficient a plane wave

$$E(y,t) = \frac{1}{2}E(y)\mathrm{e}^{-i(\omega t - ky)} + \text{c. c.} \tag{1.17}$$

propagating in y-direction with wave number k, electric field amplitude $E(y)$ and its complex conjugate (c. c.) is considered. Calculating the third-order electric polarization $P^{(3)}(y,t) = \epsilon_0\chi^{(3)}E(y,t)^3$ and inserting $E(y,t)$ and $P^{(3)}(y,t)$ in the nonlinear wave equation (1.4) one can obtain an equation describing the evolution of the field amplitude as a function of y given by

$$\frac{\mathrm{d}E(y)}{\mathrm{d}y}\mathrm{e}^{-i(\omega t-ky)} - \text{c.c.} = \frac{3}{8}\frac{i\omega}{cn}\chi^{(3)}|E(y)|^2E(y)\mathrm{e}^{-i(\omega t-ky)} - \text{c. c.}\,. \tag{1.18}$$

Within that calculation it is assumed that terms containing the second-order derivative with respect to y can be neglected (slowly-varying envelope approximation [39]) and only terms oscillating at ω are considered as higher harmonics are not part of a two-photon absorption process. Also the relations $\frac{1}{c^2} = \mu_0\epsilon_0$ with μ_0 the vacuum permeability and $k = \frac{\omega c}{n}$ are used. Defining the electric field amplitude as $E(y) = A(y)\exp(i\phi(y))$, where $A(y)$ and $\phi(y)$ are real quantities, and splitting the third-order susceptibility in real and imaginary part $\chi^{(3)} = \chi^{(3)}_{\mathrm{Re}} + i\chi^{(3)}_{\mathrm{Im}}$ one obtains the evolution of the nonlinear phase and field amplitude given by

$$\frac{\mathrm{d}\Phi(y)}{\mathrm{d}y} = \frac{3}{8}\frac{\omega}{cn}\chi^{(3)}_{\mathrm{Re}}A^2(y) \tag{1.19}$$

$$\text{and} \quad \frac{\mathrm{d}A(y)}{\mathrm{d}y} = -\frac{3}{8}\frac{\omega}{cn}\chi^{(3)}_{\mathrm{Im}}A^3(y)\,, \tag{1.20}$$

respectively. In the following the phase amplitude is disregarded, as an absorption only causes changes in the field amplitude during the propagation through a medium. By multiplying both sides of the nonlinear field amplitude evolution (1.20) with $2A(y)$ and using the precise proportionality between intensity $I(y)$ and the electric field amplitude $E(y)$

$$I(y) = \frac{1}{2}\epsilon_0 cn|E(y)|^2 \tag{1.21}$$

a differential equation

$$\frac{\mathrm{d}I(y)}{\mathrm{d}y} = -\beta_{\text{D-2PA}}I^2(y) \quad \text{with} \quad \beta_{\text{D-2PA}} = \frac{3\pi\chi^{(3)}_{\mathrm{Im}}}{\epsilon_0 cn^2\lambda} \tag{1.22}$$

can be derived. It describes the intensity decrease of an electromagnetic wave during the propagation in an otherwise transparent medium. Since the derivative of the intensity is proportional to the square of the intensity, here two photons with same frequency are simultaneously absorbed. The parameter $\beta_{\text{D-2PA}}$ describes the strength of that process and is therefore called the degenerate two-photon absorption coefficient. The solution of the differential equation (1.22) gives the intensity depending on the penetration depth y

$$I(y) = \frac{I_0}{1 + \beta_{\text{D-2PA}} I_0 y} \tag{1.23}$$

with the intensity I_0 at $y = 0$ comparable to the Lambert-Beer's law (1.16) for a linear one-photon absorption. [40]

A two-photon absorption can also be triggered by two photons of different frequencies ω_1 and ω_2. In that case, a pair of differential equations, similar to Equation (1.22),

$$\frac{\mathrm{d}I_1}{\mathrm{d}y} = -\beta_{11} I_1^2 - 2\beta_{12} I_1 I_2 \tag{1.24}$$

$$\frac{\mathrm{d}I_2}{\mathrm{d}y} = -\beta_{22} I_2^2 - 2\beta_{21} I_1 I_2 \tag{1.25}$$

can analogously be derived, which describe the decrease of the intensities I_1 and I_2 of the two electromagnetic waves, which are temporally and spatially overlapped in a nonlinear material. β_{11} and β_{22} are again the degenerate 2PA coefficients describing the absorption of two-photons of the same beam. β_{12} and β_{21} are the non-degenerate 2PA coefficients ($\beta_{\text{ND-2PA}}$), giving the strength of an absorption with either one photon of each beam. The factor of 2 ensures that the non-degenerate 2PA coefficient approaches the degenerate 2PA coefficient in the case of $I_2 \to I_1$ and $\omega_1 \to \omega_2$ [41]. Also in the non-degenerate case, $\beta_{\text{ND-2PA}}$ is directly related to the imaginary part of the third-order susceptibility. [42]

1.2.2 Two-photon absorption in semiconductors

A simultaneous absorption of two photons in a semiconductor usually triggers an electronic transition across the direct or indirect bandgap via an intermediate state. The two involved photons need to have at least a sum energy exceeding the bandgap energy. The process can be referred to as "simultaneous" as the lifetime of the intermediate state is less than a femtosecond according to the Heisenberg uncertainty principle $\Delta t \propto \hbar / E_{\text{g}}$ whereby $\hbar$ is the reduced Planck constant and E_{g} the bandgap energy which ranges between $1 - 3\,\text{eV}$ for typical semiconductors.

1.2.2.1 Scaling rules for direct semiconductors

Theoretical approaches

In semiconductors the behavior of the two-photon absorption coefficient under variation of certain parameters is of special interest since, for example, the dispersion of the 2PA coefficient is an important parameter for the optimization of semiconductor devices. Therefore, theoretical scaling rules for the degenerate and non-degenerate 2PA coefficient in direct semiconductors are introduced. Traditionally, these scaling rules have been studied by 2PA transition rate approaches. On the one hand, this is the second-order perturbative approach, which was firstly introduced by Maria Göppert-Mayer [2] in 1931; on the other hand, this is the tunnelling approach of L. V. Keldysh [43] from 1965. The latter uses first-order perturbation theory, taking into account the effects of an ac electric light field on the electronic energies and wave functions. The approach is limited to very simple semiconductor bandstructure models, even so leading to reasonable predictions of the 2PA scaling rules in direct semiconductors. In contrast, in the second-order perturbative approach, more sophisticated semiconductor bandstructure models are applicable[6]. In that formalism the two-photon absorption coefficient is related to the two-photon transition rate W_2 according to

$$\beta_{\text{D-2PA}}(\omega) = \frac{2\hbar\omega W_2^{\text{D}}}{I^2} \tag{1.26}$$

for degenerate transitions with one driving optical field of angular frequency ω and intensity I and

$$\beta_{\text{ND-2PA}}(\omega_1, \omega_2) = \frac{\hbar\omega_1 W_2^{\text{ND}}}{2 I_1 I_2} \tag{1.27}$$

for non-degenerate transitions with two driving optical fields of angular frequencies $\omega_1 \neq \omega_2$ and intensities I_1 and I_2. The two-photon transition rate W_2, known as Fermi's golden rule, is derived from second-order time-dependent perturbation theory and is in case of a degenerate 2PA

$$W_2^{\text{D}} = \frac{2\pi}{\hbar} \sum_{vc} \left| \sum_i \frac{\langle \psi_c | \hat{H}_{\text{opt}} | \psi_i \rangle \langle \psi_i | \hat{H}_{\text{opt}} | \psi_v \rangle}{E_{iv}(\mathbf{k}) - \hbar\omega} \right|^2 \delta(E_{cv}(\mathbf{k}) - 2\hbar\omega) \tag{1.28}$$

and in case of a non-degenerate 2PA

$$W_2^{\text{ND}} = \frac{2\pi}{\hbar} \sum_{vc} \left| \sum_i \left[\frac{\langle \psi_c | \hat{H}_{\text{opt},1} | \psi_i \rangle \langle \psi_i | \hat{H}_{\text{opt},1} | \psi_v \rangle}{E_{iv}(\mathbf{k}) - \hbar\omega_1} + \frac{\langle \psi_c | \hat{H}_{\text{opt},2} | \psi_i \rangle \langle \psi_i | \hat{H}_{\text{opt},2} | \psi_v \rangle}{E_{iv}(\mathbf{k}) - \hbar\omega_2} \right] \right|^2 . \cdot \delta(E_{cv}(\mathbf{k}) - \hbar\omega_1 - \hbar\omega_2) \tag{1.29}$$

[6] For an extensive comparison of both approaches in case of the degenerate 2PA scaling rules in direct semiconductors see, for example, References [42, 44].

The optical interaction Hamiltonian $\hat{H}_{\text{opt}}$ describes the perturbation by the coupling of the respective driving field to the semiconductor crystal potential. ψ_v and ψ_c denote the Bloch wave functions for the valence (v) and conduction band (c). E_{cv} is the energy difference between valence and conduction band and E_{iv} between valence band and intermediate state (i). The Bloch wave functions and energies are dependent on the crystal momentum $\mathbf{k}$. The conservation of energy is given by the δ-function. The summations are performed over all possible intermediate states and over all possible transitions starting from a filled state and ending at an empty state. In case of an intrinsic semiconductor this is usually a transition from the valence to the conduction band. The second-order perturbative approach vividly shows that the resulting 2PA coefficient and its scaling do not solely depend on the specific chosen approach, but in particular on the introduced bandstructure model, meaning which intermediate states can be addressed and over what transition channels the summations are performed. [15, 42, 45]
In addition to the transition rate approaches, further theoretical models exist for describing the nonlinear optical response, especially in case of the non-degenerate 2PA. For example, one model uses a susceptibility approach [46] while another is based on the semiconductor Bloch equations [47] to derive the scaling of the non-degenerate 2PA coefficient. Also these models are evaluated in the framework of a specific chosen bandstructure model.

Bandstructure models[7]

For a direct semiconductor the simplest approximation for a bandstructure is a two-band model with one parabolic valence and one parabolic conduction band (see Figure 1.1) [44, 45, 46, 47, 49, 50]. These bands are separated by the bandgap energy $E_{\text{g}} = E_{cv}(\mathbf{k} = 0)$ since the maximum of the valence band and the minimum of the conduction band are both located at the Γ-point. In this model the intermediate states for a 2PA lie within the valence or conduction band. Hence, this model enables two possible degenerate two-photon transitions, more precisely a combination of an interband transition across the fundamental bandgap and a preceding or succeeding intraband transition within the valence or conduction band (self-transition)[8]. According to the conditions for angular momentum conservation and the parity difference between the initial and final state, the interband transition at the Γ-point from the typically p-type valence band states to the s-type conduction band states is referred to as "allowed" whereas the self-transition is referred to as "forbidden". [42, 51]

[7] The references in this section which are directly given after the first mentioning of a specific bandstructure model refer to theoretical studies calculating the 2PA coefficient using this model.

[8] In case of a non-degenerate 2PA four different transitions are possible as the photons are distinguishable by their energies.

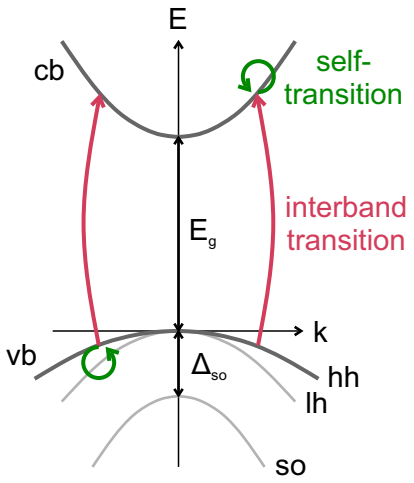

Figure 1.1: The simplest approximation for a bandstructure of a direct semiconductor is a two-band model (dark grey) with one parabolic valence (vb) and one parabolic conduction band (cb) separated by the bandgap energy E_g enabling allowed-forbidden two-photon transitions with a combination of an interband and a self-transition. The Kane bandstructure model [48] (dark + light grey) takes the threefold degeneracy of the valence band in heavy-hole (hh), light-hole (lh) and split-off (so) band separated by the spin-orbit interaction energy Δ_so into account and enables further transition channels (not shown here).

More realistic band models, as for example the Kane bandstructure model [48] (see also Figure 1.1), take the threefold degeneracy of the valence band in heavy-hole, light-hole and split-off band separated by the spin-orbit interaction energy Δ_so at $\mathbf{k} = 0$ into account [42]. Other models for example include higher conduction bands [6, 52]. The integration of further bands enables additional transition channels, for example, from either the valence band or conduction band to higher conduction bands. Next to the already described allowed-forbidden transition type, allowed-allowed and forbidden-forbidden transitions then have to be considered. Other refinements to the bandstructure include, for instance, the consideration of non-parabolic bands [44, 53, 54] and exciton effects [44, 52]. Nevertheless, also models without these refinements can still give reasonable predictions for the 2PA coefficient. Exciton effects, for example, only need to be included if the excess energy $\Delta E = 2\hbar\omega - E_\mathrm{g}$ for degenerate transitions and $\Delta E = \hbar\omega_1 + \hbar\omega_2 - E_\mathrm{g}$ for non-degenerate transitions is very small, otherwise the influence is negligible [49].

Scaling rules

Although there are numerous theoretical studies using different approaches and applying diverse bandstructure models, the results are consistent in that the excitation energies of the two photons and the semiconductor bandgap energy are the two most influencing

parameters on the scaling of the degenerate and non-degenerate 2PA coefficient. For the exact spectral dependence minor differences exist in literature while the bandgap scaling is beyond dispute. The absolute values for the 2PA coefficient deviate stronger between different studies. Here, an interpretation of the results under consideration of the specific framework is particularly important. Also, the comparison with experimental data has to be treated with care since the accordance of the experimental and theoretical constraints, such as the excess energy, has to be taken into account.

In the degenerate case various theoretical studies (see for example References [44, 45, 49]), all using a non-parabolic two-band model, independently derive for the scaling of degenerate 2PA coefficient

$$\beta_{\text{D-2PA}} \propto \frac{1}{n^2 E_\text{g}^3} F_2\left(\frac{\hbar\omega}{E_\text{g}}\right) \quad \text{with} \quad F_2(x) = \frac{(2x-1)^{3/2}}{(2x)^5} \,. \tag{1.30}$$

The dimensionless scaling function F_2 models the spectral dependence for allowed-forbidden transitions. The allowed-allowed and forbidden-forbidden transition type have a similar dependence only with a differing exponent in the numerator [55], but in general have very little influence on the degenerate two-photon absorption coefficient in direct semiconductors. Only for sum energies $2\hbar\omega$ just above the bandgap energy the allowed-allowed type and far away from the bandgap energy the forbidden-forbidden type gain slight influence [56]. Experimental studies validate the dominance over the other transition types since the experimental data fits well the scaling function F_2 for the allowed-forbidden type in various materials [57, 58, 59]. In Figure 1.2(a) F_2 is shown for various photon energies. The degenerate 2PA emerges at $2\hbar\omega = E_\text{g}$, when the sum energy of the two photons exceeds E_g. Going to higher photon energies, $\beta_{\text{D-2PA}}$ rapidly increases up to a maximum value at $\hbar\omega = 5/7 E_\text{g}$, followed by a smooth decrease. At $\hbar\omega = E_\text{g}$ (dashed line) linear absorption sets in and would superimpose the 2PA in experiments. In GaAs, for example, $\beta_{\text{D-2PA}}$ can be scaled up to maximum values of more than 10 cm/GW [58], $\beta_{\text{D-2PA}}$ of ZnSe is scalable up to approximately 7 cm/GW [57, 59].
As also seen in Equation (1.30), a scaling of the degenerate 2PA strength can also be achieved by choosing materials with different bandgaps. The E_g^{-3}-scaling is widely validated in experiments (see for example Reference [60]). Hence, going to very narrow-gap semiconductors like InSb with a bandgap energy of 0.18 eV [51], $\beta_{\text{D-2PA}}$ can be increased to a few cm/MW [61]. Nevertheless, the absolute values of $\beta_{\text{D-2PA}}$ for widely-used semiconductors, with bandgap energies ranging from 1 to 3 eV, remain in the order of a few cm/GW (see Figure 1.2(b)).

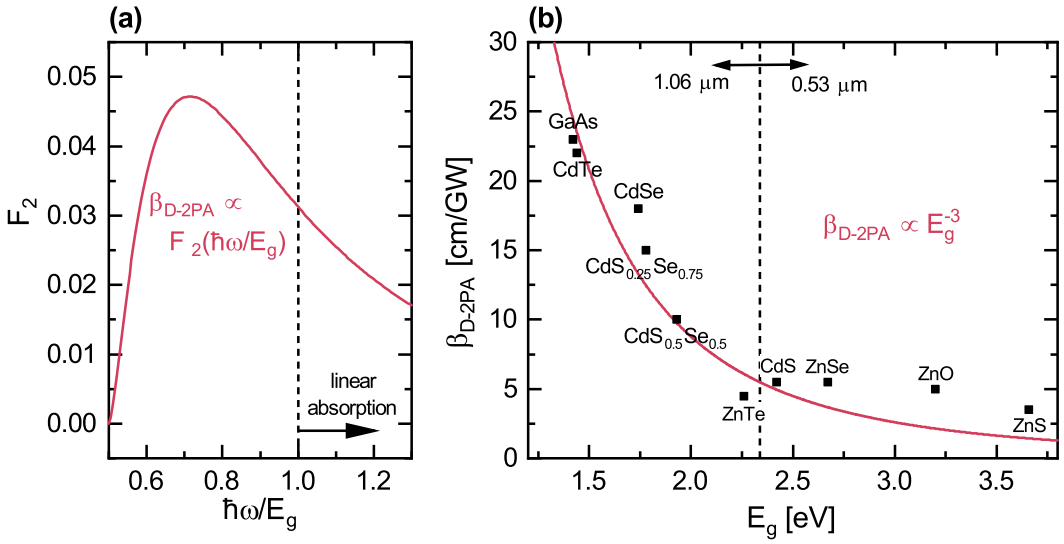

Figure 1.2: (a) The dimensionless function $F_2(\hbar\omega/E_\mathrm{g})$ models the spectral dependence of $\beta_\mathrm{D\text{-}2PA}$. (b) $\beta_\mathrm{D\text{-}2PA}$ for various direct semiconductors. The solid line represents a fit according to the E_g^{-3}-scaling. The data to the left (right) of the vertical dotted lined is acquired in degenerate experiments with photons of $\lambda = 1.06\,\mu\mathrm{m}$ ($\lambda = 0.53\,\mu\mathrm{m}$). Taken and adapted from Reference [60].

Consequently, in the degenerate case, the scaling of the 2PA strength is very limited if prototypical semiconductors like GaAs or ZnSe are used. Only comparably low nonlinearities can be achieved. For these materials a further scaling probability can be realized by using non-degenerate configurations with photons of different excitation energies[9]. Going to very non-degenerate configurations, theoretical scaling functions predict an enhancement of $\beta_\mathrm{ND\text{-}2PA}$ up to two to three magnitudes in contrast to the degenerate case. The explicit spectral dependence is slightly varying for different approaches. Three recent studies for direct semiconductors, which all use a simple two-band approximation, are the model of Hannes et al. [47] based on the semiconductor Bloch equations with **k**-independent dipole matrix elements which reveals

$$\beta_\mathrm{ND\text{-}2PA}(\omega_1,\omega_2) \propto \omega_1 \left(\frac{1}{\omega_1^2}+\frac{1}{\omega_2^2}\right)^2 , \tag{1.31}$$

the model of Sheik-Bahae et al. [49, 50] which calculates within a transition rate approach with **k**-dependent dipole matrix elements

$$\beta_\mathrm{ND\text{-}2PA}(\omega_1,\omega_2) \propto \frac{(\omega_1+\omega_2)^2}{\omega_1^3\omega_2^4} \tag{1.32}$$

[9] Also for non-degenerate configurations $\beta_\mathrm{ND\text{-}2PA}(\omega_1,\omega_2) \propto E_\mathrm{g}^{-3}$ holds true (see, for example, Reference [42]), but this again excludes the use of prototypical semiconductors.

and the model of Aversa et al. [46] using a susceptibility approach also with **k**-dependent dipole matrix elements which results into

$$\beta_{\text{ND-2PA}}(\omega_1, \omega_2) \propto \frac{(\omega_1 + \omega_2)^3}{\omega_1^3 \omega_2^4} \,. \tag{1.33}$$

In all three studies $\beta_{\text{ND-2PA}}$ exponentially increases if either $\hbar\omega_1$ or $\hbar\omega_2$ becomes small or accordingly if the ratio of the photon energies increases. The difference between those three approaches is especially seen for very non-degenerate configurations. Within the perturbative framework using a two-band model this enhancement can be vividly explained by the smaller energy photon becoming resonant to the forbidden intraband or self-transition and the larger energy photon to the allowed interband transition across the bandgap. The enhancement of the non-degenerate 2PA coefficient is limited by the linear one-photon absorption, when the larger energy photon approaches the bandgap energy. [19]

Experimentally, these predictions have so far been verified only for photon pairs where one photon is fixed and the other is varied in energy. For example, Fishman et al. [19] showed that in ZnSe for a photon energy ratio of 12.5 a 270-fold enhancement of the 2PA strength could be achieved when comparing to the corresponding degenerate coefficient at the average photon energy $(\hbar\omega_1 + \hbar\omega_2)/2$. For GaAs they obtained a 127-fold enhancement for a photon energy ratio of ten. In their experiments the small energy photon had a fixed energy at approximately 8 % and 10 % of the bandgap energy of ZnSe and GaAs, respectively. The large energy photon was varied in energy within the visible and near-infrared wavelength range. They compared the experimental data to the above introduced theoretical model of Sheik-Bahae et al. (see Equation (1.32)) and found good agreement. The results of Fishman et al. for ZnSe and GaAs are shown in Figure 1.3. Further experimental studies can be found in References [15, 17] among others. However, a systematic investigation of the non-degenerate 2PA coefficient, where the ratio of the photon energies is tuned away from unity while the sum energy $\hbar\omega_1 + \hbar\omega_2$ is kept constant so that always the same states in the conduction band are addressed, is still missing so far.

1.2.2.2 Scaling rules for indirect semiconductors

In an indirect semiconductor the maximum of the valence band and the minimum of the conduction band occur at different values of the crystal momentum **k** separated by the indirect energy gap E_{gi} (see Figure 1.4). Thus, a 2PA additionally needs to be accompanied by a simultaneous absorption or emission of a phonon providing the required crystal momentum to the electron. The energy to excite the electron from the valence to the

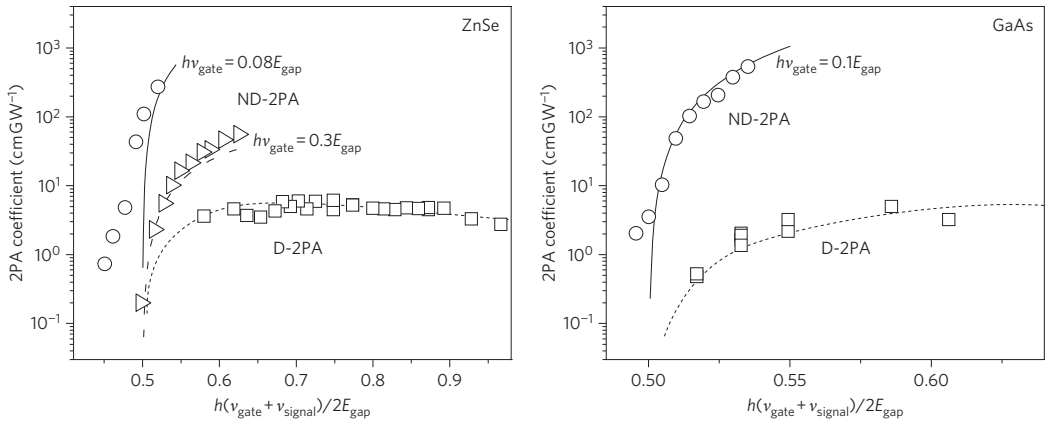

Figure 1.3: Fishman et al. investigated the non-degenerate 2PA in ZnSe (left) and GaAs (right) for the small energy photon ($\hbar\omega_{\text{gate}}$) fixed in energy and the large energy photon ($\hbar\omega_{\text{signal}}$) varied in energy. They found a strong enhancement for very non-degenerate configurations comparing to the degenerate case. The experimentally obtained scaling behaviour fits well the theoretical predictions (lines) of Sheik-Bahae et al. [49, 50]. Taken from Reference [19].

conduction band across the indirect bandgap E_{gi} is again provided by the sum energy of the two photons. The phonon energy E_{ph} contributes only little since it is at best a few tens of meV [51] and compared to the photon energies almost negligible. At $\mathbf{k} = 0$ the valence band states are again of p-type and the conduction band states of s-type whereas the conduction band states at the indirect bandgap at $\mathbf{k} \neq 0$ are a mixture of p- and s-type [51, 62]. In contrast to the 2PA in direct semiconductors, the 2PA in indirect semiconductors exhibits a temperature dependence because of the temperature dependent phonon occupation numbers [63].

Due to the additionally participating phonon, the strength of a 2PA in an indirect semiconductor is much lower than in a direct semiconductor. Nevertheless, a comprehensive understanding of the phonon-assisted 2PA is of special interest as there are various 2PA based applications using Si, the most prominent representative in the group of indirect semiconductors. Aside from technologies benefiting from the 2PA, in Si at 1310 nm and 1550 nm (the most common telecommunication wavelengths) the 2PA itself and the subsequently induced free-carrier absorption (see also Chapter 2.1.1) act as an undesirable loss mechanism at high optical intensities competing with actually desired nonlinearities [64]. Even so, less experimental and theoretical studies have been performed on phonon-assisted 2PA in contrast to studies on direct semiconductors, particularly the research on phonon-assisted non-degenerate 2PA is scarce. [65]

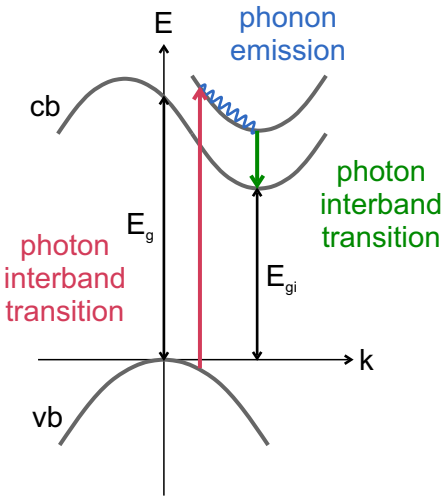

Figure 1.4: Bandstructure model of an indirect semiconductor with one parabolic valence band and two parabolic conduction bands separated by the indirect bandgap E_{gi} at $\mathbf{k} \neq 0$. The direct bandgap E_{g} at $\mathbf{k} = 0$ is larger than E_{gi}. One possible phonon-assisted 2PA out of many possible transition schemes is shown. It consists of an interband transition from the valence to the higher conduction band, followed by a phonon emission and finally an interband transition to the minimum of the valence band.

Comparable to direct semiconductors theoretical studies try to calculate scaling rules for the phonon-assisted 2PA coefficient. Also here, various approaches and bandstructure models are developed, showing that the excitation energies of the two photons as well are the most influencing parameters on the scaling of the phonon-assisted degenerate and non-degenerate 2PA coefficient[10].

The most recent theoretical study of Garcia et al. [55] applies a bandstructure model comprising one parabolic valence and two parabolic conduction bands. The degeneracy of the valence band is neglected. In Figure 1.4 the bandstructure model with one two-photon transition, out of many possible transitions, is shown. It consists of an interband transition from the valence to a higher conduction band, followed by a phonon emission and finally an interband transition from the higher conduction to the lowest conduction band. The approach of Garcia et al. yields a phonon-assisted degenerate 2PA coefficient in total consisting of three different dispersion relations depending on the transition type. In contrast to $\beta_{\text{D-2PA}}$ in direct semiconductors, the allowed-allowed and allowed-forbidden transition type are here not negligible for the scaling behavior. Nevertheless, the forbidden-forbidden

[10] Also the indirect bandgap is an influencing parameter on the scaling of the phonon-assisted 2PA coefficient. The exact dependence differs between theoretical studies and has not been experimentally determined. M. Dinu [63] calculates E_{gi}^{-3} as in direct semiconductors whereas Garcia et al. [55] proposes $E_{\mathrm{gi}}^{-3/2}$.

transition type is much weaker and peaks at excitation energies of $\hbar\omega \approx 5/2E_{\mathrm{gi}}$ when linear absorption already superimposes the 2PA. According to this, the overall phonon-assisted degenerate 2PA coefficient is given by

$$\beta_{\text{D-2PA}} = \sum_{n=0}^{2} \beta^{(n)} = \sum_{n=0}^{2} 2CF_2^{(n)} \left(\frac{\hbar\omega}{E_{\mathrm{gi}}} \right) \tag{1.34}$$

with C a material dependent constant (which can function as a fit parameter in comparison with experimental data) and $n = 0, 1, 2$ denoting the allowed-allowed, allowed-forbidden and forbidden-forbidden transition type, respectively. The factor 2 accounts for phonon absorption and emission. The spectral dependence F_2 is given by

$$F_2^{(n)}(x) = \frac{(2x-1)^{n+2}}{(2x)^5} \int_0^1 (1-x)^{n+\frac{1}{2}} x^{\frac{1}{2}} \, \mathrm{d}x \tag{1.35}$$

assuming $E_{\mathrm{ph}} \ll E_{\mathrm{gi}}$. The integral in $F_2^{(n)}(x)$ weights the influence of the specific transition type. It is $\frac{\pi}{8}$, $\frac{\pi}{16}$ and $\frac{5\pi}{128}$ for $n = 1, 2, 3$, respectively. In Figure 1.5 the function $F_2^{(n)}(\hbar\omega/E_{\mathrm{gi}})$ for each transition type and the summation $\sum_{n=0}^{2} F_2^{(n)}$ over all transition types are shown. The maxima of $F_2^{(n)}(x)$ for $n = 0, 1$ lie close-by at $\hbar\omega \approx 5/6E_{\mathrm{gi}}$ and $\hbar\omega \approx 5/4E_{\mathrm{gi}}$, respectively. The summation models the experimentally observable scaling behaviour of $\beta_{\text{D-2PA}}$ as all transition types contribute to the 2PA.

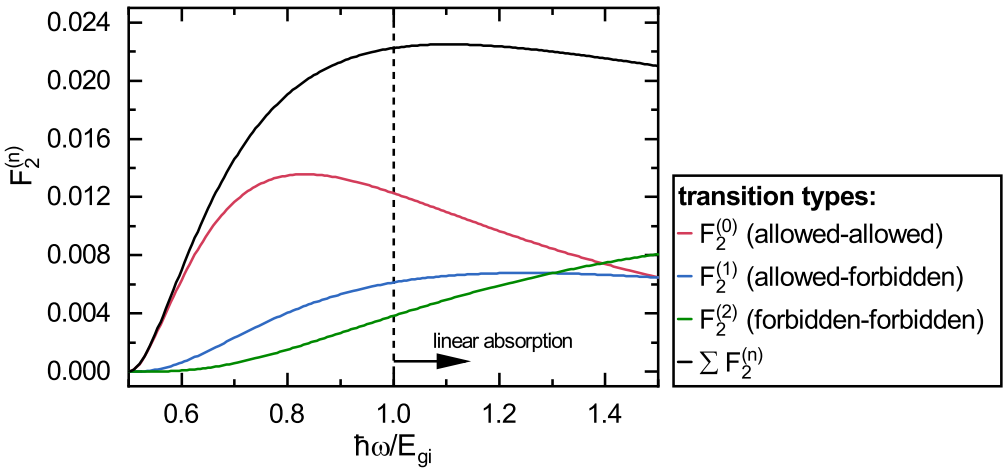

Figure 1.5: Spectral dependence $F_2^{(n)}(\hbar\omega/E_{\mathrm{gi}})$ of the phonon-assisted degenerate 2PA coefficient for the three different transition types assuming $E_{\mathrm{ph}} \ll E_{\mathrm{gi}}$. The forbidden-forbidden type contributes only little as the scaling would be experimentally observed.

The theoretical predictions for the scaling of the phonon-assisted degenerate 2PA coefficient are well in line with experimental observations. The measured 2PA coefficients of

Bristow et al. [66] in Si for excitation wavelengths $850\,\mathrm{nm} < \lambda < 2200\,\mathrm{nm}$ are compared with the theoretical results of Garcia et al. and show good agreement. Values for $\beta_{\text{D-2PA}}$ up to $\approx 2.5\,\frac{\mathrm{cm}}{\mathrm{GW}}$ were observed. A comparable study of Lin et al. [67], also in Si and using the same wavelength range, shows a similar trend for $\beta_{\text{D-2PA}}$, although a definite comparison with theory is missing there. The absolute 2PA coefficients of Lin et al. are overall smaller ($< 0{,}6\,\frac{\mathrm{cm}}{\mathrm{GW}}$). The theory of Garcia et al. was further confirmed for indirect transitions in Ge using the experimental data of Seo et al. [68, 69]. Followingly, also the phonon-assisted degenerate 2PA coefficients are scalable by changing the excitation energy, as in case of direct semiconductors, but also do not exceed a few cm/GW.

These limits can also be extended by using non-degenerate configurations. The joint study of Sanaz Faryadras and Cox et al. [23, 24], so far the only one, theoretically calculates the scaling of the phonon-assisted non-degenerate 2PA coefficient. By comparing their results with experimental data, they find the allowed-allowed transition type describing the scaling behavior best. Assuming $E_{\text{ph}} \ll E_{\text{gi}}$, the phonon-assisted non-degenerate 2PA coefficient is accordingly given by

$$\beta_{\text{ND-2PA}}(x_1, x_2) = \frac{D}{n_1 n_2} \frac{1}{x_1 x_2^2} \left(\frac{1}{\frac{E_{\text{g}}}{E_{\text{gi}}} - x_1} + \frac{1}{\frac{E_{\text{g}}}{E_{\text{gi}}} - x_2} \right)^2 \left(\frac{1}{x_1 + x_2} \right)^2 (x_1 + x_2 - 1)^2 \quad (1.36)$$

with $x_{1,2} = \frac{\hbar\omega_{1,2}}{E_{\text{gi}}}$ and D a scaling parameter to be determined by comparison with experimental data. Faryadras and Cox et al. further distinguish between specific pathways of the allowed-allowed type. The dominating pathway, described by Equation (1.36), is an interband transition across the direct bandgap at $\mathbf{k} = 0$, followed by a downward transition back to the valence band maximum (both transitions induced by a photon) and finally a phonon-assisted interband transition to the minimum of the conduction band. The measurements for validation were performed with one photon at a fixed wavelength (1700 nm, 1900 nm, 2400 nm) while the other one varied in wavelength between 1150 nm and 1500 nm. Since the non-degenerate 2PA coefficient should also lead to the degenerate 2PA coefficient with $\omega_1 = \omega_2$ they also used the degenerate data of Bristow et al. [66] for comparison. Nevertheless, the authors remark that due to the limited experimental data further examinations could add some more transitions paths, leading to a final scaling that describes the experimental data even better. Therefore, systematic studies with varying ω_1/ω_2 at a constant sum energy could be very useful. So far only phonon-assisted non-degenerate 2PA data at discrete wavelength configurations, especially in Si waveguides at the telecommunication wavelengths [20, 21, 22], is available. However, they do not pursue to validate the scaling behavior but rather address other questions. Within the study

of Faryadras and Cox et al. for the most non-degenerate configuration at 1150 nm and 2400 nm a 2PA coefficient of about 1.2 cm/GW was reached.

All in all, the frequency ratio of the two involved photons is the most influencing parameter to enlarge the 2PA strength in direct and indirect semiconductors within one material. Especially the scaling probability for non-degenerate configurations is very large. The specific scaling functions deviate due to the different dominating transition type(s). In direct semiconductors very high non-degenerate 2PA coefficients in the range of cm/MW can be achieved. Because of the additionally participating phonon, the enhancement in indirect semiconductors still remains in the order of cm/GW due to the overall smaller 2PA absorption strength.

1.2.2.3 Anisotropy

In cubic semiconductors, the linear one-photon absorption strength is equivalent along all crystal axes. There are no differences for linear, circular or elliptical polarized light. In contrast, the 2PA is dependent on the crystallographic orientation and the polarization of the driving fields. It is anisotropic. This anisotropy stems from the third-order susceptibility tensor, more precisely its specific tensor elements, since $\chi^{(3)}_{\mathrm{Im}}$ is directly proportional to the (non-)degenerate 2PA coefficient (see Chapter 1.2.1). $\chi^{(3)}_{\mathrm{Im}}$ exhibits off-diagonal elements which introduce the anisotropy, whereas the linear susceptibility tensor $\chi^{(1)}$ is a scalar quantity and thus isotropic (see Chapter 1.1.2).
Various theoretical and experimental studies have investigated the 2PA anisotropy, mainly for degenerate driving fields[11]. The approaches are versatile and examine different aspects. The main results for direct semiconductors are:

(i) Varying the (linear) polarization of the two driving fields with respect to a specific crystal axis most often leads to a periodically modulated 2PA coefficient. [26, 27, 28, 29] (orientation anisotropy)

(ii) The specific polarization of the driving fields (linear, circular, elliptical) and their relative orientation with respect to each other highly influences the degenerate 2PA strength. [25, 26, 42, 70, 71] (polarization anisotropy)

(iii) The ratio of the 2PA coefficient in different states of polarization, for example $\beta_{\mathrm{linear}}/\beta_{\mathrm{circular}}$, is dependent on the specific excitation energies. [70, 71, 72]

[11] In the context of anisotropy the term "non-degenerate" sometimes refers to a configuration where the two driving fields have the same wavelengths but different polarizations. Here, the term is used for different wavelengths only.

(iv) The 2PA anisotropy effects are less significant in semiconductors with smaller bandgap energies. [26, 70, 71]

Theoretical studies have further shown that calculations using a two-band model are not able predict the 2PA anisotropy, although this model can successfully describe the scaling of the 2PA coefficient as introduced in Chapters 1.2.2.1 and 1.2.2.2. Only the extension to a model with at least the next higher conduction band can account for 2PA anisotropy effects. The influence of this higher conduction band is threefold: "First, the mixing of the upper conduction states with the lower conduction and valence bands perturbs the energies leading to anisotropic bands and spin splitting. Second, the upper conduction-band wave functions [...] mix with the lower states and so modify the optical coupling between the lower states. Third, the upper conduction-band states appear as additional intermediate levels in the two-photon absorption." [71]. For very narrow gap semiconductors the influence of the additionally considered conduction band vanishes as the energy gap to the lowest conduction band increases. In that case, the band structure approaches the isotropic limit which underlines the less significant anisotropy for small bandgap semiconductors like InSb. [70, 71, 72]

Few experimental studies, especially for Si, partially give rise to similar characteristics of the 2PA anisotropy in indirect semiconductors [30, 31, 32, 33]. Anyhow, for a reliable validation further experimental data needs to be accumulated. Theoretical studies are entirely lacking so far.

Due to the anisotropy effects it is absolutely essential in every 2PA study to precisely describe the specimen orientation and the polarization of the driving fields. In many studies this information is missing so that a comparison of absolute values of the 2PA coefficient is hardly possible. For example, Dvorak et al. showed that the degenerate 2PA coefficient of GaAs at 950 nm varies between 19.5 cm/GW and 27 cm/GW if the two incident beams are either polarized along the [001] or the [110] crystallographic axis[12], respectively. Comparing two configurations where the two incident beams were either polarized parallel or perpendicular to each other gave values of 19.5 cm/GW and 8 cm/GW, respectively. [26]

[12]The notation $[uvw]$, according to the Miller indices [73], refers to a specific direction vector $u\vec{x}_1 + v\vec{x}_2 + w\vec{x}_3$ with the basis vectors $\vec{x}_i$ of the real or reciprocal lattice, depending on which lattice is referred to.

Chapter 2

Experimental Setup and Sample Characterization

This chapter gives a comprehensive overview on the experimental setup and the specifically used main experimental methods in detail. The characteristics are described, advantages and challenges are elucidated. The chapter completes with a thorough presentation of the three investigated semiconductors ZnSe, GaAs and Si.

2.1 Experimental methods

The three main experimental concepts are the measurement of the non-degenerate two-photon absorption strength, the knife-edge method which is used for measuring the spot size of a laser beam and the 2PA based autocorrelation technique to determine the pulse lengths. The spot sizes and pulse lengths are required for the analysis of the two-photon absorption strength measurements, thus the determination of the 2PA coefficients. The operating principle of the 2PA autocorrelator is of further interest since it is an application based on 2PA.

2.1.1 Non-degenerate two-photon absorption measurement

The non-degenerate two-photon absorption strength is measured in a pump-probe scheme where two pulsed laser beams with photon energies $\hbar\omega_{\mathrm{probe}}$ and $\hbar\omega_{\mathrm{pump}}$ are spatially and temporally overlapped at the sample location under a variably adjustable time delay τ_{d}. After the sample the transmittance of the probe beam is detected and the pump beam is blocked. Within the sample the two beams can be assumed to be parallel, since refraction further decreases the anyway small angle between the two beams in front of the sample.

With this concept the 2PA strength can be directly measured from the attenuation of the signal beam. Figure 2.1 shows a schematic representation of the experimental setup.

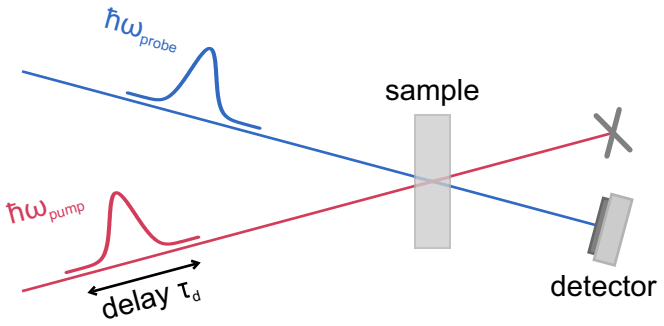

Figure 2.1: Schematic representation of a non-degenerate 2PA experimental setup in pump-probe fashion with a weak probe pulse $\hbar\omega_{\mathrm{probe}}$ and strong pump pulse $\hbar\omega_{\mathrm{pump}}$.

In order to induce the non-degenerate 2PA with one photon from each beam and to suppress the degenerate 2PA with two photons from the same beam, the photon energies are preferably chosen to be

$$\frac{E_{\mathrm{g(i)}}}{2} < \hbar\omega_{\mathrm{probe}} < E_{\mathrm{g(i)}} \quad \text{and} \quad \hbar\omega_{\mathrm{pump}} < \frac{E_{\mathrm{g(i)}}}{2} \quad .$$

With this choice, the strong pump beam alone cannot trigger an interband transition with two of its photons. Additionally, a low intensity is set for the probe beam that itself alone does not induce significant degenerate 2PA.

Figure 2.2 shows simulated 2PA pump-probe traces for a 70 µm thick ZnSe specimen as a function of the time delay τ_{d}. The traces are given for frequency ratios $\omega_{\mathrm{probe}}/\omega_{\mathrm{pump}} = \{1.00, 1.14, 1.33, 1.6, 2.0, 2.67, 4.00\}$ with a constant sum energy of 3.10 eV. The simulations are based on an analytical model for the pump-probe traces of Raluca A. Negres et al. [74], which will be further explained in Chapter 3.1.1. The involved photons both have pulse lengths of 100 fs (FWHM)[1] and the pump intensity is 0.06 GW/cm^2. Since the 2PA coefficient scales with the frequency ratio $\omega_{\mathrm{probe}}/\omega_{\mathrm{pump}}$, the respective values are $\beta\,[\mathrm{cm/GW}] = \{3.8, 4.2, 4.9, 6.5, 10.2, 20.1, 67.3\}$[2]. The linear absorption is assumed to be zero. The refractive indices are taken from Reference [75]. These 2PA pump-probe traces exemplify their characteristic appearance in general and can be adopted to other materials,

[1] Subsequently, the pulse lengths will be either given as full width at half maximum (FWHM) or half width at 1/e maximum (HW$^1/_e$M). The more current term is the FWHM even so the HW$^1/_e$M is used for the analysis of the pump-probe traces in Chapter 3.1.1. The two lengths can be converted into each other by $\mathrm{FWHM} = 2\sqrt{\ln 2} \cdot \mathrm{HW}^1/_e\mathrm{M} \approx 1.665 \cdot \mathrm{HW}^1/_e\mathrm{M}$.

[2] The 2PA coefficients are based on the measurement results of the (100)-oriented ZnSe sample described in Chapter 3.2.

sample thicknesses or photon pair characteristics such as pulse lengths. In the following the pump-probe traces are described in detail.

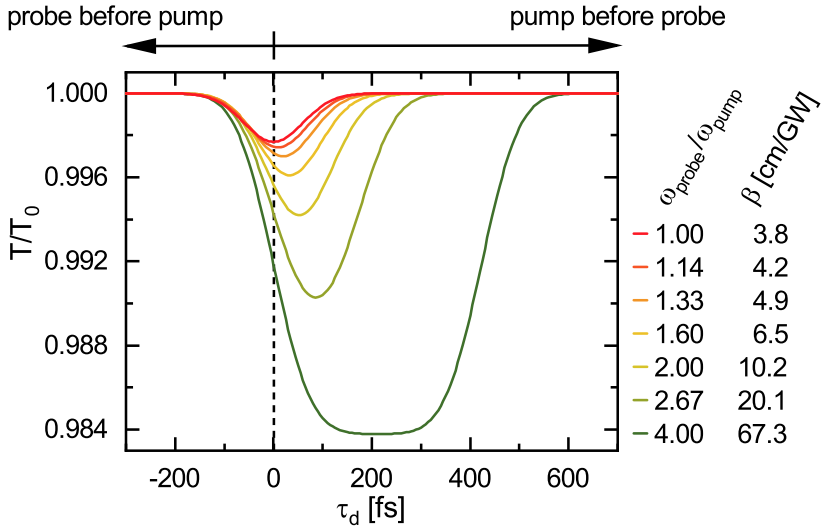

Figure 2.2: Simulated 2PA pump-probe traces in ZnSe for frequency ratios $\omega_{\mathrm{probe}}/\omega_{\mathrm{pump}} = \{1.00, 1.14, 1.33, 1.60, 2.00, 2.67, 4.00\}$ with a constant sum energy of 3.10 eV. The related values for the 2PA coefficient are $\beta\,[\mathrm{cm/GW}] = \{3.8, 4.2, 4.9, 6.5, 10.2, 20.1, 67.3\}$. The red colored graph represents the degenerate and the dark green colored graph the most non-degenerate configuration.

Independent from the degree of non-degeneracy the rising and falling slope of the pump-probe traces correspond to the convolution of the involved pulses. The exemplary pump-probe traces in Figure 2.2 exhibit Gaussian shapes because the involved pulses also have Gaussian profiles. In the degenerate case at $\omega_{\mathrm{probe}}/\omega_{\mathrm{pump}} = 1$ the transmission is minimal at $\tau_{\mathrm{d}} = 0$. The probe and pump pulse spatially and temporally overlap over the whole sample length. In the non-degenerate case the two pulses propagate through the sample at different velocities since the group velocity of a pulse is strongly dependent on its wavelength. Thus, at $\tau_{\mathrm{d}} = 0$ the faster pump pulse outruns the slower probe pulse so that only a very small 2PA signal can be detected. For this reason, the minimum of the transmission curve is shifted to delay times $\tau_{\mathrm{d}} > 0$ where the pump pulse overtakes the probe pulse within the sample length and thus a maximal 2PA signal is observable. Additionally, the group velocity mismatch shortens the overlap distance relatively to the sample thickness so that the measured amplitude of the transmission curve decreases. Nevertheless, this effect cannot be observed in the transmission curves, since the 2PA absorption strength increases with increasing ratio of $\omega_{\mathrm{probe}}/\omega_{\mathrm{pump}}$. Summarizing both effects this still leads

to an overall increase of the amplitude. Further on, several initial delay times occur where probe and pump pulse walk through each other within the sample thickness, so that the 2PA signal broadens and a plateau at the maximum amplitude is formed. This emerging effective overlap distance can also be observed if the frequency ratio $\omega_{\text{probe}}/\omega_{\text{pump}}$ is kept constant and the sample thickness is increased. In this case, an overlap of the two pulses is even possible for larger delay times, which also results in the formation of a plateau. The broadening of the individual pulses as they pass through the sample, due to the group velocity dispersion (GVD), is particularly important for very short pulses with a broad frequency spectrum or very thick samples. [18, 74, 76]

The 2PA measurements can be accompanied by free-carrier absorption (FCA). The free-carrier absorption is a subsequent intraband absorption process of already two-photon excited "free" carriers (electrons or holes) to another unoccupied state in the same band. Especially early studies on degenerate 2PA, with relatively long pulses in the picosecond-range, were influenced by a significant high FCA which had to be included in the calculation of the 2PA coefficients as otherwise misleading results occurred. Therefore, Bechtel et al. [77] introduced a critical intensity when the attenuation due to free-carrier absorption is comparable to the attenuation by degenerate 2PA given by

$$I_{\text{cr}} = \frac{2\hbar\omega}{\sigma_{\text{h}}\tau(1-R)} \tag{2.1}$$

with τ the pulse length (HW$^1/_e$M), σ_{h} the free hole absorption cross section[3] and R the reflectivity. In more recent studies the contribution of FCA has diminished since the use of shorter pulses in the femtosecond-range has increased the critical intensity I_{cr} to a level which goes far beyond the actual intensities used in experiments.
In non-degenerate 2PA measurements the FCA of probe and pump photons can be introduced by carriers preliminary excited due to non-degenerate or (if it is not energetically excluded) degenerate 2PA. Significant FCA of probe photons introduced by carriers preliminary excited due to degenerate 2PA of the pump pulse would result into a slower rising slope after the temporal overlap and thus to unsymmetrical pump-probe traces. For this reason, the appearance of the pump-probe traces allows to directly monitor if there is degenerate 2PA of pump photons and subsequent FCA of probe photons. FCA of probe photons introduced by non-degenerate two-photon excited carriers would result into a further transmission decrease when probe and pump pulse temporally overlap but which is

[3] Usually the dominant secondary absorption is by free holes. σ_h is in the order of $10^{-17}\,\text{cm}^2$ for typical semiconductors like GaAs. [77]

unlikely since pulse lengths in the femtosecond-range are used[4]. The FCA of pump photons is not captured in the pump-probe traces but can equally be estimated as non-relevant due to the idler pulse lengths also in the femtosecond-range. Of course, the critical intensity I_{cr} can also be used to estimate the significance of the FCA.

2.1.2 Knife-edge method

The knife-edge method is used to determine the diameter of a laser beam [78]. The main advantages of this method are its simplicity and usability over a wide wavelength range, which depends solely on the choice of a suitable detector. To acquire a knife-edge measurement, an optically opaque material with a sharp edge, for example a razor blade, is translated across the beam perpendicular to the propagation direction. After the blade, the mean power dependent on the blade position is detected. The recorded characteristic power profile provides the information about the beam diameter. A representation of the experimental setup can be seen in Figure 2.3.

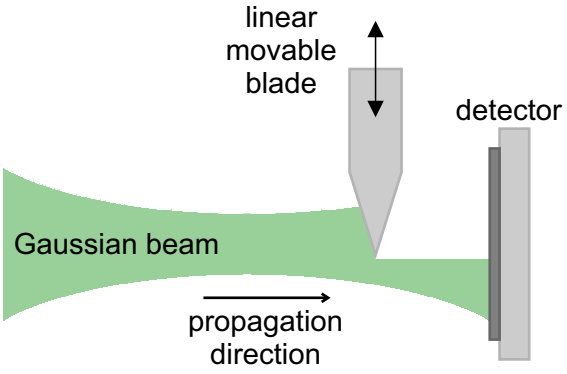

Figure 2.3: Schematic representation of the experimental setup for the determination of the laser beam diameter via knife-edge method.

The power profile is evaluated assuming a Gaussian intensity profile according to the Gaussian beam optics [79]

$$I(x,y) = I_0 \exp\left[-\frac{4(x+y)^2}{d^2}\right] \tag{2.2}$$

in the $xy-$plane perpendicular to the propagation direction (see Figure 2.4), where I_0 describes the maximum intensity and d the diameter of the beam at which the maximum

[4]Here, the same probe pulse on the one hand excites the carriers via non-degenerate 2PA and on the other hand provides photons for the FCA. This is why this effect can only be observed at the temporal overlap.

intensity has decreased to I_0/e (FW^1/$_e$M). If the blade is translated into the beam in the positive x'-direction, the power is calculated as a function of the blade position x in the beam given by

$$\begin{aligned} P(x) &= \int_{-\infty}^{\infty}\int_{x}^{\infty} I(x',y)\,\mathrm{d}x'\mathrm{d}y \\ &= \frac{1}{2}P_{\max}\left(1-\mathrm{erf}\left(\frac{2x}{d}\right)\right)\ , \end{aligned} \tag{2.3}$$

with the Gaussian error function $\mathrm{erf}(x) = \frac{2}{\sqrt{\pi}}\int_0^x e^{-\tau^2}\mathrm{d}\tau$ [80]. In this case, the beam is not covered by the blade at the beginning of the measurement (see Figure 2.4). Otherwise, with the beam completely covered, the sign in front of the error function changes. The maximum power $P_{\max}$ without the blade is

$$P_{\max} = \int_{-\infty}^{\infty}\int_{-\infty}^{\infty} I(x',y)\,\mathrm{d}x'\mathrm{d}y = \frac{\pi}{4}I_0 d^2\ . \tag{2.4}$$

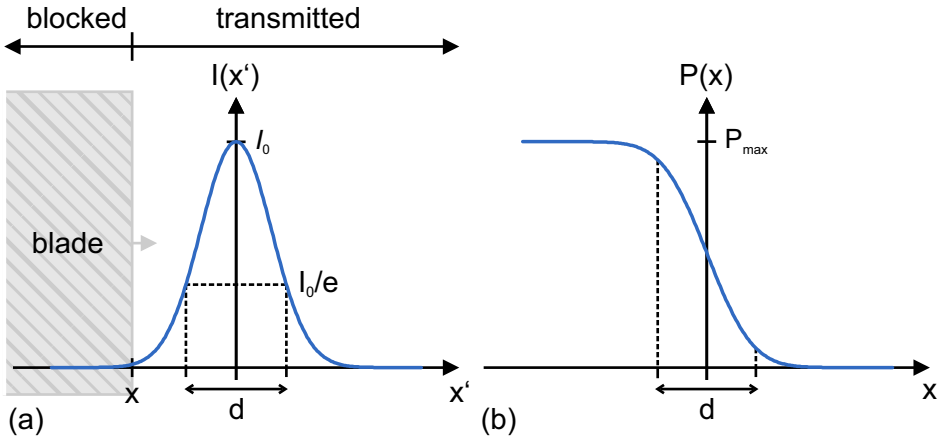

Figure 2.4: (a) Radial intensity profile $I(x')$ and (b) characteristic power profile $P(x)$ dependent on the blade position with d the diameter of the beam at which the intensity has decreased to I_0/e.

2.1.3 Two-photon absorption based autocorrelator

The optical autocorrelation is a method to determine the temporal width of ultrashort laser pulses as shortly described in the Introduction. In general, to measure a time interval it needs to be scanned with an even shorter time interval. In case of laser pulses down to a few femtoseconds there are no suitable standard electronics available, since the response times of, for example, photodiodes and oscilloscopes are too slow. The optical autocorrelation technique solves this problem by splitting the femtosecond pulses into two parts,

so that the pulse can be scanned with a duplicate of itself to reach the required time scales.

The experimental setup of an interferometric autocorrelator is based on a Michelson interferometer (see Figure 2.5). The input beam is split into the two arms of the interferometer by a centrally arranged beamsplitter. One part of the pulse train is temporally delayed, in the simplest case, for example, via a movable mirror. Afterwards, the two parts pass the beamsplitter again, are thus recombined and collinear superimposed. The recombined pulse trains are multiplied via a nonlinear process and the autocorrelation signal generated in this way is detected and analyzed as a function of the delay time between the two pulse trains.

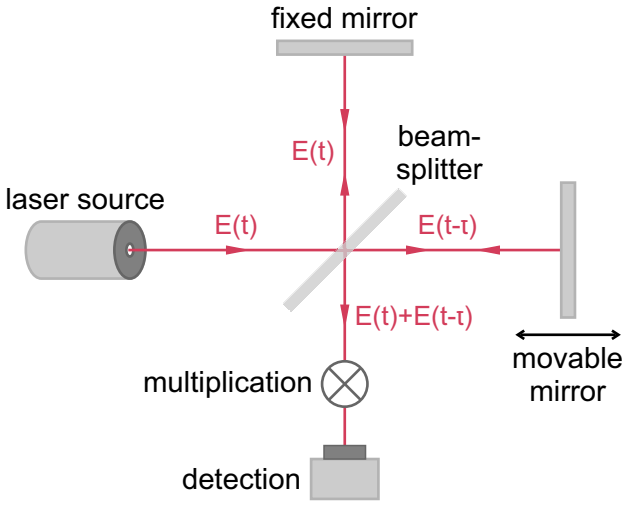

Figure 2.5: Schematic representation of an interferometric autocorrelator

The interferometric autocorrelation intensity profile $I_{\mathrm{IAC}}(\tau)$ for a pulse with the electric field $E(t)$ is given by

$$I_{\mathrm{IAC}}(\tau) = \int_{-\infty}^{\infty} \left| [E(t) + E(t-\tau)]^2 \right|^2 \, \mathrm{d}t \, . \tag{2.5}$$

Expanding the term in the bracket yields to an intensity profile consisting of four contributions

$$I_{\mathrm{IAC}}(\tau) = \int_{-\infty}^{\infty} I^2(t) I^2(t-\tau) \, \mathrm{d}t \quad \text{(constant background)} \tag{2.6}$$

$$+ 4 \int_{-\infty}^{\infty} I(t) I(t-\tau) \, \mathrm{d}t \quad \text{(intensity autocorrelation)} \tag{2.7}$$

$$+ 2 \int_{-\infty}^{\infty} (I(t) + I(t-\tau)) \, \mathrm{Re}[E(t) E^*(t-\tau)] \, \mathrm{d}t \quad (\omega\text{-interference term}) \tag{2.8}$$

$$+ \int_{-\infty}^{\infty} \mathrm{Re}[E^2(t)E^{*2}(t-\tau)]\,\mathrm{d}t \quad (2\omega\text{-interference term}) \tag{2.9}$$

with $I(t) = |E(t)|^2$ and * denoting the complex conjugate. The background term gives a constant offset corresponding to the self-multiplication of each individual pulse independent from the time delay. The convolution integral in the second term determines the intensity autocorrelation $I_{\mathrm{AC}} = \int_{-\infty}^{\infty} I(t)I(t-\tau)\,\mathrm{d}t$ from which the temporal pulse width can be deduced. The two interference terms appear as the electric fields of the two pulse trains can be superimposed constructively or destructively depending on the mutual phase position, adding interference fringes oscillating at ω and 2ω to the interferometric autocorrelation profile. [81, 82]

To determine the temporal width of the initial pulse, its specific pulse profile needs to be known. Assuming, for example, an initial pulse with a Gaussian intensity profile

$$I(t) = \mathrm{e}^{-t^2} \tag{2.10}$$

the intensity autocorrelation signal also has a Gaussian profile given by

$$I_{\mathrm{AC}}(\tau) = \sqrt{\frac{\pi}{2}}\mathrm{e}^{-\frac{\tau^2}{2}}\,. \tag{2.11}$$

Evaluating $I(t)$ and $I_{\mathrm{AC}}(\tau)$ at half of their amplitudes gives the time value at half width (HWHM) and accordingly by doubling the value at full width at half maximum (FWHM)

$$I(t_{\mathrm{HWHM}}) = \frac{1}{2} \quad \Rightarrow \quad t_{\mathrm{FWHM}} = 2\sqrt{\ln(2)} \quad \text{and} \tag{2.12}$$

$$I_{\mathrm{AC}}(\tau_{\mathrm{HWHM,\,AC}}) = \frac{1}{2}\cdot\sqrt{\frac{\pi}{2}} \quad \Rightarrow \quad \tau_{\mathrm{FWHM,\,AC}} = 2\sqrt{2\ln(2)}\,. \tag{2.13}$$

Hence, the transformation factor between the FWHM of the initial pulse and its autocorrelation signal is given by $\frac{t_{\mathrm{FWHM}}}{\tau_{\mathrm{FWHM,\,AC}}} = 0.71$.

The most commonly used method to nonlinearly multiply the two pulse trains is the second-harmonic generation. Here, the two pulse trains are superimposed in a nonlinear crystal and an autocorrelation signal at twice the initial frequency is generated which is then passed on to a detector. To achieve sufficient signal strengths interaction distances, longer than hundreds of the incident wavelength, are required which makes the nonlinear crystal relatively bulky. To further enlarge the autocorrelation signal, phasematching conditions, to conserve the photon momentum between the input waves and the output wave, need to be fulfilled. An alternative to second-harmonic generation based autocorrelators are autocorrelators based on 2PA. Here, the nonlinear crystal and the detector can be

replaced by a single semiconductor detection unit, since the 2PA transforms an optical signal directly into an electrical signal through the transition of charge carriers. As long interaction distances and phasematching are not required, the 2PA detectors are comparatively thin so that also undesirable broadening of the pulses due to GVD is negligible. Furthermore, inexpensive standard devices such as photodiodes can be utilized. The 2PA based autocorrelators are additionally easier in handling and adjustment. Detector materials for a wide wavelength range of operation are available as the 2PA is not limited by the narrow phasematching bandwidth. [8, 9]

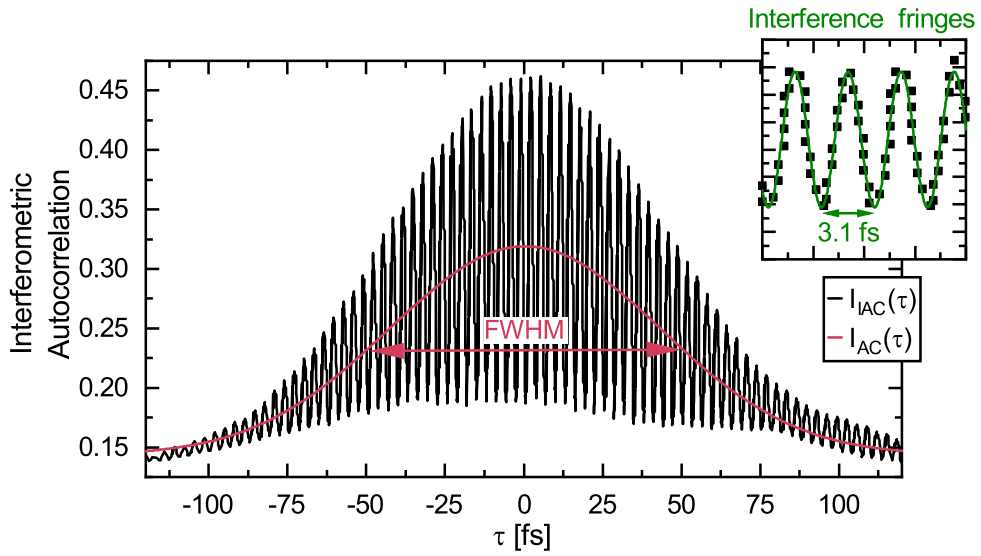

Figure 2.6: Interferometric autocorrelation signal $I_{\mathrm{IAC}}(\tau)$ detected with a commercial interferometric autocorrelator based on 2PA. The red line represents a Gaussian fit to the low-pass filtered signal representing the intensity autocorrelation term I_{AC} with $\tau_{\mathrm{FWHM,\,AC}} = 101.1\,\mathrm{fs}$. Accordingly, the temporal width of the initial pulse is $t_{\mathrm{FWHM}} = 71.8\,\mathrm{fs}$. The detailed view shows the interference fringes with a peak to peak distance of $\Delta\tau = 3.1\,\mathrm{fs}$ corresponding to a wavelength of 940 nm as determined with a spectrometer.

In Figure 2.6 an interferometric autocorrelation signal $I_{\mathrm{IAC}}(\tau)$ for a 940 nm pulse with Gaussian profile is shown. It was detected with the commercial interferometric autocorrelator APE Mini TPA based on 2PA. The interferometric autocorrelation signal $I_{\mathrm{IAC}}(\tau)$ is low-pass filtered and fitted with a Gaussian profile, representing the intensity autocorrelation term $I_{\mathrm{AC}}(\tau)$ with a width of $\tau_{\mathrm{FWHM,\,AC}} = 101.1\,\mathrm{fs}$. Accordingly, the initial pulse width is $t_{\mathrm{FWHM}} = 71.8\,\mathrm{fs}$. The detailed view shows the interference fringes with a peak to peak distance of $\Delta\tau = 3.1\,\mathrm{fs}$ corresponding to a wavelength of $\lambda = c\Delta\tau = 940\,\mathrm{nm}$, consistent

with a spectrometer measurement. The constant offset corresponds to the self-induced 2PA of each pulse train in the two interferometer arms.

2.2 Experimental setup

The experimental setup for the two-photon absorption measurements is based on a laser system consisting of a titanium:sapphire mode-locked oscillator (Coherent Micra), a titanium:sapphire regenerative amplifier (Coherent RegA) and a pump laser (Coherent Verdi). The RegA system emits ultrashort laser pulses with a central wavelength of $\lambda_{\mathrm{RegA}} = (790 - 800)\,\mathrm{nm}$, a pulse length of $\tau_{\mathrm{RegA}} \approx 60\,\mathrm{fs}$ (FWHM) and a pulse energy of $E_{\mathrm{RegA}} = 8000\,\mathrm{nJ}$ at a repetition rate of $f_{\mathrm{RegA}} = 250\,\mathrm{kHz}$.

The pulses provided by the RegA system are coupled into an optical parametric amplifier (OPA) and used on the one hand as a pump pulse with the frequency $\omega_{\mathrm{pump}}^{\mathrm{OPA}}$ and on the other hand to generate a white light continuum. The white light continuum is overlaid with the intense pump pulse in a nonlinear crystal. Depending on the phase matching conditions, meaning practically the adjustment of the phase matching angle, a specific frequency ω_{sig} of the white light continuum is amplified through the pump pulse. Additionally, a further pulse at the difference frequency $\omega_{\mathrm{idl}} = \omega_{\mathrm{pump}}^{\mathrm{OPA}} - \omega_{\mathrm{sig}}$ is generated. After the first pass of the pump and signal pulse through the nonlinear crystal, the pulses pass through the crystal a second time for further amplification. Then, the signal, idler and residual pump pulse exit the OPA.
Consequently, the sum frequency ω_{sum} of the signal and idler photon is equal to the pump frequency, i.e. constant for all adjustable frequency combinations of signal and idler photon. Thus, an OPA offers the possibility to systematically scan through different ratios $\omega_{\mathrm{sig}}/\omega_{\mathrm{idl}}$ with a constant sum frequency and is therefore well suited for the investigation of the 2PA coefficient depending on that ratio. [83]

Since for the stimulation of the 2PA the sum energy E_{sum} of the involved photons has to be at least as large as the bandgap of the respective material, two OPAs with different sum energies and accordingly different output wavelengths of the signal pulse in the visible (VIS) and in the infrared (IR) range are used. The VIS-OPA (Coherent model 9400/9450) is pumped with photons at a wavelength of 400 nm (3.10 eV), making it tunable in a wavelength range[5] of $\lambda_{\mathrm{sig}} = (510 - 800)\,\mathrm{nm}$ and $\lambda_{\mathrm{idl}} = (1855 - 800)\,\mathrm{nm}$. Here, the output pulses

[5] The degenerate photon pair at $\lambda_{\mathrm{sig}} = \lambda_{\mathrm{idl}} = 800\,\mathrm{nm}$ is directly provided by the RegA system, but is listed in the tuning range for clarity.

Table 2.1: Tuning ranges of the VIS- and IR-OPA

	VIS-OPA	**IR-OPA**
λ_{sum}	400 nm	790 nm
E_{sum}	3.10 eV	1.57 eV
λ_{sig}	$(510 - 800)$ nm	$(1210 - 1550)$ nm
E_{sig}	$(2.43 - 1.55)$ eV	$(1.02 - 0.80)$ eV
λ_{idl}	$(1855 - 800)$ nm	$(2276 - 1611)$ nm
E_{idl}	$(0.67 - 1.55)$ eV	$(0.54 - 0.77)$ eV

of the RegA system are firstly frequency-doubled to achieve the desired pump wavelength. The IR-OPA (Coherent model 9800/9850) is directly pumped with photons provided by the RegA system at a wavelength of 790 nm (1.57 eV), the corresponding tuning ranges are $\lambda_{\mathrm{sig}} = (1210 - 1550)$ nm and $\lambda_{\mathrm{idl}} = (2276 - 1611)$ nm. Hence, systematical investigations of frequency ratios $\omega_{\mathrm{sig}}/\omega_{\mathrm{idl}}$ from 1.0 to 3.6 with the VIS-OPA and from 1.1 to 1.9 with the IR-OPA are possible. An overview of the tuning ranges of the VIS- and IR-OPA can be found in Table 2.1. The lengths and energies of signal and idler pulses are strongly dependent on their frequency ratio and the individual RegA system and OPA adjustment. The pulse lengths range from $(\tau_{\mathrm{sig}}, \tau_{\mathrm{idl}}) = (50 - 500)$ fs (FWHM) with generally a decrease in τ_{sig} and an increase in τ_{idl} observed with increasing frequency ratio $\omega_{\mathrm{sig}}/\omega_{\mathrm{idl}}$. The pulse energies are $E_{\mathrm{sig}} \leq 140$ nJ and $E_{\mathrm{idl}} \leq 40$ nJ. For both OPAs, the signal and idler beams are linearly polarized at the output. The two beams are separated by different dichroic beamsplitters in case of the VIS-OPA and by a broadband Wollaston prism in case of the IR-OPA.

The complete experimental setup for the non-degenerate two-photon absorption measurements, as described in Chapter 2.1.1, is shown in Figure 2.7. The idler beam initially travels over a variable delay path x to achieve a time offset

$$\tau_{\mathrm{d}} = \frac{x n_{\mathrm{air}}}{c} \tag{2.14}$$

in between signal and idler pulse with $n_{\mathrm{air}} \approx 1$ the refractive index of air for measurements under ambient conditions. For that purpose the motorized linear stage Newport XMS50-S Ultra-Performance is used which features minimal incremental steps of 1 nm length corresponding to time intervals of a few attoseconds and hence satisfies the requirement to resolve pulses with several femtoseconds length. After the delay, the signal and idler beam are superimposed on the sample. A small angle φ between the two beams allows to easily separate them after the sample but still ensures the spatial overlap of the two

pulses in the sample since the angle is even smaller in the sample due to refraction. A $\lambda/2$-waveplate, placed in front of the sample in the idler beam, further allows the linear polarization of the idler pulse to be rotated by 90°. In this way 2PA measurements can be realized where the signal and idler pulses are either polarized parallel or perpendicular to each other. In the following, these two configurations will be referred to as co-polarized ($\parallel$) and cross-polarized ($\perp$), respectively. Furthermore, the idler beam is modulated with a mechanical chopper at a frequency f_{mod}.

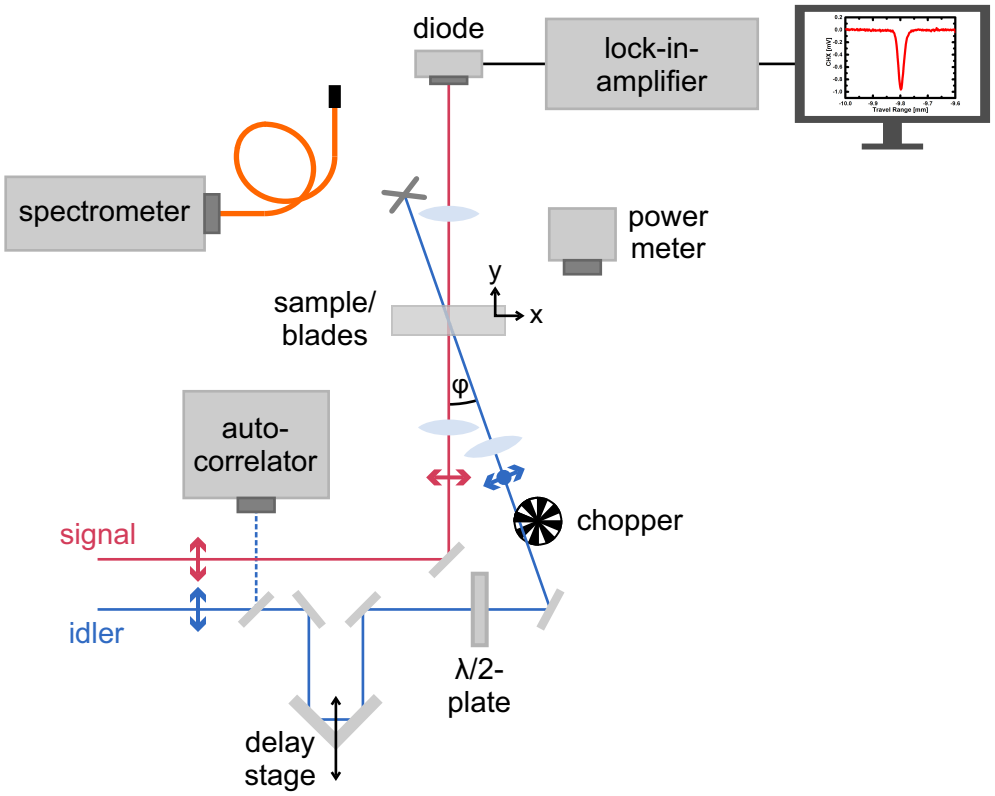

Figure 2.7: Schematic representation of the 2PA experimental setup.

In the overlap plane of the two pulses a sample holder is mounted perpendicular to the signal beam propagation direction which can be moved horizontally (x-direction) and vertically (y-direction) via two further motorized linear stages so that switching between different samples and recording knife-edge measurements is easily possible. For the knife-edge measurements a power meter can additionally be installed behind the sample holder in the signal or idler beam. The samples and the blades for the knife-edge measurements are glued side by side on a glass carrier and can be picked up by the holder (see Figure 2.8). The blades are non-transparent, titanium-vaporized glass plates with sharp edges comparable to razorblades. These are mechanically ground to the respective sample thickness, so

that the beam diameter is measured in the sample plane. Additionally, the lenses focusing the beams on the sample are chosen so that the minimum signal and idler beam waist $2w_0$ does not diverge significantly over a few tens of millimeters corresponding to the Raleigh length $z_R = \pi w_0^2/\lambda$ [79]. Also, by the choice of these lenses, the idler spot size in plane of the sample is adjusted to be bigger than the signal spot size for all frequency configurations to ensure that the signal pulse is located in area of approximately uniform idler intensity. The idler beam is blocked behind the sample and the transmission of the signal beam is detected using a photodiode. Since the idler beam is modulated, a lock-in amplifier can be used to compare the transmission signal with the reference signal from the chopper and filter out any components that do not originate from the interaction of the signal and idler beam to enhance the signal-to-noise-ratio of the measurement.

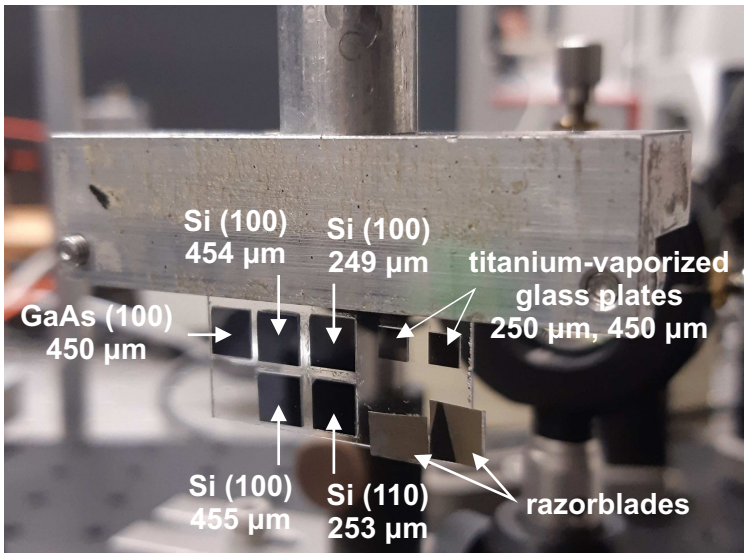

Figure 2.8: Sample holder with glass carrier on which the different Si samples are glued. The additional GaAs sample is used for adjusting the spatial and temporal overlap since Si has overall smaller 2PA strengths. The titanium-vaporized glass plates have a similar thickness as the samples and are used to perform knife-edge measurements in the sample plane. The razorblades are used to validate the quality of the titanium-vaporized glass plates. The sample holder can be electronically translated in x- and y-direction to switch between the samples and blades. The sample holder can likewise pick up glass carriers with other samples.

For the quantitative analysis of the two-photon absorption coefficient a precise knowledge of the idler pulse lengths and the signal and idler wavelengths is required. The idler pulse lengths are measured with the commercial autocorrelator APE Mini TPA, which operation principle is described in Chapter 2.1.3. The autocorrelator can be equipped with differ-

ent detector units depending on the actual wavelength of the pulse. The signal pulses could also be characterized in that way. But as the signal pulse has overall shorter pulse lengths with higher refractive indices compared to the idler pulse due to its shorter wavelengths, the length of the signal is more reliably determined by the data analysis described in Chapter 3.1.1. With that the signal pulse length is "measured" in the sample plane independent from dispersion effects of the experimental setup. For measuring the wavelengths of signal and idler pulse different commercial spectrometers are used. The visible wavelength range is covered by the AVANTES AVASPEC-2048-SPU spectrometer suitable for wavelengths $\lambda = (327 - 1100)\,\mathrm{nm}$. The near-infrared wavelength range is covered by the STELLARNET EPP-2000-NIR-INGAAS spectrometer suitable for wavelengths $\lambda = (900 - 1700)\,\mathrm{nm}$ and the APE WAVESCAN spectrometer suitable for wavelengths $\lambda = (800 - 2600)\,\mathrm{nm}$.

2.3 Sample characterization

The semiconductors studied in this thesis are ZnSe, GaAs and Si. ZnSe and GaAs belong to the group of II-VI- and III-V compound semiconductors, respectively, and exhibit Zincblende structure (space group 216, point group $\bar{4}3\mathrm{m}$). Both crystals are direct semiconductors with bandgaps of $E_{\mathrm{g,\,ZnSe}} = 2.7\,\mathrm{eV}$ and $E_{\mathrm{g,\,GaAs}} = 1.42\,\mathrm{eV}$ at room temperature. Si, on the other hand, belongs to the group of element semiconductors and has diamond structure (space group 227, point group $\mathrm{m}\bar{3}\mathrm{m}$). It is an indirect semiconductor with the smallest energy gap $E_{\mathrm{gi,\,Si}} = 1.12\,\mathrm{eV}$ close to the X-point in [100]-direction. At the Γ-point, the direct bandgap $E_{\mathrm{g,\,Si}} = 3.4\,\mathrm{eV}$ is much larger. Also, both of these bandgaps refer to room temperature. [51]

Since for the 2PA the sum energy of the involved photons needs to exceed the bandgap, the VIS-OPA ($E_{\mathrm{sum}} = 3.10\,\mathrm{eV}$) is used for the ZnSe sample and the IR-OPA ($E_{\mathrm{sum}} = 1.57\,\mathrm{eV}$) for the GaAs and Si samples. Consequently, the excess energies above the bandgaps are $\Delta E_{\mathrm{ZnSe}} \approx 400\,\mathrm{meV}$ for ZnSe, $\Delta E_{\mathrm{GaAs}} \approx 150\,\mathrm{meV}$ for GaAs and $\Delta E_{\mathrm{Si\ (indirect)}} \approx 450\,\mathrm{meV}$ for Si. Note that the sum energy of the VIS-OPA does not exceed the direct bandgap of Si, hence there is no direct bandgap transition through a 2PA process possible.
Each sample is investigated in (100) and (110) crystallographic orientation[6]. In the experiment, these planes are perpendicular to the signal beam propagation direction. The angle φ between signal and idler beam is 20°, 27° and 30° for ZnSe, GaAs and Si, respectively. Due to refraction the angle in the sample is with approximately 8°, for all three

[6] The notation (hkl) refers to a plane in the real lattice with the normal vector $\vec{n} = h\vec{a}_1 + k\vec{a}_2 + l\vec{a}_3$ and the basis vectors $\vec{a}_{\mathrm{i}}$ of the real lattice according to the Miller indices [73].

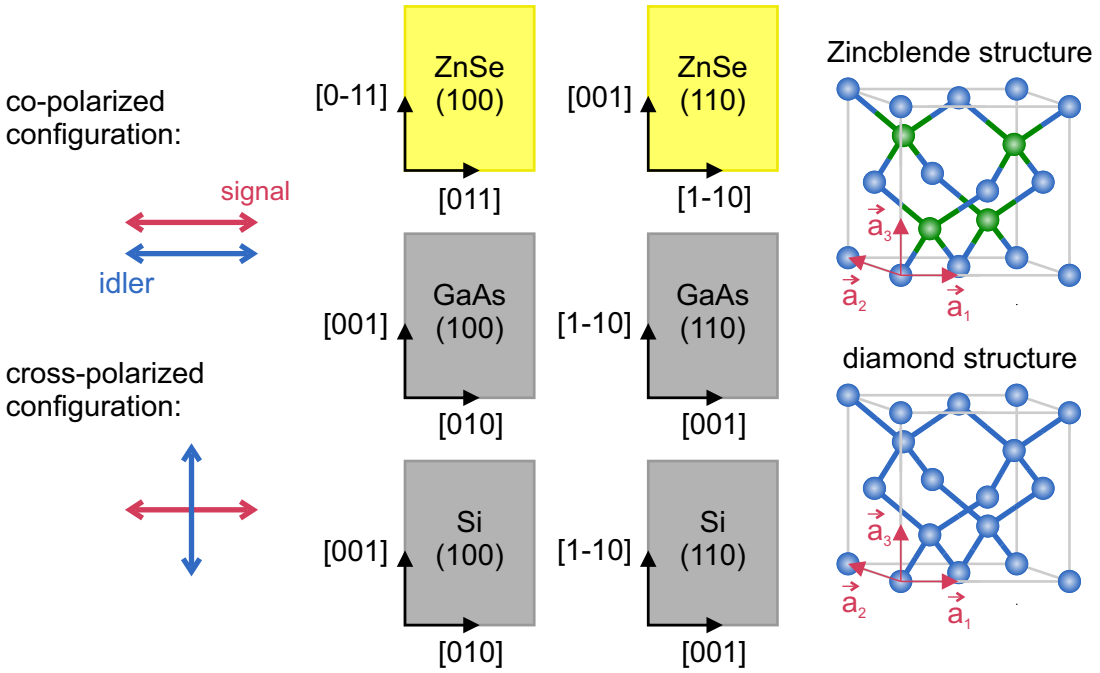

Figure 2.9: Crystallographic orientations and cutting edges of the ZnSe, GaAs and Si samples compared to the polarizations of the signal and idler beam, schematic representation of the Zincblende and diamond structure.

materials and for each idler wavelength, even smaller. Thus, the spatial walk-off in the sample is negligible and the signal and idler beams can be assumed to be parallel. The crystallographic axes with respect to the signal and idler polarizations are individual for each sample and are shown in Figure 2.9.

The ZnSe and GaAs samples have a thickness of approximately 50 µm, thick enough to ensure a sufficient signal strength but even so keeping the group velocity mismatch small. For Si the expected 2PA strengths are overall smaller than for ZnSe and GaAs, hence thicker samples for Si are chosen. Furthermore, Si is measured in two different thicknesses, approximately 250 µm and 450 µm, to exemplarily show that the sample thickness does not affect the 2PA strength, i. e. the group velocity mismatch is well described by the measurement analysis. The thicknesses are achieved by mechanical grinding of commercial wafers. All samples are undoped. An overview of the bandgaps, orientations, and exact thicknesses of all samples and the assigned laser system for each sample can be found in Table 2.2.

Table 2.2: Bandgaps at room temperature and experimental parameters of the ZnSe, GaAs and Si samples. Additionally, the laser system used for the respective sample is given.

	bandgap	orientation and thickness	laser system
ZnSe	$E_{\mathrm{g,\,ZnSe}} = 2.7\,\mathrm{eV}$	(100): $d = 42\,\mu\mathrm{m}$ (110): $d = 37\,\mu\mathrm{m}$	RegA + VIS-OPA
GaAs	$E_{\mathrm{g,\,GaAs}} = 1.42\,\mathrm{eV}$	(100): $d = 51\,\mu\mathrm{m}$ (110): $d = 52\,\mu\mathrm{m}$	RegA + IR-OPA
Si	$E_{\mathrm{gi,\,Si}} = 1.12\,\mathrm{eV}$ $E_{\mathrm{g,\,Si}} = 3.4\,\mathrm{eV}$	(100): $d = 249\,\mu\mathrm{m}$, $454\,\mu\mathrm{m}$ (110): $d = 253\,\mu\mathrm{m}$, $455\,\mu\mathrm{m}$	RegA + IR-OPA

Chapter 3

Experimental Results

In the following chapter the experimental results of the non-degenerate two-photon absorption measurements are presented. The scaling of the non-degenerate two-photon absorption coefficient as well as its orientation and polarization anisotropy for ZnSe, GaAs and Si are analyzed. The results of the specific samples are compared among each other and with previous experimental results. The accordance with theoretical predictions is evaluated.

3.1 Procedure for experimental data analysis

The analysis of the non-degenerate 2PA pump-probe traces and the knife-edge measurement data follows general procedures which can be independently applied to each individual measurement. These procedures and representative examples for all measurements are illustrated in the following.

3.1.1 Analysis of the two-photon absorption measurements

For the determination of the 2PA coefficient the theoretical approach of Negres et al. [74] is used. The authors provide an analytical model to fit the 2PA pump-probe traces (see Chapter 2.1.1) with the possibility to extract the 2PA coefficient β as a fitting parameter. The approach considers an interaction of two optical pulses centered at wavelengths λ_{sig} and λ_{idl} in a nonlinear medium whereby the signal and idler pulse refer to the weak probe and the strong pump pulse as introduced in Chapter 2.1.1, respectively[1]. The idler wavelength is chosen so that linear absorption or degenerate 2PA is suppressed and the so called undeleted pump approximation is applicable. Due to its wavelength and weak

[1]For better readability the notation used in the study of Negres et al. is adapted to the notation introduced in this thesis.

intensity also the signal pulse does not exhibit linear absorption or degenerate 2PA. The broadening of the signal pulse due to the GVD is assumed to be zero. This holds true for many materials if the introduced GVD parameter

$$\mu_{\mathrm{sig}} = \frac{\lambda_{\mathrm{sig}}^3 d}{4\pi c^2 \tau_{\mathrm{sig}}^2} \frac{\partial^2 n}{\partial \lambda^2}\bigg|_{\lambda_{\mathrm{sig}}} , \tag{3.1}$$

with the signal pulse length τ_{sig} given as HW$1/e$M, does not exceed the critical value of $\mu_{\mathrm{cr}} = 0.45$. In general, this is valid for measurements with signal pulse lengths in the 100 fs-range and in samples not thicker than a few millimeters. The broadening of the idler pulse can also be neglected since its GVD is even smaller due to its longer wavelengths[2]. Taking into account the idler parameters, Equation (3.1) can of course also be used for verification. Both pulses are assumed to have Gaussian temporal envelopes.

Within this framework the normalized nonlinear transmittance of the signal pulse can be modeled by

$$\frac{T}{T_0} = \frac{\exp(-2\sigma)}{W\sqrt{\pi}} \int_{-\infty}^{\infty} \exp\left\{ -\left(\frac{\tau + \tau_{\mathrm{d}}/\tau_{\mathrm{idl}} - \rho}{W} \right)^2 - \frac{\Gamma\sqrt{\pi}}{\rho} (\mathrm{erf}(\tau) - \mathrm{erf}(\tau - \rho)) \right\} \mathrm{d}\tau \tag{3.2}$$

with the Gaussian error function $\mathrm{erf}(x) = \frac{2}{\sqrt{\pi}} \int_0^x e^{-\tau^2} \mathrm{d}\tau$ [80], the ratio $W = \tau_{\mathrm{sig}}/\tau_{\mathrm{idl}}$ of signal and idler pulse length given as HW$1/e$M and the time delay τ_{d} between the pulses. The temporal walk-off between the two pulses when passing through the sample due to the group velocity mismatch is captured by the walk-off parameter

$$\rho = \frac{d}{\tau_{\mathrm{idl}} c} \Delta n_{\mathrm{gr}} \tag{3.3}$$

with the group index difference $\Delta n_{\mathrm{gr}} = n_{\mathrm{gr,\,sig}} - n_{\mathrm{gr,\,idl}}$ of the two pulses. The linear and nonlinear absorption of the signal pulse is covered by the linear absorption parameter

$$\sigma = \frac{\alpha d}{2} \tag{3.4}$$

and the nonlinear absorption parameter

$$\Gamma = d \frac{n_{\mathrm{sig}}}{n_{\mathrm{idl}}} I_{\mathrm{idl}}^0 \beta , \tag{3.5}$$

with the initial idler intensity I_{idl}^0 before impinging on the sample. By excluding the nonlinearity via setting $\Gamma = 0$, the model can be traced back to only linear absorption as described by the Lambert-Beer's law (1.16). The model also holds true for degenerate and

[2] This is true at least for wavelengths in the near-IR range due to the shape of $n(\lambda)$ in that wavelength region.

non-degenerate 2PA, so that β either gives $\beta_{\text{D-2PA}}$ for $\lambda_{\text{sig}} = \lambda_{\text{idl}}$ or $\beta_{\text{ND-2PA}}$ for $\lambda_{\text{sig}} \neq \lambda_{\text{idl}}$.

To obtain reliable fitting results an accurate determination of all contributing parameters to the model (3.2) is necessary. As described in the experimental setup (see Chapter 2.2) many of these values are experimentally determined. These are the wavelengths of both pulses λ_{sig} and λ_{idl}, the idler pulse width τ_{idl}, the incident idler power P_{idl} and the signal and idler spot sizes A_{sig} and A_{idl} in the sample plane[3]. Based on these parameters an average initial idler intensity

$$I_{\text{idl}}^{0} = (1 - R_{\text{idl}}) \frac{P_{\text{idl}}}{f_{\text{RegA}} \tau_{\text{idl}} A_{\text{idl}}} \tag{3.6}$$

can be derived, whereby the values for the idler reflectance R_{idl} are taken from Reference [84], which uses References [75, 85, 86] as primary sources for ZnSe, GaAs and Si. R_{idl} is dependent on the idler wavelength, on the polarization of the idler beam with respect to the incident plane (p- or s-polarized reflectance) and on the angle of incidence φ. The idler pulse length and spot size enter the calculation of I_{idl}^{0} as FW$^{1}/_{e}$M (see also Chapter 3.1.2). The remaining parameters are calculated by using literature values. The refractive index for each wavelength is given by fitting the Sellmeier equation [87]

$$n(\lambda) = \sqrt{1 + \frac{A\lambda^2}{\lambda^2 - B} + \frac{C\lambda^2}{\lambda^2 - D} + \frac{E\lambda^2}{\lambda^2 - F}} \,. \tag{3.7}$$

to literature values of the refractive index measured for a wide wavelength range. These data sets are also taken from Reference [84] with the above mentioned primary sources for the three samples. The calculated Sellmeier coefficients A – F for the specific sample can be found in Table 3.1. Using the Selllmeier equation and the relation $\omega = 2\pi \frac{c}{\lambda}$, the group refractive index can further be calculated by

$$n_{\text{gr}}(\omega) = \frac{c}{v_{\text{gr}}(\omega)} = c \frac{\mathrm{d}k(\omega)}{\mathrm{d}\omega} = \frac{\mathrm{d}}{\mathrm{d}\omega}(n(\omega)\omega) = n(\omega) + \omega \frac{\mathrm{d}n(\omega)}{\mathrm{d}\omega} \,. \tag{3.8}$$

Table 3.1: Sellmeier coefficients for ZnSe, GaAs and Si

	A	B	C	D	E	F
ZnSe	4.713	0.03741	0.13085	0.20464	0.96186	1059.53848
GaAs	9.41804	0.09315	0.44502	0.50385	1.93379	1350.49124
Si	9.64011	0.04846	4.24633	0.04903	-3.23475	-0.11019

[3]The signal spot size is monitored for comparison with the idler spot size and does not directly enter the analysis of the pump-probe traces.

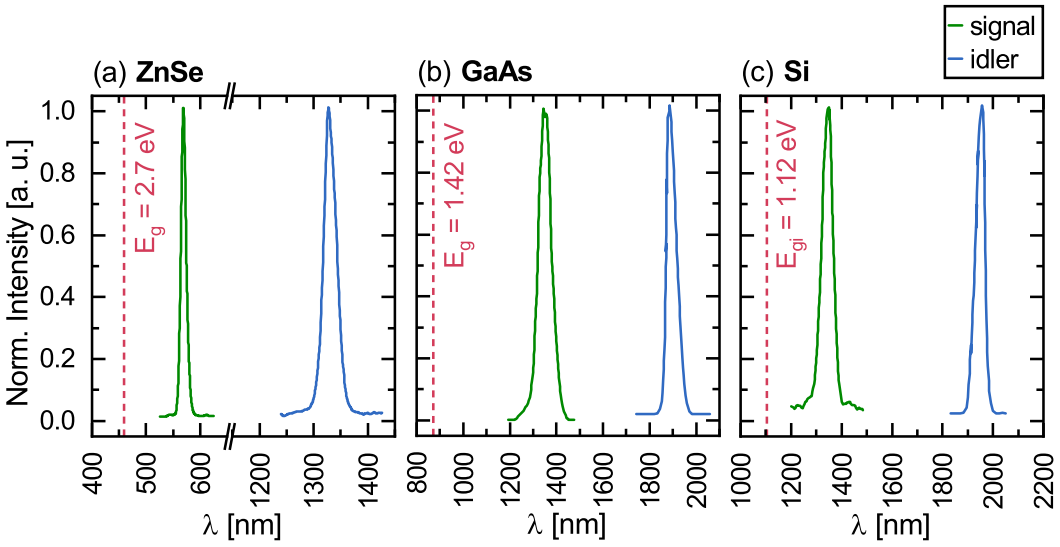

Figure 3.1: Wavelength spectra for the representative measurement examples. The pulses have central wavelengths of $\lambda_{sig} = 570\,nm$ and $\lambda_{sig} = 1341\,nm$ for the ZnSe sample and $\lambda_{sig} = 1350\,nm$ and $\lambda_{sig} = 1904\,nm$ for the GaAs and Si samples. The bandgap energies at the corresponding wavelengths are also shown for each sample.

The evaluation of the 2PA data sets is performed with WOLFRAM MATHEMATICA developed by WOLFRAM RESEARCH. The source code with detailed comments can be found in the Appendix. In the following, for each sample one representative measurement example and its analysis are illustrated. These are the co- and cross-polarized measurements at wavelength combinations $\lambda_{sig} = 570\,nm$ and $\lambda_{sig} = 1341\,nm$ for the (100)-oriented ZnSe sample and $\lambda_{sig} = 1350\,nm$ and $\lambda_{sig} = 1904\,nm$ for the (100)-oriented GaAs and Si samples. The wavelength spectra of the individual pulses are shown in Figure 3.1 with the bandgap energies of ZnSe, GaAs and Si at the corresponding wavelengths. The following assumptions are not only applicable to the given measurement examples but are also valid for all measurements at each signal and idler wavelength combination. They are consistent with the assumptions required for the evaluation of the data sets within the model of Negres et al. as given above.

The linear absorption of signal and idler photons across the fundamental bandgap $E_{g(i)}$ is assumed to be zero since $E_{sig} < E_{g(i)}$ and $E_{idl} < E_{g(i)}$. The linear absorption of signal and idler photons due to FCA can also be excluded since the pump-probe traces are symmetric and the critical intensities I_{cr} (see Equation (2.1)), calculated for signal and idler pulse, are in the order of a few hundreds of GW/cm^2 exceeding the actually used intensities

($< 1\,\mathrm{GW/cm^2}$)[4]. The degenerate 2PA of the signal pulse is suppressed due to its weak intensity. Degenerate 2PA of the idler pulse would be energetically possible for some of the shorter idler wavelengths in ZnSe and GaAs and all idler wavelengths in Si but can also be neglected because the pump-probe traces do not show transient absorption beyond the temporal overlap of signal and idler pulse. The temporal broadening of the signal and idler pulses while propagating through the sample due to GVD is negligible as for all samples the GVD parameter (3.1) for signal and idler pulse does not exceed the critical GVD parameter of $\mu_{\mathrm{cr}} = 0.45$. The spot sizes of signal and idler pulse are adjusted so that the idler spot is at least 2.5-times for ZnSe, 4.4-times for GaAs, 2.5-times for Si with $d = 249\,\mu\mathrm{m}$ and 2.6-times for Si with $d = 454\,\mu\mathrm{m}$ larger than the signal spot. As a result, the intensity of the idler across the signal spot is practically identical to its peak intensity. Therefore the average idler intensity I^0_{idl} in Equation (3.6) is scaled with $e/(e-1) \approx 1.582$ to convert the assumed flat-top to a Gaussian intensity profile with the peak intensity $I^{\mathrm{peak}}_{\mathrm{idl}}$.

Table 3.2: Signal and idler pulse parameters

	ZnSe	**GaAs**	**Si** 249 µm	**Si** 454 µm
λ_{sig} [nm]	570	1350	1350	1350
λ_{idl} [nm]	1341	1904	1904	1904
τ_{idl} [fs]	59.0	61.9	96.1	96.1
μ_{sig}	0.004	0.003	0.057	0.104
μ_{idl}	0.003	0.007	0.011	0.020
P_{sig} [mW]	0.2	0.1	0.1	0.1
P_{idl} [mW]	0.45	0.7	0.6	0.6
A_{sig} [µm^2]	2100	1000	1500	3200
A_{idl} [µm^2]	30100	17300	12000	13900
$I^{\mathrm{peak}}_{\mathrm{idl},\parallel}$ [GW/cm^2]	0.067	0.155	0.122	0.106
$I^{\mathrm{peak}}_{\mathrm{idl},\perp}$ [GW/cm^2]	0.064	0.138	0.105	0.092

Note: τ_{idl} is given as HW^1/$_e$M while A_{sig} and A_{idl} are given as FW^1/$_e$M

A detailed overview of the signal and idler pulse parameters, the calculated non-degenerate 2PA coefficients $\beta_{\parallel}$ and $\beta_{\perp}$ and the related signal pulse widths τ_{sig} can be found in Ta-

[4]Strictly speaking, the estimation via I_{cr} is only valid for FCA whereby the carriers are originally excited by degenerate 2PA. The critical intensity for FCA arising from carriers excited by non-degenerate 2PA will however be in the same order, since signal and idler pulse have on that note comparable energies, pulse lengths and reflectivities.

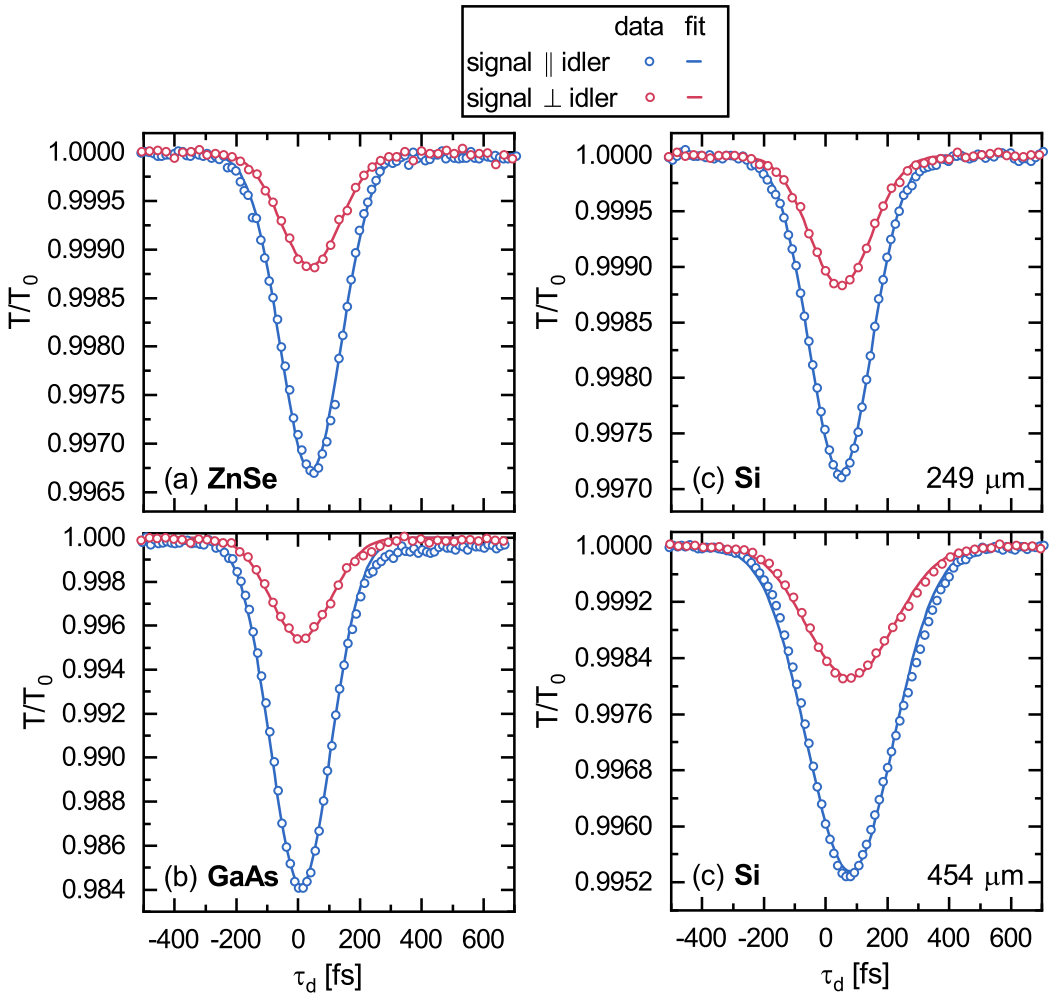

Figure 3.2: Exemplary pump-probe traces for a co- and cross-polarized non-degenerate 2PA measurement for the (a) ZnSe sample at $\lambda_{\mathrm{sig}} = 570\,\mathrm{nm}$ and $\lambda_{\mathrm{idl}} = 1341\,\mathrm{nm}$ and (b) GaAs sample, (c) Si sample with $d = 249\,\mu\mathrm{m}$, (d) Si sample with $d = 454\,\mu\mathrm{m}$ all at $\lambda_{\mathrm{sig}} = 1350\,\mathrm{nm}$ and $\lambda_{\mathrm{idl}} = 1904\,\mathrm{nm}$. All samples exhibit (100) crystallographic orientation. The blue (red) data corresponds to the co-(cross-)polarized configuration. Solid lines represent a fit according to the model by Negres et al. [74].

Table 3.3: Fitting results

	$\beta_{\parallel}$ [cm/GW]	$\tau_{\mathrm{sig},\parallel}$ [fs]	$\beta_{\perp}$ [cm/GW]	$\tau_{\mathrm{sig},\perp}$ [fs]
ZnSe	$12.93\,^{+1.59}_{-1.36}$	120.7 ± 0.9	$4.77\,^{+0.60}_{-0.51}$	120.1 ± 1.7
GaAs	$22.25\,^{+1.85}_{-1.66}$	122.5 ± 1.4	$7.19\,^{+0.61}_{-0.55}$	123.5 ± 1.9
Si (249 µm)	$0.69\,^{+0.06}_{-0.05}$	96.7 ± 0.8	$0.34\,^{+0.03}_{-0.03}$	98.2 ± 1.3
Si (454 µm)	$0.98\,^{+0.07}_{-0.07}$	153.2 ± 1.7	$0.46\,^{+0.04}_{-0.03}$	156.6 ± 1.8

Note: $\tau_{\mathrm{sig},\parallel}$ and $\tau_{\mathrm{sig},\perp}$ are given as HW$^1/_e$M

bles 3.2 and 3.3. Figure 3.2 shows the measurement data and the corresponding fits. To estimate the error $\pm\Delta\beta$ of the 2PA coefficient, the most error-prone parameters are varied within the following inaccuracies. For the signal pulse length and the idler spot size these are the wavelength dependent fitting errors $\Delta\tau_{\mathrm{sig}}$ and ΔA_{idl}. The idler pulse length, the sample thickness and the incident idler power exhibit systematic errors independently applicable to all measurements and samples. These are $\Delta\tau_{\mathrm{idl}} = \pm 3\,\mathrm{fs}$, $\Delta d = \pm 1\,\mu\mathrm{m}$ and $P_{\mathrm{idl}} = \pm 0.03\,\mathrm{mW}$. By including the error-prone parameters in the analysis and running once again the fitting procedure, $+\Delta\beta$ and $-\Delta\beta$ are individually determined.

For all samples the measurement data is in excellent agreement with the fits. All non-degenerate pump-probe traces show the characteristic shift of the transmittance minimum to delay times $\tau_{\mathrm{d}} > 0$ due to the group velocity mismatch between signal and idler pulse. This also leads to the broadening of the pump-probe traces of the thicker Si sample in comparison with the thinner sample. The formation of a plateau at the minimum amplitude cannot be observed here since the sample is not sufficiently thick in this respect. There is no significant degenerate 2PA by the idler beam or free-carrier absorption of probe photons because the pump-probe traces all exhibit a symmetrical shape so that the assumptions made before can be confirmed.

3.1.2 Analysis of the knife-edge measurements

The knife-edge measurements were repeated for each sample at every individual wavelength combination as the signal and idler spot sizes vary with the wavelength tuning of the VIS- and IR-OPA. The idler spot size directly enters the 2PA coefficient calculation (see Section 3.1.1) as a parameter of the idler power intensity. The signal spot size is monitored for comparison with the idler spot size. The individual measurement data sets are in principle the same so that their analysis follows the same procedure analogously. For that

reason only one data set is exemplarily described in the following. For the data analysis the software program ORGIN, which is developed by the ORGINLAB CORPORATION, is used.

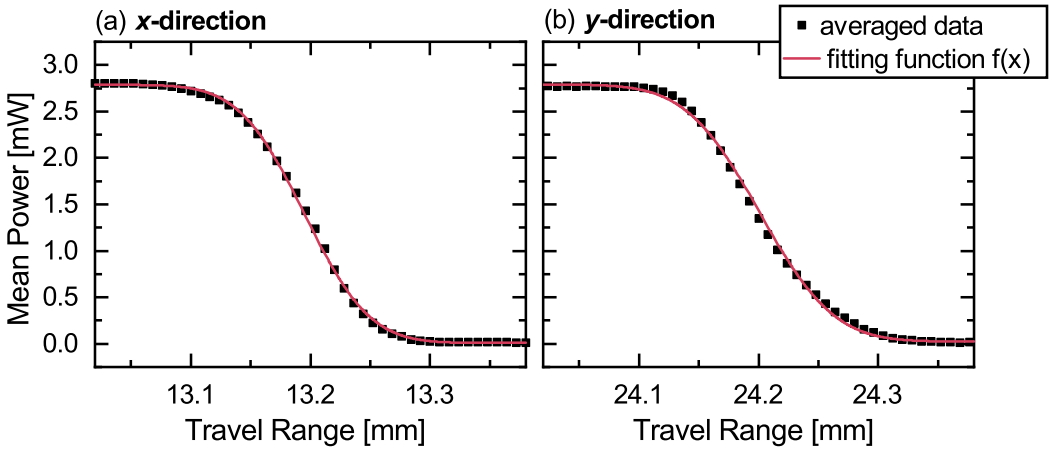

Figure 3.3: Exemplary knife-edge measurement for the idler beam at 1736 nm in the measurement series of the GaAs sample for the (a) x- and (b) y-direction. The data reveals beam diameters of $d_x = 137.4\,\mu\text{m}$ and $d_y = 121.6\,\mu\text{m}$.

From Equation 2.4, which describes the power profile of the knife-edge measurement, a fitting function $f(x)$ can be derived. $f(x)$ is equipped with the offsets x_0 and y_0 in x- and y-direction, respectively, since the power profile in the experiment could not be symmetric around the origin. With $|B| = P_{\text{max}}$ the fitting function dependent on the travel range x of the blade is given by

$$f(x) = y_0 + \frac{B}{2}\,\text{erf}\left(\frac{2(x - x_0)}{d}\right) , \tag{3.9}$$

where B can be positive or negative depending on whether the beam is covered by the blade at the beginning of the measurement or not. The fitting parameter d gives the spot diameter at which the maximum power has decreased to P_{max}/e (FW1/eM). Figure 3.3 shows an example of a knife-edge measurement. The measurement was taken for the idler beam at a wavelength of $\lambda = 1736\,\text{nm}$ in the measurement series of the GaAs sample. The blade was moved three times in total over the complete beam diameter in 4 µm steps. The following results

$$B = (-2.766 \pm 0.013)\,\text{mW}, \quad x_0 = (24.2012 \pm 0.0010)\,\mu\text{m},$$
$$y_0 = (1.407 \pm 0.008)\,\text{mW} \quad \text{and} \quad d_x = (137.4 \pm 2.1)\,\mu\text{m}$$

are obtained from fitting the averaged measurement points for the x-direction. The beam

was also measured in y-direction to calculate the spot size $A = \frac{\pi}{4} d_x d_y$ as an ellipse to achieve a higher accuracy. For the given exemplarily measurement, the results for the y-direction are

$$B = (-2.778 \pm 0.007)\,\mathrm{mW}, \quad x_0 = (13.1949 \pm 0.0004)\,\mu\mathrm{m},$$
$$y_0 = (1.398 \pm 0.004)\,\mathrm{mW} \quad \text{and} \quad d_y = (121.6 \pm 1.3)\,\mu\mathrm{m},$$

so that the beam has a spot size of $A_{\mathrm{idl}} = (13100 \pm 200)\,\mu\mathrm{m}^2$. The error is calculated by $\Delta A = \frac{\pi}{4}\sqrt{(d_y \Delta d_x)^2 + (d_x \Delta d_y)^2}$ according to the Gaussian error propagation [88]. The fits are in accurate accordance with the measurement data.

3.2 Evaluation of the two-photon absorption coefficients

In the following, the calculated 2PA coefficients are plotted as a function of the frequency ratio $\omega_{\mathrm{sig}}/\omega_{\mathrm{idl}}$ for the co- and cross-polarized measurements as well as for the different samples to analyze the scaling behavior of the 2PA strength. Additionally, the orientation and polarization anisotropy and its dependence on the frequency ratio $\omega_{\mathrm{sig}}/\omega_{\mathrm{idl}}$ is evaluated.

In Figure 3.4 the extracted 2PA coefficients $\beta_{\parallel}$ and $\beta_{\perp}$ for both the (100)- and (110)-oriented ZnSe samples are summarized. Some data points at certain frequency ratios appear twice as part of the measurements are repeated at a later stage as test for consistency. For both crystallographic orientations of the ZnSe samples the values for the co- and cross-polarized 2PA coefficient $\beta_{\parallel}$ and $\beta_{\perp}$ increase with increasing frequency ratio $\omega_{\mathrm{sig}}/\omega_{\mathrm{idl}}$, whereby the values of $\beta_{\perp}$ are overall smaller than the values for $\beta_{\parallel}$. In case of the (100)-oriented sample $\beta_{\parallel}$ and $\beta_{\perp}$ show an approximately eightfold increase comparing configurations with $\omega_{\mathrm{sig}}/\omega_{\mathrm{idl}} = 1$ and $\omega_{\mathrm{sig}}/\omega_{\mathrm{idl}} = 3.3$[5]. The 2PA coefficient in the (110)-oriented sample increases slightly stronger with a factor of ≈ 10 for the co-polarized and ≈ 13 for the cross-polarized configuration. Comparing the two crystallographic orientations, similar magnitudes for $\beta_{\parallel}$ are found at the same frequency ratios. In contrast, the values for $\beta_{\perp}$ for the (110)-oriented sample are consistently higher than for the (100)-oriented sample.

The scattering of the data occurs due to various reasons. The two most relevant ones are (i) the unstable signal and idler intensities for different frequency ratios $\omega_{\mathrm{sig}}/\omega_{\mathrm{idl}}$ mainly due to varying pulse lengths and spot sizes as a consequence of tuning the OPA to different

[5] The 2PA coefficient at $\omega_{\mathrm{sig}}/\omega_{\mathrm{idl}} = 3.6$ is not used for the estimation of the increase as it shows higher deviations than the other measurements points.

wavelengths and (ii) the challenging adjustment of spatial and temporal overlap of signal and idler pulse. Especially the increasing noise of the VIS- and IR-OPA for widely non-degenerate configurations diminish the exact positioning of mirrors and delay stage at the maximum 2PA signal strength so that the scatter of the experimental data also increases with higher degrees of non-degeneracy.

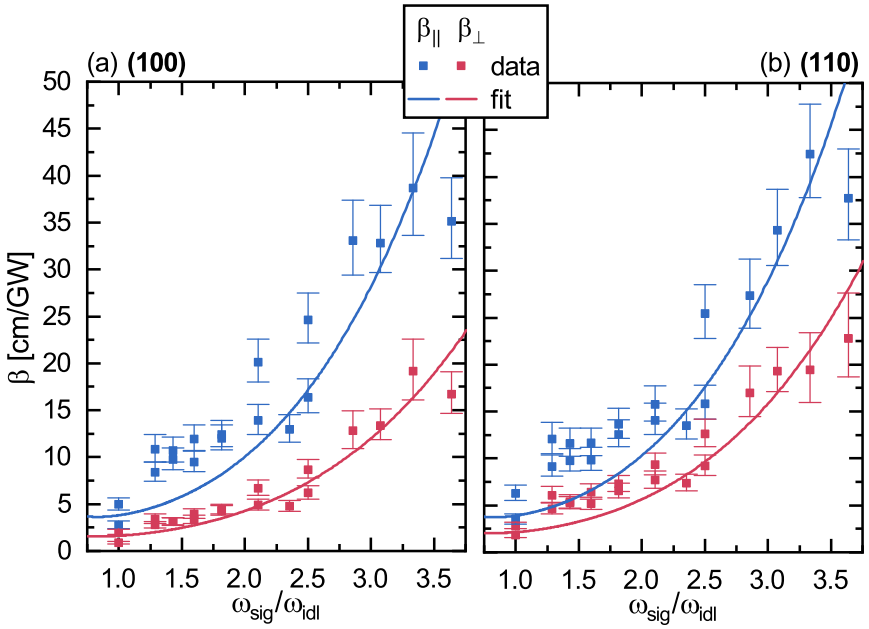

Figure 3.4: ZnSe 2PA coefficients β for co- (blue) and cross-polarized (red) measurements as a function of the frequency ratio $\omega_{sig}/\omega_{idl}$ for (a) (100) and (b) (110) crystallographic orientation. The solid lines represent the corresponding fits according to the model by Hannes et al. [47].

In comparison with literature the average values[6] for the degenerate 2PA coefficient at $\lambda_{sig} = \lambda_{idl} = 800\,\text{nm}$, $\bar{\beta}_{\parallel} = 3.9\,\text{cm/GW}$ for the (100)-oriented sample and $\bar{\beta}_{\parallel} = 4.9\,\text{cm/GW}$ for the (110)-oriented sample are in good accordance with previous studies. Mihaela Balu et al. [59] and Fishman et al. [19] independently report a co-polarized 2PA coefficient of $\approx 3.5\,\text{cm/GW}$ for excitation with 800 nm pulses. Balu et al. used a polycrystalline ZnSe specimen and Fishman et al. do not give particular specifications of the crystal and polarization orientation at all. The 2PA anisotropy may account for the slightly lower literature values of the 2PA coefficients. Studies giving more detailed specifications are not available for ZnSe. Diverging results for the 2PA coefficient despite same experimental conditions

[6] The given values for $\bar{\beta}$ are the average degenerate 2PA coefficients out of two independent measurements at $\lambda_{sig} = \lambda_{idl} = 800\,\text{nm}$.

may also stem from different quantity definitions used in the analysis. For example, it has an influence on the overall magnitude of β whether the idler pulse length τ_{idl} is included in the intensity I^0_{idl} (see Equation (3.6)) as FWHM, FW$1/e$M or FW$1/e^2$M, since the model to fit the pump-probe traces directly comprises I^0_{idl} (see Equation (3.2))[7]. This also applies to the signal spot size A_{idl} since the spot size diameters can likewise be defined differently. In addition, the choice of a specific data set among others used for the determination of, for example, the (group) refractive indices and reflectivities may also account for differences between experimental studies despite same experimental conditions. The comparison of non-degenerate 2PA coefficients is even more difficult since studies need to be found that examine the 2PA coefficient at the same frequency ratio and sum energy. In case of ZnSe there is no comparable non-degenerate data available.

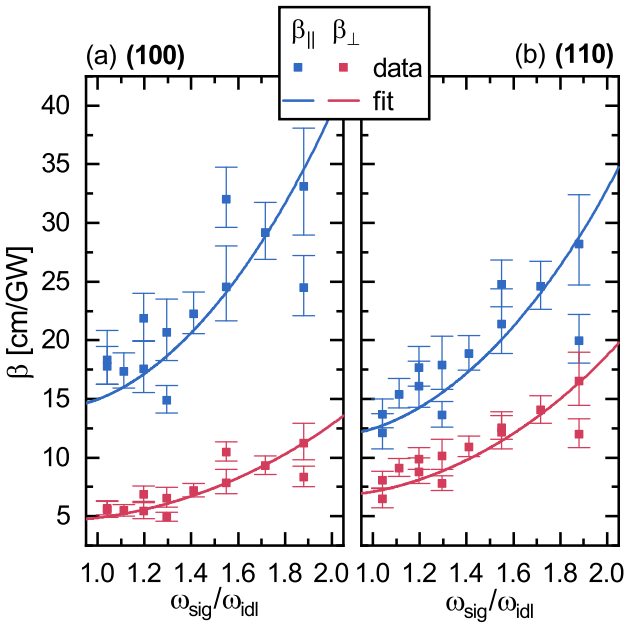

Figure 3.5: GaAs 2PA coefficients β for co- (blue) and cross-polarized (red) measurements as a function of the frequency ratio $\omega_{\mathrm{sig}}/\omega_{\mathrm{idl}}$ for (a) (100) and (b) (110) crystallographic orientation. The solid lines represent the corresponding fits according to the model by Hannes et al. [47].

In Figure 3.5 the extracted 2PA coefficients $\beta_{\parallel}$ and $\beta_{\perp}$ for the (100)- and (110)-oriented GaAs samples are summarized. Also for GaAs some data points at certain frequency ratios appear twice as part of the measurements are repeated. Similar to ZnSe, for both crystallo-

[7] This is also valid for the analysis of z-scan measurements where the model to fit the z-scan traces also comprises I_0 [14, 30].

graphic orientations of the GaAs samples the values for the co- and cross-polarized 2PA coefficients $\beta_{\parallel}$ and $\beta_{\perp}$ increase with increasing frequency ratio $\omega_{\mathrm{sig}}/\omega_{\mathrm{idl}}$. Also, the values of $\beta_{\perp}$ are overall smaller than the values for $\beta_{\parallel}$. For GaAs an approximately twofold increase over the whole measurement range from $\omega_{\mathrm{sig}}/\omega_{\mathrm{idl}} = 1.04$ to $\omega_{\mathrm{sig}}/\omega_{\mathrm{idl}} = 1.88$ can be observed for both polarization configurations and crystallographic orientations. When comparing the two crystallographic orientations the values of $\beta_{\parallel}$ are generally higher for the (100)-oriented than for the (110)-oriented sample, for $\beta_{\perp}$ it is reversed. In comparison with ZnSe, GaAs reveals overall higher 2PA coefficients $\beta_{\parallel}$ and $\beta_{\perp}$ for the same frequency ratios. This is consistent with the general E_{g}^{-3}-scaling of the degenerate and non-degenerate 2PA coefficient in direct semiconductors by which smaller bandgap semiconductors ($E_{\mathrm{g,\,GaAs}} < E_{\mathrm{g,\,ZnSe}}$) generally exhibit higher 2PA strengths (see Chapter 1.2.2.1).

Also for GaAs a comparison with previous experimental data is only possible for co-polarized degenerate 2PA coefficients as no data is available for non-degenerate configurations at similar frequency ratios and sum energies. Since the IR-OPA cannot provide degenerate photon pairs, the data points closest to degeneracy at $\omega_{\mathrm{sig}}/\omega_{\mathrm{idl}} = 1.04$ ($\lambda_{\mathrm{sig}} = 1550\,\mathrm{nm}$, $\lambda_{\mathrm{idl}} = 1611\,\mathrm{nm} \Rightarrow \bar{\lambda} = 1580\,\mathrm{nm}$) are used for comparison. The corresponding average 2PA coefficients are $\bar{\beta}_{\parallel} = 18.1\,\mathrm{cm/GW}$ for the (100)-oriented sample and $\bar{\beta}_{\parallel} = 12.9\,\mathrm{cm/GW}$ for the (110)-oriented sample. Fishman et al. [19] report a degenerate co-polarized 2PA coefficient of $\approx 2.5\,\mathrm{cm/GW}$ and Cirloganu et al. [18] of $\approx 12.0\,\mathrm{cm/GW}$ both at $\lambda_{\mathrm{sig}} = \lambda_{\mathrm{idl}} = 1580\,\mathrm{nm}$ whereby no further crystal or polarization specifications are given. In case of GaAs, few studies have been published which further specify the crystallographic orientation and beam polarization. Dvorak et al. [26] performed a study using a (001)-oriented GaAs sample with signal and idler beam polarization parallel to the [100]-direction and extracted a 2PA coefficient of $\approx 20.0\,\mathrm{cm/GW}$ at $\lambda_{\mathrm{sig}} = \lambda_{\mathrm{idl}} = 950\,\mathrm{nm}$. DeSalvo et al. [27] report differences in the degenerate 2PA coefficients at $\lambda_{\mathrm{sig}} = \lambda_{\mathrm{idl}} = 1064\,\mathrm{nm}$ for (100)-, (110)- and (111)-oriented GaAs specimens with the beam polarization parallel to the [001]-direction, varying between 18 cm/GW and 25 cm/GW. Taking into account the deviating experimental conditions and possible differences in the analysis, as explained above for ZnSe, the measurement results agree well with the reported literature values.

Further on, the experimental results of ZnSe and GaAs are in good accordance with the theoretically predicted scaling functions $\beta_{\text{ND-2PA}}(\omega_1, \omega_2)$ for direct semiconductors introduced in Chapter 1.2.2.1. In Figures 3.4 and 3.5 the solid lines represent fits to the co- and cross-polarized measurement data according to the scaling function of Hannes et al. [47] (see Equation (1.31)). A prefactor A has been chosen for best fit with the experimental

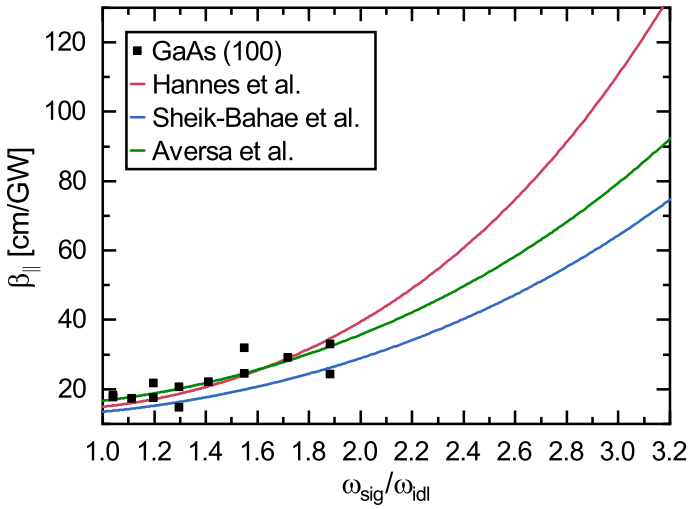

Figure 3.6: Comparison of the theoretical scaling functions of Hannes et al. [47] (red), Sheik-Bahae et al. [16] (blue) and Aversa et al. [46] (green). The solid lines represent the fits to the co-polarized 2PA coefficients $\beta_{\parallel}$ in the (100)-oriented GaAs sample. In each case, a prefactor has been chosen for best fit with the experimental data. The difference in between those models is particularly seen for very high degrees of non-degeneracy beyond the accessible measurement range.

data so that the fitting function is given by

$$\beta_{\text{ND-2PA}}(E_{\text{sig}}) = A \cdot E_{\text{sig}} \left(\frac{1}{E_{\text{sig}}^2} + \frac{1}{(E_{\text{sum}} - E_{\text{sig}})^2} \right)^2 . \tag{3.10}$$

Regardless of the specific polarization configuration and sample orientation, the measurement data for ZnSe and GaAs agrees very well with the theoretical scaling. The scaling functions of Sheik-Bahae et al. [16] (see Equation (1.32)) and Aversa et al. [46] (see Equation (1.33)) are also consistent with the experimental results. These fits deviate only little from the fit according to Hannes et al. in the measurement range. To further distinguish between those models, measurement points at higher degrees of non-degeneracy would be required which are inaccessible with the VIS- and IR-OPA described in Chapter 2.2. An exemplary comparison of the fits according to the three different theoretical scalings is shown in Figure 3.6 for the experimental data of the (100)-oriented GaAs sample and co-polarized configuration, representative for all measurements in ZnSe and GaAs. Also for the scaling functions of Sheik-Bahae et al. and Aversa et al., a prefactor A has been chosen for best fit with the experimental data. The fitting functions are given by

$$\beta_{\text{ND-2PA}}(E_{\text{sig}}) = A \cdot \frac{E_{\text{sum}}^a}{E_{\text{sig}}^3 (E_{\text{sum}} - E_{\text{sig}})^4} \tag{3.11}$$

whereby the exponent of the numerator is $a = 2, 3$ for the scaling function of Sheik-Bahae et al. and Aversa et al., respectively.

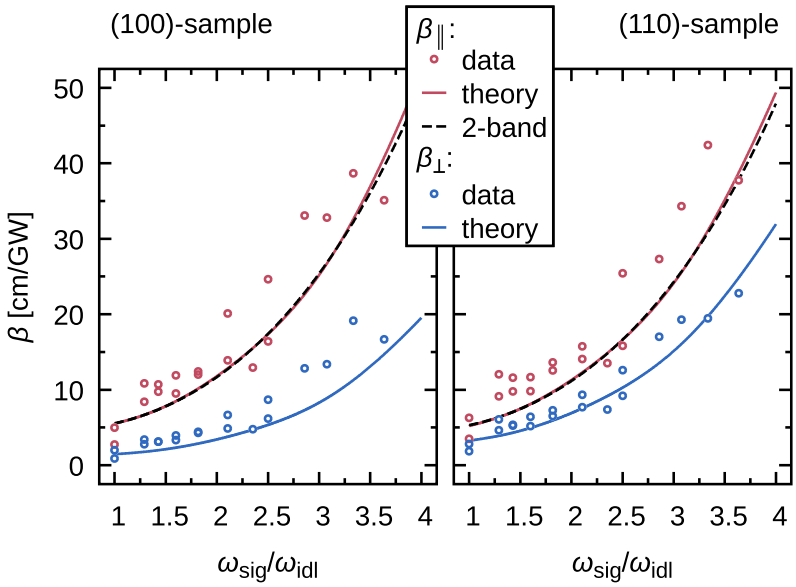

Figure 3.7: ZnSe 2PA coefficients β for co- (red) and cross-polarized (blue) measurements as a function of the frequency ratio $\omega_{sig}/\omega_{idl}$ for (100) (left) and (110) (right) crystallographic orientation as in Figure 3.4. The solid lines represent tailored numerical calculations done by W.-R. Hannes (Paderborn University) within the multiband model of Hannes et al. [89]. The dashed lines correspond to the two-band model of Hannes et al. [47] but with **k**-dependent dipole matrix elements (for further details see Reference [89]). Taken from Reference [89].

The two-band models of Hannes et al., Sheik-Bahae et al. and Aversa et al. do not capture the anisotropy of the 2PA coefficient and are restricted to evaluate the scaling behavior (and the magnitude in case of $\beta_\parallel$) so that only by using a prefactor in the fitting functions the scaling can be adjusted to the different polarization configurations and sample orientations. For a theoretical description of the 2PA coefficient taking anisotropy into account, calculations which incorporate higher conduction bands are required since these mainly influence the 2PA anisotropy as described in Chapter 1.2.2.3. Therefore, Hannes et al. have proposed a more comprehensive model including higher conduction bands based on multiband semiconductor Bloch equations [89]. To the experimental data of ZnSe tailored numerical calculations done by W.-R. Hannes (Paderborn University) within this model show surprisingly good agreement without using any fitting parameter (see Figure 3.7). The theory well reproduces the magnitude and scaling behavior of $\beta(\omega_{sig}/\omega_{idl})$ as well as the orientation and polarization anisotropy of the 2PA coefficient. In comparison with the

two-band model fit in Figure 3.4 the 2PA strength shows a slightly weaker increase with increasing frequency ratio $\omega_{\mathrm{sig}}/\omega_{\mathrm{idl}}$ so that the slope of the fit more closely approaches the slopes of the fits according to the models of Sheik-Bahae et al. and Aversa et al. as depicted in Figure 3.6.

Figure 3.8 summarizes the experimental results for the $\approx 250\,\mu\mathrm{m}$ and $\approx 450\,\mu\mathrm{m}$ thick Si samples for both $\beta_{\parallel}$ and $\beta_{\perp}$, again comparing the (100) and (110) crystallographic orientations. The 2PA coefficients increase with higher degrees of non-degeneracy as in case of ZnSe and GaAs. The values of $\beta_{\perp}$ are also overall smaller than the values for $\beta_{\parallel}$. As expected, the overall absorption strength in comparison with ZnSe and GaAs is smaller due to the additionally participating phonon in indirect semiconductors. In the measurement range of $\omega_{\mathrm{sig}}/\omega_{\mathrm{idl}} = 1.04-1.86$ the 2PA coefficients show an approximately twofold increase independent of the sample thickness, polarization configuration and crystallographic orientation. Comparing the 2PA coefficients of one crystallographic orientation at the same frequency ratio between the thin and thick Si sample, the values are, as expected, rather similar since the sample thickness should not affect the 2PA coefficient. Only the measurement points at $\omega_{\mathrm{sig}}/\omega_{\mathrm{idl}} = 1.1$ and $\omega_{\mathrm{sig}}/\omega_{\mathrm{idl}} = 1.2$ of the (110)-oriented thinner Si sample show higher deviations. These are most likely due to exceptional measurement inaccuracies since such high deviations only occur for these two points and are mostly absent in the other samples. In general, the $\beta_{\parallel}$ values of the (100)-oriented sample are smaller than for the (110) crystallographic orientation, for $\beta_{\perp}$ the values are largely independent of the orientation. The generally larger scatter of the Si data, in contrast to the ZnSe and GaAs data, is due to the overall smaller 2PA signal strengths. Here, the scatter of the experimental data also increases with higher degrees of non-degeneracy, again, because the noise of the VIS-OPA increases for widely non-degenerate configurations.

The experimentally obtained 2PA coefficients, $\bar{\beta}_{\parallel} = 0.9\,\mathrm{cm/GW}$ for the (100)-oriented sample and $\bar{\beta}_{\parallel} = 1.1\,\mathrm{cm/GW}$ for the (110)-oriented sample[8], closest to degeneracy ($\lambda_{\mathrm{sig}} = 1550\,\mathrm{nm}$, $\lambda_{\mathrm{idl}} = 1611\,\mathrm{nm} \Rightarrow \bar{\lambda} = 1580\,\mathrm{nm}$) are in good agreement with previous experimental studies. Bristow et al. [66] report a degenerate 2PA coefficient of $\approx 0.75\,\mathrm{cm/GW}$ at $\lambda_{\mathrm{sig}} = \lambda_{\mathrm{idl}} \approx 1600\,\mathrm{nm}$ for a (001)-oriented sample and Mihaela Dinu et al. [30] $\approx 0.79\,\mathrm{cm/GW}$ at $\lambda_{\mathrm{sig}} = \lambda_{\mathrm{idl}} \approx 1540\,\mathrm{nm}$ for a (110)-oriented sample. In both cases, the relative orientation of the crystallographic axes with respect to the beam polarization is not specified. Lin et al. [67] report a degenerate 2PA coefficient of $\approx 0.5\,\mathrm{cm/GW}$

[8] In the following comparison with literature $\bar{\beta}$ is given as the average 2PA coefficient obtained from the thin and thick Si sample.

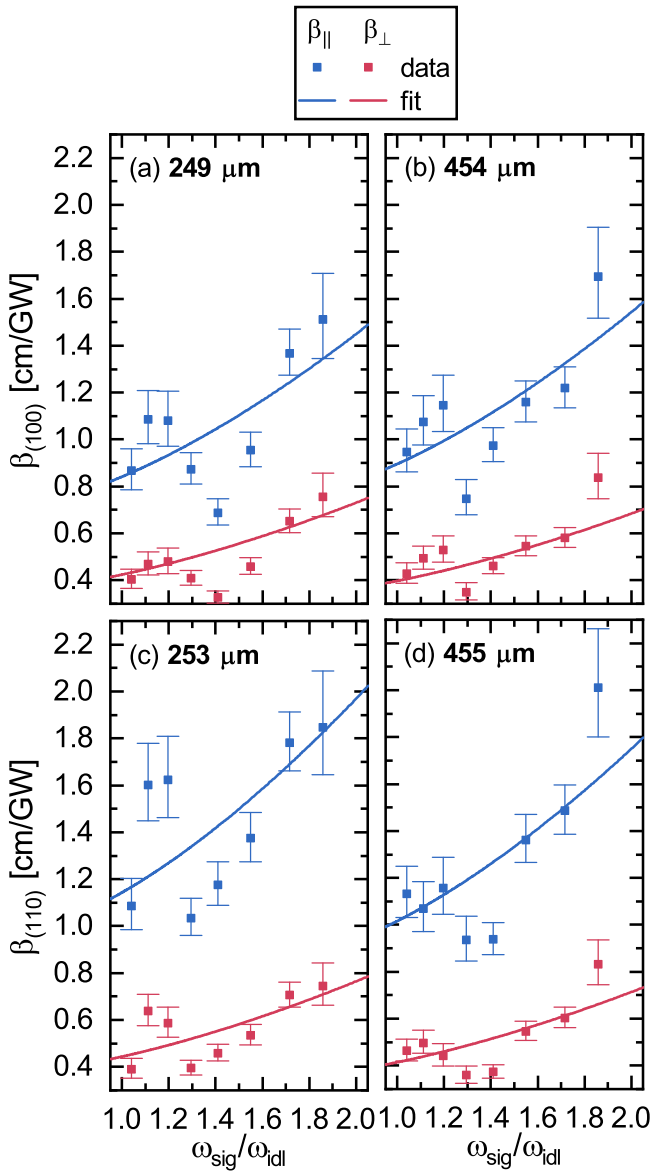

Figure 3.8: Si 2PA coefficients β for co- (blue) and cross-polarized (red) measurements as a function of the frequency ratio $\omega_{sig}/\omega_{idl}$ for (a), (b) (100) and (c), (d) (110) crystallographic orientation. Note the different sample thicknesses as indicated. The solid lines represent the corresponding fits according to the model by Faryadras et al. [23].

at $\lambda_{\mathrm{sig}} = \lambda_{\mathrm{idl}} \approx 1600\,\mathrm{nm}$ for a (100)-oriented Si sample with signal and idler polarization parallel to the [010]-direction. All these studies focus on co-polarized configurations. For Si also a comparison with non-degenerate data is possible. Faryadras et al. [23] report non-degenerate 2PA coefficients of $\approx 0.7\,\mathrm{cm/GW}$ and $\approx 1.0\,\mathrm{cm/GW}$ for wavelength configurations of $\lambda_{\mathrm{sig}} = 1450\,\mathrm{nm}$, $\lambda_{\mathrm{idl}} = 1700\,\mathrm{nm}$ and $\lambda_{\mathrm{sig}} = 1350\,\mathrm{nm}$, $\lambda_{\mathrm{idl}} = 1900\,\mathrm{nm}$, respectively. Taking into account the measurement inaccuracies a good agreement can be found with $\bar{\beta}_{\parallel} = 1.1\,\mathrm{cm/GW}$ at $\omega_{\mathrm{sig}}/\omega_{\mathrm{idl}} = 1.20$ ($\lambda_{\mathrm{sig}} = 1450\,\mathrm{nm}$, $\lambda_{\mathrm{idl}} = 1736\,\mathrm{nm}$) and $\bar{\beta}_{\parallel} = 0.8\,\mathrm{cm/GW}$ at $\omega_{\mathrm{sig}}/\omega_{\mathrm{idl}} = 1.41$ ($\lambda_{\mathrm{sig}} = 1350\,\mathrm{nm}$, $\lambda_{\mathrm{idl}} = 1904\,\mathrm{nm}$) of the (100)-oriented sample. Faryadras et al. also used pulses in the femtosecond-range and investigated a (100)-oriented sample in a co-polarized configuration whereby the relative orientation of the beam polarization with respect to the crystallographic directions is no further given.

The experimental results of Si are in good accordance with the theoretically predicted scaling function $\beta_{\text{ND-2PA}}(\omega_1, \omega_2)$ of Faryadras et al. [23] for indirect semiconductors (see Equation (1.36)) as introduced in Chapter 1.2.2.2. The solid lines in Figure 3.8 represent those fits for each sample and each polarization configuration. Again, a prefactor A has been chosen for best fit with the experimental data so that the fitting function is given by

$$\beta_{\text{ND-2PA}}(E_{\mathrm{sig}}) = A \cdot \frac{E_{\mathrm{gi}}^3}{E_{\mathrm{sig}}(E_{\mathrm{sum}} - E_{\mathrm{sig}})^3} \left(\frac{E_{\mathrm{gi}}}{E_{\mathrm{g}} - E_{\mathrm{sig}}} + \frac{E_{\mathrm{gi}}}{E_{\mathrm{g}} - E_{\mathrm{sum}} + E_{\mathrm{sig}}} \right)^2 . \tag{3.12}$$

Comparing the fits of the two different sample thicknesses reveals similar prefactors which also indicate the independence of the 2PA coefficient from the sample thickness. In case of the (100) crystallographic orientation the thin sample deviates from the thick sample by approximately $+6.5\,\%$ for the co- and $-6.3\,\%$ for the cross-polarized configuration. In case of the (110)-oriented sample the deviation is approximately $-11.1\,\%$ for the co- and $-6.7\,\%$ for the cross-polarized configuration. The slightly higher deviation of $-11.1\,\%$ is due to the inaccurate measurement points at $\omega_{\mathrm{sig}}/\omega_{\mathrm{idl}} = 1.1$ and $\omega_{\mathrm{sig}}/\omega_{\mathrm{idl}} = 1.2$.

As already described, the 2PA coefficient for ZnSe, GaAs and Si is dependent on the crystallographic orientation and the polarization configuration of signal and idler pulse. To further elaborate on the anisotropy more in detail, the ratio $\beta_{\perp}/\beta_{\parallel}$ as a function of $\omega_{\mathrm{sig}}/\omega_{\mathrm{idl}}$ is analyzed. The results for all three samples are summarized in Figure 3.9. The error is calculated by

$$\Delta\frac{\beta_{\perp}}{\beta_{\parallel}} = \sqrt{\left(\frac{\Delta\beta_{\perp}}{\beta_{\parallel}}\right)^2 + \left(\frac{\beta_{\perp}\Delta\beta_{\parallel}}{\beta_{\parallel}^2}\right)^2} \tag{3.13}$$

according to the Gaussian error propagation [88]. Most likely the error for $\beta_{\perp}/\beta_{\parallel}$ is overestimated as part of the inaccuracies cancel out, when computing the ratio. This can be

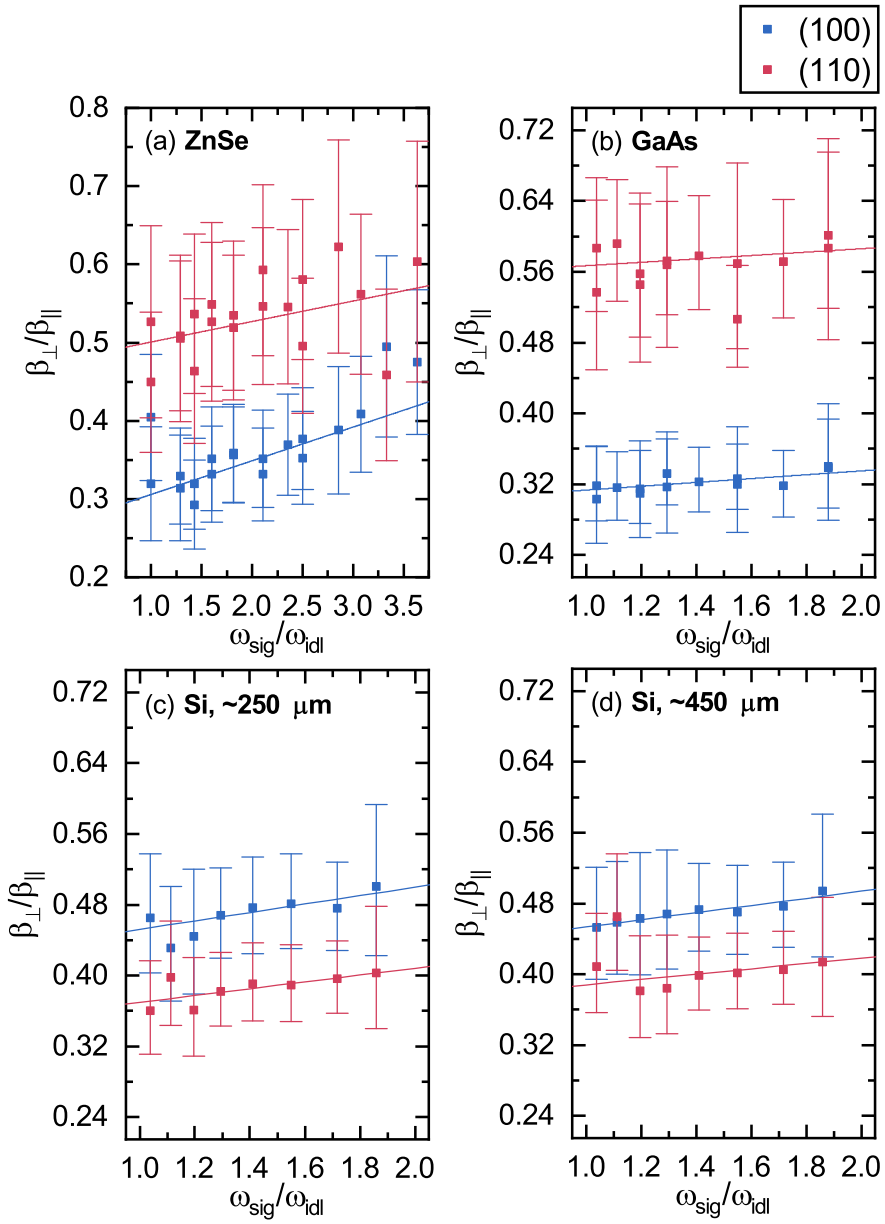

Figure 3.9: Ratio $\beta_\perp/\beta_\parallel$ for (a) ZnSe, (b) GaAs, (c) Si with $d \approx 250\,\mu\text{m}$ and (d) Si with $\approx 450\,\mu\text{m}$ as a function of the frequency ratio $\omega_{\text{sig}}/\omega_{\text{idl}}$. The color indicates the (100) (blue) and (110) (red) crystallographic orientation. The corresponding lines are guides to the eye. Note the different scalings of the y-axis between the ZnSe and GaAs/Si graphs.

seen in the fairly low scatter of $\beta_\perp/\beta_\parallel$, especially for GaAs and Si whose measurements were both acquired with the IR-OPA. The slightly higher scatter of the ZnSe data could depend on using the VIS-OPA.

For ZnSe and GaAs the (100)-oriented crystal shows a more pronounced anisotropy than the (110)-oriented crystal since the values of $\beta_\perp/\beta_\parallel$ for the (100)-oriented sample are overall smaller than for the (110) crystallographic orientation. In case of Si it is reversed. This contrary behavior is at first surprising since ZnSe and GaAs (point group: $\bar{4}3m$) and Si (point group: $m\bar{3}m$) belong to point groups resulting into the same nonzero third-order susceptibility tensor elements which in turn substantially influence the anisotropy (see Chapter 1.2.2.3). However, there must be other decisive factors, for example the character of the bandgap or the space group, which also influence the anisotropy. These factors can only be specified by more precisely comparing the experimental results with theoretical studies which are not yet available.

In contrast to this, $\beta_\perp/\beta_\parallel$ shows a slight increase with increasing $\omega_{\mathrm{sig}}/\omega_{\mathrm{idl}}$ independent of the specific material and crystallographic orientation so that not only the 2PA coefficient is scalable by the degree of non-degeneracy but also the anisotropy. The specific slope is rather comparable for the two crystallographic orientations in one sample with slightly higher values for the (100)-oriented samples. GaAs shows the less pronounced and Si the most pronounced increase. Comparing the (100)-oriented Si samples with different thicknesses reveals similar values of $\beta_\perp/\beta_\parallel$ at same frequency ratios. In case of the (110)-oriented Si sample there are small deviations in the magnitude of $\beta_\perp/\beta_\parallel$ for the two different thicknesses again due to the 2PA values at $\omega_{\mathrm{sig}}/\omega_{\mathrm{idl}} = 1.1$ and $\omega_{\mathrm{sig}}/\omega_{\mathrm{idl}} = 1.2$ in the thinner sample. The value at degeneracy is dependent on the material and its orientation and ranges for all samples between 0.3 and 0.6.

Only for the (100)-oriented GaAs sample the average value $\bar{\beta}_\perp/\bar{\beta}_\parallel \approx 0.31$ ($\Leftrightarrow \bar{\beta}_\parallel - \bar{\beta}_\perp = 12.5\,\mathrm{cm/GW}$) closest to degeneracy at $\omega_{\mathrm{sig}}/\omega_{\mathrm{idl}} = 1.04$ can be compared to other experimental results. Dvorak et al. [26] report a degenerate value of $\beta_\perp/\beta_\parallel \approx 0.41$ at $\lambda_{\mathrm{sig}} = \lambda_{\mathrm{idl}} = 950\,\mathrm{nm}$ for a (001)-oriented crystal whereby in the co-polarized configuration the signal and idler polarization are parallel to the [100]-direction and in the cross-polarized configuration the idler polarization is rotated by 90°. Schroeder et al. [25] also use a (001)-oriented GaAs specimen at $\lambda_{\mathrm{sig}} = \lambda_{\mathrm{idl}} = 950\,\mathrm{nm}$ with the same co- and cross-polarized configuration as Dvorak et al. but a different measurement scheme which reveals $\beta_\parallel - \beta_\perp = (12 \pm 3)\,\mathrm{cm/GW}$. The results agree very well taking into account the differences

between those measurements as for example the excitation energies (References [25, 26] use $2\hbar\omega \approx 2.6\,\mathrm{eV}$ compared to $\hbar\omega_{\mathrm{sig}} + \hbar\omega_{\mathrm{idl}} = 1.57\,\mathrm{eV}$ of the IR-OPA).

The decreasing anisotropy of the 2PA coefficient with higher degrees of non-degeneracy has not been described by other experimental studies before. However, the results can again be compared with the theoretical model of Hannes et al. [89] based on multiband semiconductor Bloch equations as already shown in Figure 3.7. The tailored simulations well capture the increasing trend of $\bar{\beta}_{\perp}/\beta_{\parallel}$ within the experimental uncertainties (see Figure 3.10). The slight increase in the vicinity of degeneracy might be an artifact of the simulations since this cannot be observed in any experimental data (also not in GaAs and Si).

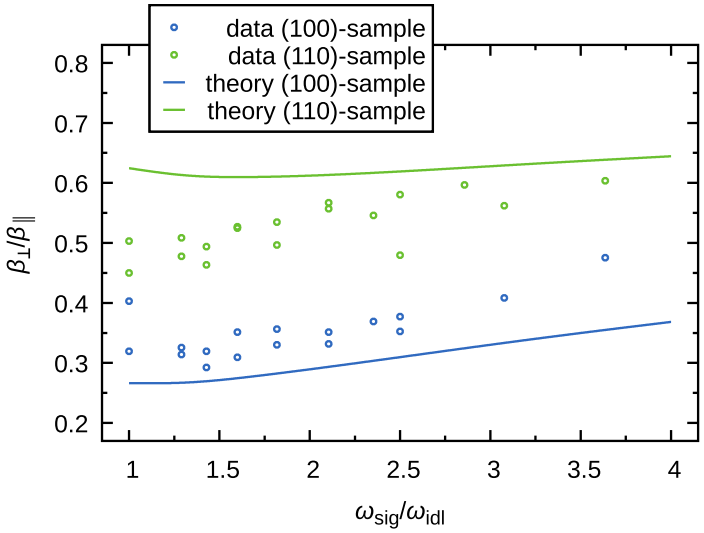

Figure 3.10: Ratio $\beta_{\perp}/\beta_{\parallel}$ for ZnSe as as function of the frequency ratio $\omega_{\mathrm{sig}}/\omega_{\mathrm{idl}}$. The solid lines represent tailored numerical calculations done by W.-R. Hannes (Paderborn University) within the multiband model of Hannes et al. [89]. Experimental and theoretical data is comparable to Figure 3.7. Taken from Reference [89].

Chapter 4

Summary

The non-degenerate 2PA coefficient β as a function of the frequency ratio ω_1/ω_2 was successfully measured for the semiconductors ZnSe, GaAs and Si while keeping the sum energy $\hbar\omega_1 + \hbar\omega_2$ of the two involved photons constant. All three materials show an enhancement of the 2PA strength with increasing frequency ratio $\omega_1/\omega_2 > 1$ regardless of the direct or indirect character of the bandgap. The overall 2PA strength is higher for ZnSe and GaAs than for Si since an interband two-photon transition from the valence to the conduction band can only occur phonon-assisted in an indirect semiconductor. Comparing the 2PA strengths of ZnSe and GaAs at same frequency ratios ω_1/ω_2, the latter reveals overall higher 2PA coefficients due to its smaller bandgap. The experimentally observed scaling of the 2PA coefficient in each material is in good accordance with corresponding theoretical predictions for direct and indirect semiconductors. For ZnSe, not only the scaling but also the absolute magnitudes of the 2PA coefficients agree with tailored numerical calculations.

Future experiments on the scaling of the non-degenerate 2PA coefficient would preferably involve an expansion of the measurement range to even higher degrees of non-degeneracy to better distinguish between different theoretical models since these show significant deviations only very far from degeneracy. In the experimental realization, however, the limits are already reached when using only one OPA for generating both the signal and idler pulse since phase matching conditions for very non-degenerate pulse pairs cannot sufficiently be fulfilled which in turn leads to a destabilization of the OPA. Instead, it would be conceivable to split the signal and idler generation to two OPAs to avoid the phase matching issues as then each OPA only needs to be working at signal or idler wavelength. However, the wavelength tuning is still limited since the nonlinear crystals used in conventional OPAs have strongly reduced transparencies for wavelengths beyond $\approx 2.5\,\mu\text{m}$ [90]. Non-collinear optical parametric amplifiers (NOPAs) could be a promising alternative. These use a

two-stage amplification with non-collinear propagating signal and pump pulses as well as nonlinear crystals with enlarged transparency regions to the mid-IR [91].

In addition to the scaling of the 2PA coefficient, the polarization and orientation anisotropy was investigated. Therefore, co- and cross-polarized configurations are used where the two, both linearly polarized, driving fields are either aligned parallel or perpendicular to each other. Additionally, the ZnSe, GaAs and Si samples are each studied in (100) and (110) crystallographic orientation. For all three materials the magnitude of $\beta_\perp$ is generally smaller than for $\beta_\parallel$ at same frequency ratios. When characterizing the polarization anisotropy in terms of the ratio $\beta_\perp/\beta_\parallel$, the (100)-oriented ZnSe and GaAs samples show a more pronounced anisotropy than the (110)-oriented samples. For Si it is reversed. This contrary behavior leaves open questions for future research since the classification of all three materials to point groups resulting in the same nonzero third-order susceptibility tensor elements would, according to expectations, lead to similar anisotropy. Independent of the specific material and its orientation, $\beta_\perp/\beta_\parallel$ is also slightly increasing with increasing frequency ratio ω_1/ω_2 so that not only the 2PA coefficient is scalable by the degree of non-degeneracy but also its anisotropy. For each material the scaling of the 2PA anisotropy is rather comparable for the two crystallographic orientations. Since the 2PA anisotropy is mainly influenced by the higher conduction bands, the use of an OPA is particularly advantageous as it provides photon pairs of constant sum energy. Thus, always the same conduction bands are involved in the transition which allows the independent investigation of $\beta_\perp/\beta_\parallel(\omega_1/\omega_2)$.

In summary, the non-degenerate 2PA strength can in particular be influenced by the degree of non-degeneracy but also by its polarization and orientation anisotropy. The scaling of the 2PA coefficient is interesting in two respects. As already addressed in the Introduction, an enhancement of the 2PA absorption coefficient can optimize the performance of 2PA based applications as autocorrelators or infrared detectors. On the contrary, the 2PA can also act as a loss mechanism. Especially in applications that are based on other nonlinear phenomena such as the Kerr or Raman effect, the 2PA leads to undesired energy dissipation [64]. Here, a minimization of the 2PA strength is desirable. Considering the 2PA as an essential element of current and future applications and its great potential for properties yet to be explored emphasizes the importance of ongoing fundamental research on two-photon absorption.

Appendix

A.1 MATHEMATICA source code

The following WOLFRAM MATHEMATICA source code is used for the analysis of the two-photon absorption measurement data. The mathematical basic concept is based on the theoretical model of Negres et al. [74]. It is generally applicable to different samples and to co- and cross-polarized configurations. Here, it is exemplarily executed for the (100)-oriented ZnSe sample in co-polarized configuration at a wavelength combination of $\lambda_{\mathrm{sig}} = 570\,\mathrm{nm}$ and $\lambda_{\mathrm{idler}} = 1341\,\mathrm{nm}$ (see also Chapter 3.1.1 for detailed information about this specific measurement). Note that the signal and idler pulses are referred to as probe and pump pulse.

```
ClearAll["Global`*"]

(* import experimental data *)
expdata01100pa570 = Import["C:/.../(100)_570nm_parallel.txt", "Table"];

(* print experimental data, converting format: x-axis from ps to fs, y-axis shift + 1,
     define x-axis shift from zero *)
expdata01100pa570conv = Partition[Riffle[expdata01100pa570[[1 ;; Length[expdata01100pa570], 1]]
     *1000 + 42, expdata01100pa570[[1 ;; Length[expdata01100pa570], 2]] + 1], 2];
expdata01100pa570plot = ListPlot[expdata01100pa570conv, PlotRange -> All]
```

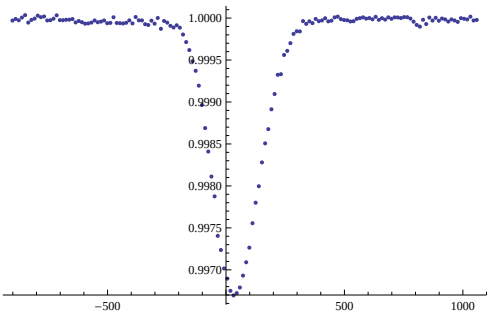

```
(* select data set *)
expdataconv = expdata01100pa570conv;
expdataplot = expdata01100pa570plot;

(* constants *)
c0 = 3*10^-5; (*  velocity of light [cm/fs] *)

(* experimental parameters *)
L = 42*10^(-4); (* sample length [cm] *)
lpr = 570; (* probe wavelength [nm] *)
lpu = 1341; (* pump wavelength [nm] *)
tpu = 98.2; (* pump pulse length [fs] (FWHM) *)
wpr = 2. Pi c0/(lpr 10^-7); (* probe frequency [1/fs] with wavelength in cm *)
wpu = 2. Pi c0/(lpu 10^-7);(* pump frequency [1/fs] with wavelength in cm *)
R = 0.15948; (* pump reflectivity @ 1341nm, p-polarized, angle of incidence: 20degree *)
freplaser = 250000; (* laser repetition frequency [Hz] *)
Ppu = 0.45; (* pump power [mW] *)
Apu = 0.000301271; (* idler cross section [cm^2] (FW1/eM) *)
Apuerror = 4.83517*10^(-6); (* idler cross section error [cm^2] (FW1/eM) *)

(* calculation of pump peak intensity *)
scale1 = 1./Sqrt[Log[2]]; (* tpu: FWHM -> FW1/eM *)
scale2 = E/(E - 1.); (* average intensity -> peak intensity *)
Ipuaverage = (1 - R)*(Ppu*10^(-12))/(freplaser*tpu*scale1*10^(-15)*Apu); (* pump average
     intensity [GW/cm^2] *)
Ipu = Ipuaverage*scale2; (* pump peak intensity [GW/cm^2] *)

(* calculation of refractive and group refractive index *)
(* Sellmeier equation with wavelength in cm *)
ngeneric[l_, B1_, C1_, B2_, C2_, B3_, C3_] := Sqrt[1 + (B1*(l*10^4)^2/((l*10^4)^2 - C1)) +
     (B2*(l*10^4)^2/((l*10^4)^2 - C2)) + (B3*(l*10^4)^2/((l*10^4)^2 - C3))]
(* Sellmeier coefficients for ZnSe calculated with wavelength in [10^(-6)m] *)
B11 = 4.713; C11 = 0.03741;
B21 = 0.13085; C21 = 0.20464;
B31 = 0.96186; C31 = 1059.53848;
n[l_] := ngeneric[l, B11, C11, B21, C21, B31, C31] (* refractive index *)
k[w_] := n[2. Pi c0/w] (w)/c0; (* wave vector [1/cm] *)
inversevgr[w_] = D[k[w], w]; (* group velocity [cm/fs] *)
GVD[w_] = D[k[w], {w, 2}]; (* group velocity dispersion [fs^2/mm] *)
ngr[w_] = c0*inversevgr[w]; (* group refractive index *)

npr = n[lpr*10^(-7)]; (* probe refractive index *)
ngrpr = ngr[wpr]; (* probe group refractive index *)
npu = n[lpu*10^(-7)]; (* pump refractive index *)
ngrpu = ngr[wpu]; (* pump group refractive index *)
deltangr = ngrpr - ngrpu; (* group velocity mismatch *)

(* conversion of pulse lenghts *)
convpar = 1/(2 Sqrt[Log[2]])*1.; (* pulse length: FWHM -> HW1/eM *)
tpuconv = convpar*tpu; (* pump pulse length [fs] (HW1/eM), notation in Negres et al.: omegap *)
```

```
(* parameters for fit *)
sigmafit = 0; (* linear absorption parameter set as zero: sigma=1/2*alpha*L *)
gammafit = L*npr/npu*Ipu*beta; (* nonlinear absorption parameter with beta [GW/cm] *)
rhofit = L/(tpuconv*c0)*deltangr; (* walk-off parameter *)

(* nonlinear transmittance (see Equation (14) in Negres et al.) *)
Q[sigma_, tau_, W_, rho_, gamma_] := Exp[-2*sigma]/(W*Sqrt[Pi])*NIntegrate[Exp[(-1)*((t
     + tau/tpuconv - rho)/(W))^2 - (gamma*Sqrt[Pi])/(rho)*(Erf[t] - Erf[t - rho])], {t, -Infinity,
     Infinity}]; (* tau is the variable real delay time *)

(* test calculation fot fit to estimate start values for beta and trprconv *)
beta = 12.5;
tprconvtest = 120;
Wtest = tprconvtest/tpuconv;
testtable = Table[{taurange, Q[sigmafit, taurange, Wtest, rhofit, gammafit]}, {taurange,
     -600, 600, 25}];
plottesttable = ListLinePlot[testtable, PlotRange -> {All, {0.98, 1.00009}}, PlotStyle ->
     Directive[Green, Thick]];
Show[{plottesttable,  expdataplot}, PlotRange -> {{-600, 600}, {1.001, 0.996}}]
```

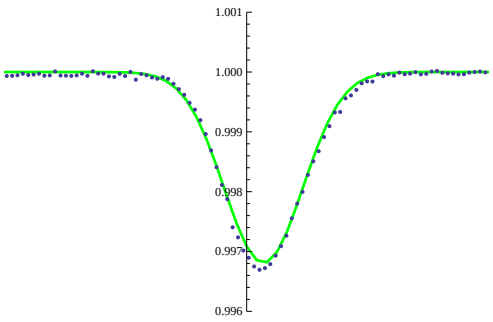


```
(* fit of dataset *)
fitfunctionQnon[tprconvfitnon_?NumericQ, betafitnon_?NumericQ, taufitnon_?NumericQ] :=
     Exp[-2*sigmafit]/(tprconvfitnon/tpuconv*Sqrt[Pi])*NIntegrate[Exp[(-1)*((tnon +
     taufitnon/tpuconv - rhofit)/(tprconvfitnon/tpuconv))^2 - (L*npr/npu* Ipu*betafitnon*
     Sqrt[Pi])/(rhofit)*(Erf[tnon] - Erf[tnon - rhofit])], {tnon, -Infinity, Infinity}];
fitQnon = NonlinearModelFit[expdataconv, fitfunctionQnon[tprconvfitnon, betafitnon, taufitnon],
     {{tprconvfitnon, 120.0}, { betafitnon, 10.0}}, taufitnon] (* insert start values *)
Qnonfit = Plot[fitQnon[taufitnon], {taufitnon, -500, 500}, PlotRange -> { {-500, 500}, All} ,
     PlotStyle ->  Directive[Green, Thick]];
tableQnonfit = Table[{taufitnon, fitQnon[taufitnon]}, {taufitnon, -500, 500, 10}];
Export[NotebookDirectory[] <> "TPA-fits_(100)_pa_570nm_fit.dat", tableQnonfit];
Export[NotebookDirectory[] <> "TPA-fits_(100)_pa_570nm_data.dat", fitQnon["ParameterTable"]];
Export[NotebookDirectory[] <> "TPA-fits_(100)_pa_570nm_plot.pdf", Qnonfit];
Show[Qnonfit, expdataplot]
fitQnon["ParameterTable"]
```

FittedModel[fitfunctionQnon[120.743, 12.9326, taufitnon]]

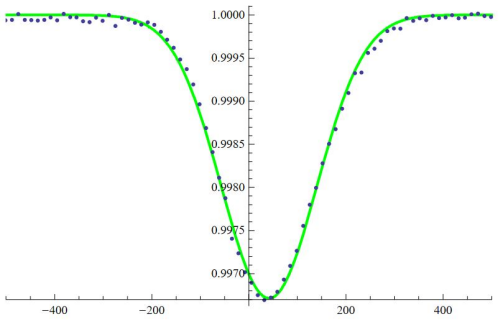

	Estimate	Standard Error	t-Statistic	P-Value
tprconvfitnon	120.743	0.94858	127.288	1.71939×10^{-151}
betafitnon	12.9326	0.0668175	193.552	6.63669×10^{-178}

```
(* calculate error of beta *)
(* errors dependent on wavelength: tprconv [fs], Apu [cm^2]  *)
mytprconvfitnon = tprconvfitnon /. fitQnon["BestFitParameters"];
mytprconfitnonerror = fitQnon["ParameterErrors"][[1]];
tprconverrorplus = mytprconvfitnon + mytprconfitnonerror;
tprconverrorminus = mytprconvfitnon - mytprconfitnonerror;
Apuerrorplus = (Apu + Apuerror);
Apuerrorminus = (Apu - Apuerror);

(* fixed errors independendent on wavelength: tpuconv [fs] (tpu [fs]), L [cm], Ppu [GW] *)
tpuerrorplus = tpu + 5;
tpuerrorminus = tpu - 5;
tpuconverrorplus = tpuerrorplus*convpar;
tpuconverrorminus = tpuerrorminus*convpar;
Lerrorplus = L + 1*10^(-4);
Lerrorminus = L - 1*10^(-4);
Ppuerrorplus = (Ppu + 0.03) *10^(-12);
Ppuerrorminus = (Ppu - 0.03) *10^(-12);

(* calculation of betaplus *)
Ipuerrorplus = (1 - R)*Ppuerrorminus/(tpuerrorplus*scale1*250000*10^(-15)*Apuerrorplus)*(scale2);
mybetafitnon = betafitnon /. fitQnon["BestFitParameters"];
fitfunctionQerrorplus[betaerrorplus_?NumericQ, tauerrorplus_?NumericQ] :=
     1/(tprconverrorplus/tpuconverrorplus*Sqrt[Pi])*NIntegrate[Exp[(-1)*((terrorplus
     + tauerrorplus/tpuconverrorplus - Lerrorminus/(tpuconverrorplus*c0)*deltangr )/
     (tprconverrorplus/tpuconverrorplus))^2 - (Lerrorminus*npr/npu* Ipuerrorplus* betaerrorplus
     *Sqrt[Pi])/(Lerrorminus/(tpuconverrorplus*c0)*deltangr )*(Erf[terrorplus] - Erf[terrorplus -
     Lerrorminus/(tpuconverrorplus*c0)*deltangr ])], {terrorplus, -Infinity, Infinity}];
fitQerrorplus = NonlinearModelFit[expdataconv, fitfunctionQerrorplus[betaerrorplus, tauerrorplus],
     {{ betaerrorplus, mybetafitnon}}, tauerrorplus];
Deltabetaplus = Abs[mybetafitnon - betaerrorplus /. fitQerrorplus["BestFitParameters"]];

(* calculation of betaminus *)
Ipuerrorminus = (1 - R)*Ppuerrorplus/(tpuerrorminus*scale1*250000*10^(-15)*Apuerrorminus)*(scale2);
mybetafitnon = betafitnon /. fitQnon["BestFitParameters"];
```

```
fitfunctionQerrorminus[betaerrorminus_?NumericQ, tauerrorminus_?NumericQ] :=
     1/(tprconverrorminus/tpuconverrorminus*Sqrt[Pi])*NIntegrate[Exp[(-1)*((terrorminus
     + tauerrorminus/tpuconverrorminus - Lerrorplus/(tpuconverrorminus*c0)*deltangr )/
     (tprconverrorminus/tpuconverrorminus))^2 - (Lerrorplus*npr/npu* Ipuerrorminus*betaerrorminus
     *Sqrt[Pi])/(Lerrorplus/(tpuconverrorminus*c0)*deltangr )*(Erf[terrorminus] - Erf[terrorminus -
     Lerrorplus/(tpuconverrorminus*c0)*deltangr ])], {terrorminus, -Infinity, Infinity}];
fitQerrorminus = NonlinearModelFit[expdataconv, fitfunctionQerrorminus[betaerrorminus, tauerrorminus],
     {{ betaerrorminus, mybetafitnon - 20}}, tauerrorminus];
Deltabetaminus = mybetafitnon - betaerrorminus /. fitQerrorminus["BestFitParameters"];

(* summary of results *)
Print["fitting results:"]
Grid[{
  {"`beta [cm/GW]", mybetafitnon},
  {"+ deltabeta [cm/GW]", Deltabetaplus},
  {"- deltabeta [cm/GW]", Deltabetaminus},
  {"taupr [fs] (HW1/eM)", mytprconvfitnon},
  {"deltataupr [fs]", mytprconfitnonerror }
  }, Alignment -> {{Left, Left}}]
```

fitting results:

beta [cm/GW]	12.9326
+ deltabeta [cm/GW]	1.58708
- deltabeta [cm/GW]	1.35929
taupr [fs] (HW1/eM)	120.743
deltataupr [fs]	0.94858

Bibliography

[1] Y. R. Shen, *The Principles of Nonlinear Optics*. New York: John Wiley & Sons, Inc., 1st ed., (1984).

[2] M. Göppert-Mayer, "Über Elementarakte mit zwei Quantensprüngen." *Annalen der Physik* **401**, 273–294 (1931).

[3] T. H. Maiman, "Stimulated optical radiation in ruby." *Nature* **187**, 493–494 (1960).

[4] T. H. Maiman, "Optical maser action in ruby." *British Communication & Electronics* **7**, 674–676 (1960).

[5] W. Kaiser and C. G. B. Garrett, "Two-photon excitation in CaF_2:Eu^{2+}." *Physical Review Letters* **7**, 229–231 (1961).

[6] R. Braunstein and N. Ockman, "Optical double-photon absorption in CdS." *Physical Review* **134**, A499–A507 (1964).

[7] Y. Takagi, T. Kobayashi, K. Yoshihara and S. Imamura, "Multiple- and single-shot autocorrelator based on two-photon conductivity in semiconductors." *Optics Letters* **17**, 658–660 (1992).

[8] D. T. Reid, W. Sibbett, J. M. Dudley, L. P. Barry, B. Thomsen and J. D. Harvey, "Commercial semiconductor devices for two photon absorption autocorrelation of ultrashort light pulses." *Applied Optics* **37**, 8142–8144 (1998).

[9] A. Hayat, A. Nevet, P. Ginzburg and M. Orenstein, "Applications of two-photon processes in semiconductor photonic devices: invited review." *Semiconductor Science and Technology* **26**, 083001 (2011).

[10] H. Schneider, T. Maier, H. C. Liu, M. Walther and P. Koidl, "Ultrasensitive femtosecond two-photon detector with resonantly enhanced nonlinear absorption." *Optics Letters* **30**, 287–289 (2005).

[11] D. D. Yavuz, "All-optical femtosecond switch using two-photon absorption." *Physical Review A* **74**, 053804 (2006).

[12] R. Atanasov, A. Haché, J. L. P. Hughes, H. M. Van Driel and J. E. Sipe, "Coherent control of photocurrent generation in bulk semiconductors." *Physical Review Letters* **76**, 1703 (1996).

[13] A. Haché, Y. Kostoulas, R. Atanasov, J. L. P. Hughes, J. E. Sipe and H. M. Van Driel, "Observation of coherently controlled photocurrent in unbiased, bulk GaAs." *Physical Review Letters* **78**, 306 (1997).

[14] M. Sheik-Bahae, A. A. Said, T.-H. Wei, D. J. Hagan and E. W. Van Stryland, "Sensitive measurement of optical nonlinearities using a single beam." *IEEE Journal of Quantum Electronics* **26**, 760–769 (1990).

[15] J. A. Bolger, A. K. Kar, B. S. Wherrett, R. DeSalvo, D. C. Hutchings and D. J. Hagan, "Nondegenerate two-photon absorption spectra of ZnSe, ZnS and ZnO." *Optics Communications* **97**, 203–209 (1993).

[16] M. Sheik-Bahae, J. Wang, R. DeSalvo, D. J. Hagan and E. W. Van Stryland, "Measurement of nondegenerate nonlinearities using a two-color Z scan." *Optics Letters* **17**, 258 (1992).

[17] S. Chen, M.-L. Zheng, X.-Z. Dong, Z.-S. Zhao and X.-M. Duan, "Nondegenerate two-photon absorption in a zinc blende-type ZnS single crystal using the femtosecond pump-probe technique." *Journal of the Optical Society of America B* **30**, 3117–3122 (2013).

[18] C. M. Cirloganu, L. A. Padilha, D. A. Fishman, S. Webster, D. J. Hagan and E. W. Van Stryland, "Extremely nondegenerate two-photon absorption in direct-gap semiconductors [Invited]." *Optics Express* **19**, 22951–22960 (2011).

[19] D. A. Fishman, C. M. Cirloganu, S. Webster, L. A. Padilha, M. Monroe, D. J. Hagan and E. W. Van Stryland, "Sensitive mid-infrared detection in wide-bandgap semiconductors using extreme non-degenerate two-photon absorption." *Nature Photonics* **5**, 561–565 (2011).

[20] R. Sarkissiana and J. O'Brien, "Cross two photon absorption in a silicon photonic crystal waveguide fiber taper coupler with a physical junction." *Journal of Applied Physics* **117**, 033101 (2015).

[21] Y. Zhang, C. Husko, S. Lefrancois, I. H. Rey, T. F. Krauss, J. Schröder and B. J. Eggleton, "Non-degenerate two-photon absorption in silicon waveguides: analytical and experimental study." *Optics Express* **23**, 17101-17110 (2015).

[22] N. Poulvellarie, C. Ciret, B. Kuyken, F. Leo and S.-P. Gorza, "Highly nondegenerate two-photon absorption in silicon wire waveguides." *Physical Review Applied* **10**, 024033 (2018).

[23] S. Faryadras, N. Cox, D. J. Hagan and E. W. Van Stryland, "Non-degenerate two-photon absorption spectroscopy of bulk silicon." *Proceedings 2021 IEEE Research and Applications of Photonics in Defense Conference (RAPID)* **39**, 1–2 (2021).

[24] N. Cox, D. J. Hagan and E. W. Van Stryland, "Extremely nondegenerate two-photon absorption in silicon (Conference Presentation)." *Proceedings Volume* **10916**, *Ultrafast Phenomena and Nanophotonics* **XXIII**, 1091613 (2019).

[25] W. A. Schroeder, D. S. McCallum, D. R. Harken, M. D. Dvorak, D. R. Andersen, A. L. Smirl and B. S. Wherrett, "Intrinsic and induced anisotropy of nonlinear absorption and refraction in zinc blende semiconductors." *Journal of the Optical Society of America B* **12**, 401–415 (1995).

[26] M. D. Dvorak, W. A. Schroeder, D. R. Andersen, A. L. Smirl and B.S. Wherrett, "Measurement of the anisotropy of two-photon absorption coefficients in zincblende semiconductors." *IEEE Journal of Quantum Electronics* **30**, 256–268 (1994).

[27] R. DeSalvo, M. Sheik-Bahae, A. A. Said, D. J. Hagan and E. W. Van Stryland, "Z-scan measurements of the anisotropy of nonlinear refraction and absorption in crystals." *Optics Letters* **18**, 194–196 (1993).

[28] J. P. van der Ziel, "Two-photon absorption spectra of GaAs with $2\hbar\omega_1$ near the direct band gap." *Physical Review B* **16**, 2775 (1977).

[29] S. J. Bepko, "Anisotropy of two-photon absorption in GaAs and CdTe." *Physical Review B* **12**, 669 (1975).

[30] M. Dinu, F. Quochi and H. Garcia, "Third-order nonlinearities in silicon at telecom wavelengths." *Applied Physics Letters* **82**, 2954 (2003).

[31] R. Salem and T. E. Murphy, "Polarization-insensitive cross correlation using two-photon absorption in a silicon photodiode." *Optics Letters* **29**, 1524–1526 (2004).

[32] T. Kagawa and S. Ooami, "Polarization dependence of two-photon absorption in Si avalanche photodiodes." *Japanese Journal of Applied Physics* **46**, 664 (2007).

[33] J. Zhang, Q. Lin, G. Piredda, R. W. Boyd, G. P. Agrawal and P. M. Fauchet, "Anisotropic nonlinear response of silicon in the near-infrared region." *Applied Physics Letters* **91**, 071113 (2007).

[34] G. S. He and S. H. Liu, *Advanced Nonlinear Optics.* Singapore: World Scientific Publishing Co. Pte. Ltd., 1st ed., (2018).

[35] E. E. Mamajek, A. Prsa, G. Torres, P. Harmanec, M. Asplund, P. D. Bennett, N. Capitaine, J. Christensen-Dalsgaard, E. Depagne, W. M. Folkner, M. Haberreiter, S. Hekker, J. L. Hilton, V. Kostov, D. W. Kurtz, J. Laskar, B. D. Mason, E. F. Milone, M. M. Montgomery, M. T. Richards, J. Schou and S. G. Stewart, "IAU 2015 Resolution B3 on Recommended nominal conversion constants for selected solar and planetary properties." arXiv:1510.07674v1 (2015).

[36] R. W. Boyd, *Nonlinear Optics.* London: Academic Press, Elsevier Inc., 4th ed., (2020).

[37] E. G. Sauter, *Nonlinear Optics.* New York: John Wiley & Sons, Inc., 1st ed., (1996).

[38] M. Fox, *Optische Eigenschaften von Festkörpern.* München: Oldenbourg Wissenschaftsverlag GmbH, 1st ed., (2012).

[39] P. N. Butcher and D. Cotter, *The elements of nonlinear optics.* Cambridge: Cambridge University Press, 1st ed., (1990).

[40] V. Degiorgio and I. Cristiani, *Photonics - A short Course.* Cham: Springer International Publishing AG, 2nd ed., (2016).

[41] E. W. Van Stryland, A. L. Smirl, T. F. Boggess, M. J. Soileau, B. S. Wherrett and F. A. Hopf, "Weak-wave retardation and phase-conjugate self-defousing in Si." *Picosecond Phenomena III. Springer Series in Chemical Physics* **23**, 368–371 (1982).

[42] D. C. Hutchings and E. W. Van Stryland, "Nondegenerate two-photon absorption in zinc blende semiconductors." *Journal of the Optical Society of America B* **9**, 2065–2074 (1992).

[43] L. V. Keldysh, "Ionization in the field of a strong electromagnetic wave." *Soviet Physics JETP* **20**, 1785 (1965).

[44] M. H. Weiler, "Nonparabolicity and exciton effects in two-photon absorption in zincblende semiconductors." *Solid State Communications* **39**, 937–940 (1981).

[45] B. S. Wherrett, "Scaling rules for multiphoton interband absorption in semiconductors." *Journal of the Optical Society of America B* **1**, 67–72 (1984).

[46] C. Aversa, J. E. Sipe, M. Sheik-Bahae and E. W. Van Stryland, "Third-order optical nonlinearities in semiconductors: The two-band model." *Physical Review B* **50**, 18073 (1994).

[47] W.-R. Hannes and T. Meier, "Higher-order contributions and nonperturbative effects in the nondegenerate nonlinear optical absorption of semiconductors using a two-band model." *Physical Review B* **99**, 125301 (2019).

[48] E. O. Kane, "Band structure of indium antimonide." *Journal of Physics and Chemistry of Solids* **1**, 249–261 (1957).

[49] M. Sheik-Bahae, D. C. Hutchings, D. J. Hagan and E. W. Van Stryland, "Dispersion of bound electron nonlinear refraction in solids." *IEEE Journal of Quantum Electronics* **27**, 1296–1309 (1991).

[50] M. Sheik-Bahae, J. Wang and E. W. Van Stryland, "Nondegenerate optical kerr effect in semiconductors." *IEEE Journal of Quantum Electronics* **30**, 249–255 (1994).

[51] M. Grundmann, *The Physics of Semiconductors*. Cham: Springer International Publishing AG, 3rd ed., (2016).

[52] C. C. Lee and H. Y. Fan, "Two-photon absorption with exciton effect for degenerate valence bands." *Physical Review B* **9**, 3502 (1974).

[53] C. R. Pidgeon, B. S. Wherrett, A. M. Johnston, J. Dempsey and A. Miller, "Two-photon absorption in zinc-blende semiconductors." *Physical Review Letters* **42**, 1785 (1979).

[54] I. M. Catalano and A. Cingolani, "Non-parabolic band effect on two-photon absorption in ZnSe and CdTe." *Solid State Communications* **43**, 213–215 (1982).

[55] H. Garcia and R. Kalyanaraman, "Phonon-assisted two-photon absorption in the presence of a dc-field: the nonlinear Franz-Keldysh effect in indirect gap semiconductors." *Journal of Physics B: Atomic, Molecular and Optical Physics* **39**, 2737 (2006).

[56] I. M. Catalano, A. Cingolani, R. Cingolani and M. Lepore, "Interband two-photon absorption mechanisms in direct and indirect gap materials." *Physica Scripta* **37**, 579–582 (1988).

[57] M. Dabbicco and M. Brambilla, "Dispersion of the two-photon absorption coefficient in ZnSe." *Solid State Communications* **114**, 515–519 (2000).

[58] W. C. Hurlbut, Y.-S. Lee, K. L. Vodopyanov, P. S. Kuo and M. M. Fejer, "Multiphoton absorption and nonlinear refraction of GaAs in the mid-infrared." *Optics Letters* **32**, 668–670 (2007).

[59] M. Balu, L. A. Padilha, D. J. Hagan, E. W. Van Stryland, S. Yao, K. Belfield, S. Zheng, S. Barlow and S. Marder, "Broadband Z-scan characterization using a high-spectral-irradiance, high-quality supercontinuum." *Journal of the Optical Society of America B* **25**, 159–165 (2008).

[60] E. W. Van Stryland, M. A. Woodall, H. Vanherzeele and M. J. Soileau, "Energy band-gap dependence of two-photon absorption." *Optics Letters* **10**, 490–492 (1985).

[61] P. D. Olszak, C. M. Cirloganu, S. Webster, L. A. Padilha, S. Guha, L. P. Gonzalez, S. Krishnamurthy, D. J. Hagan and E. W. Van Stryland, "Spectral and temperature dependence of two-photon and free-carrier absorption in InSb." *Physical Review B* **82**, 235207 (2010).

[62] J. Singh, *Electronic and Optoelectronic Properties of Semiconductor Structures.* Cambridge: Cambridge University Press, 1st ed., (2003).

[63] M. Dinu, "Dispersion of phonon-assisted nonresonant third-order nonlinearities." *IEEE Journal of Quantum Electronics* **39**, 1498–1503 (2003).

[64] B. Jalali, S. Fathpour and K. Tsia, "Green silicon photonics." *Optics and Photonics News* **20**, 18–23 (2009).

[65] X. Sang, E.-K. Tien and O. Boyraz, "Applications of two-photon absorption in silicon." *Journal of Optoelectronics and Advanced Materials* **11**, 15–25 (2008).

[66] A. D. Bristow, N. Rotenberg and H. M. van Driel, "Two-photon absorption and kerr coefficients of silicon for $850 - 2200\,\mathrm{nm}$." *Applied Physics Letters* **90**, 191104 (2007).

[67] Q. Lin, J. Zhang, G. Piredda, R. W. Boyd, P. M. Fauchet and G. P. Agrawal, "Dispersion of silicon nonlinearities in the near infrared region." *Applied Physics Letters* **91**, 021111 (2007).

[68] D. Seo, J. M. Gregory, L. C. Feldman, N. H. Tolk and P. I. Cohen, "Multiphoton absorption in germanium using pulsed infrared free-electron laser radiation." *Physical Review B* **83**, 195203 (2011).

[69] H. Garcia and K. N. Avanaki, "Direct and indirect two-photon absorption in Ge within the effective mass approximation." *Applied Physics Letters* **100**, 131105 (2012).

[70] D. C. Hutchings and B. S. Wherrett, "Theory of polarization dependence of two-photon absorption in zinc-blende semiconductors." *Journal of Modern Optics* **41**, 1141–1149 (1994).

[71] D. C. Hutchings and B. S. Wherrett, "Theory of anisotropy of two-photon absorption in zinc-blende semiconductors." *Physical Review B* **49**, 2418 (1994).

[72] D. C. Hutchings and B. S. Wherrett, "Linear/circular dichroism of two-photon absorption in zinc-blende semiconductors." *Optical Materials* **3**, 53–60 (1994).

[73] R. Gross and A. Marx, *Festkörperphysik*. Berlin/Boston: Walter de Gruyter GmbH, 3rd ed., (2018).

[74] R. A. Negres, J. M. Hales, A. Kobyakov, D. J. Hagan and E. W. Van Stryland, "Experiment and analysis of two-photon absorption spectroscopy using a white-light continuum probe." *IEEE Journal of Quantum Electronics* **38**, 1205–1216 (2002).

[75] T. Skauli, P. S. Kuo, K. L. Vodopyanov, T. J. Pinguet, O. Levi, L. A. Eyres, J. S. Harris and M. M. Fejer, "Improved dispersion relations for GaAs and applications to nonlinear optics." *Journal of Applied Physics* **94**, 6447–6455 (2003).

[76] G. P. Agrawal, *Nonlinear Fiber Optics*. Amsterdam: Elsevier Inc., 5th ed., (2013).

[77] J. H. Bechtel and W. L. Smith, "Two-photon absorption in semiconductors with picosecond laser pulses." *Physical Review B* **13**, 3515 (1976).

[78] J. A. Arnaud, W. M. Hubbard, G. D. Mandeville, B. de la Clavière, E. A. Franke and J. M. Franke, "Technique for fast measurement of gaussian laser beam parameters." *Applied Optics* **10**, 2775–2776 (1971).

[79] E. Hecht, *Optik*. Berlin/Boston: Walter de Gruyter GmbH, 7th ed., (2018).

[80] I. N. Bronstein, K.A. Semendjajew, G. Musiol and H. Mühlig, *Taschenbuch der Mathematik*. Haan-Gruiten: Verlag Europa-Lehrmittel Nourney, Vollmer GmbH & Co. KG, 10th ed., (2016).

[81] S. Toenger, R. Mäkitalo, J. Ahvenjärvi, P. Ryczkowski, M. Närhi, J. M. Dudley and G. Genty, "Interferometric autocorrelation measurements of supercontinuum based on two-photon absorption." *Journal of the Optical Society of America B* **36**, 1320–1326 (2019).

[82] J.-C. Diels and W. Rudolph, *Ultrashort Laser Pulse Phenomena: Fundamentals, Techniques, and Applications on a Femtosecond Time Scale.* Amsterdam: Elsevier Inc., 2nd ed., (2006).

[83] R. Menzel, *Photonics.* Berlin/Heidelberg: Springer Science+Business Media S.A., 3rd ed., (2007).

[84] `http://refractiveindex.info/`.

[85] M. Querry, *Optical constants of minerals and other materials from the millimeter to the ultraviolet.* Chemical Research Development and Engineering Center Aberdeen Proving Ground, 1987.

[86] H. H. Li, "Refractive index of silicon and germanium and its wavelength and temperature derivatives." *Journal of Applied Physics* **9**, 561 (1980).

[87] W. Sellmeier, "Ueber die durch die Aetherschwingungen erregten Mitschwingungen der Körpertheilchen und deren Rückwirkung auf die ersteren, besonders zur Erklärung der Dispersion und ihrer Anomalien." *Annalen der Physik und Chemie* **223**, 386–403 (1872).

[88] H. J. Eichler, H.-D. Kronfeldt and J. Sahm, *Das neue physikalische Grundpraktikum.* Berlin/Heidelberg: Springer Spektrum, 3rd ed., (2016).

[89] L. Krauss-Kodytek, W.-R. Hannes, T. Meier, C. Ruppert and M. Betz, "Non-degenerate two-photon absorption in ZnSe: Experiment and theory." *Physical Review B* **104**, 085201 (2021).

[90] R. Akbari and A. Major, "Optical, spectral and phase-matching properties of BIBO, BBO and LBO crystals for optical parametric oscillation in the visible and near-infrared wavelength ranges." *Laser Physics* **23**, 035401 (2013).

[91] D. Brida, C. Manzoni, G. Cirmi, M. Marangoni, S. De Silvestri and G. Cerullo, "Generation of broadband mid-infrared pulses from an optical parametric amplifier." *Optics Express* **15**, 15035–15040 (2007).

Publications and Contributions

Publications:

L. Krauss-Kodytek, C. Ruppert and M. Betz
"Near-infrared non-degenerate two-photon absorption coefficients of bulk GaAs and Si"
Optics Express **29**, 34522–34530 (2021)

L. Krauss-Kodytek, W.-R. Hannes, T. Meier, C. Ruppert and M. Betz
"Non-Degenerate two-photon absorption in ZnSe: Experiment and theory"
Physical Review B **104**, 085201 (2021) - Editors' Suggestion

W.-R. Hannes, L. Krauss-Kodytek, C. Ruppert, M. Betz and T. Meier
"Intensity-dependent degenerate and non-degenerate nonlinear optical absorption of direct-gap semiconductors"
Proceedings SPIE 10916, Ultrafast Phenomena and Nanophotonics XXIII, 109160O (2019)

Supervised thesis:

J. Schroeer
"Nichtentartete Zweiphotonenabsorption in GaAs"
Bachelor Thesis, TU Dortmund University, Experimentelle Physik 2 (2019)

Acknowledgements

Throughout my dissertation I have received a great deal of support which made it possible to overcome the minor and major challenges during the last years. Therefore, I am particularly grateful to...

... Prof. Dr. Markus Betz for the continuous support, the appreciative collaboration and the diverse discussions in which he openly shared his scientific expertise.

... Prof. Dr. Carsten Westphal for kindly agreeing to review my thesis.

... Dr. Claudia Ruppert for patiently answering all my questions, helping me solving any lab issue and introducing me to MATHEMATICA.

... Prof. Dr. Torsten Meier and Dr. Wolf-Rüdiger Hannes for the fruitful collaboration in the framework of project A07 of the SFB TRR 142 funded by the Deutsche Forschungsgemeinschaft (project number 231447078).

... all my colleagues at E2. Having people around who face the same issues makes everything much easier. I especially like to thank Sergiu Anghel, Felix Paßmann, Stephan Melzer, Jan Lohrenz, Thorben Jostmeier, Daniel Keck, Michal Kobecki, Clara Rittmann and my personal fellow in misery and happiness Jan Mundry.

... all other indispensable members of or connected to E2: Michaela Wäscher, Katharina Sparka, Nina Sesemann-Collette, Dirk Schemionek, Klaus Wiegers, Daniel Tüttmann and Lars Wieschollek.

... my dear friends and my lovely family for always being there when I needed some kind words to keep me motivated. They always managed to convince me all these years that graduation day would come. Insbesondere danke ich von Herzen meinen liebsten Eltern Barbara und Rainer und meiner allerbesten Schwester Linda.

... my husband Leonard, without whom I would not be holding this work in my hands today. You mean everything to me.